STUDIA UNIVERSITATIS
BABEŞ-BOLYAI

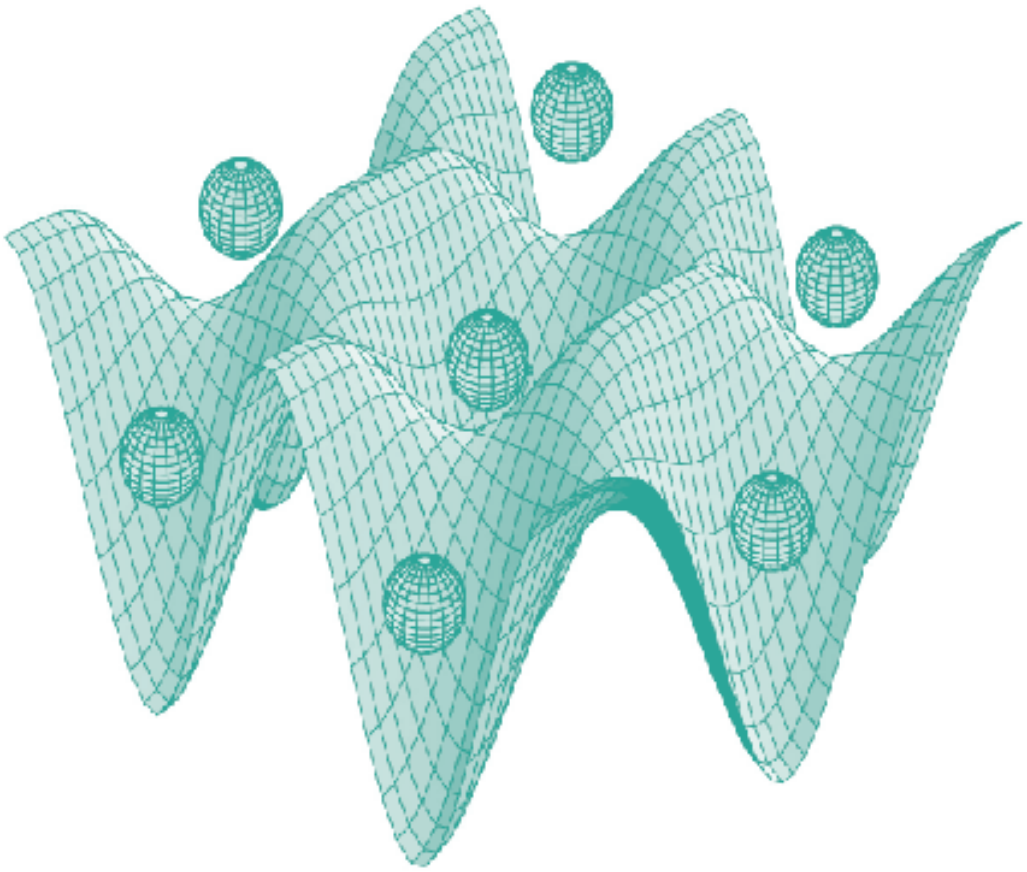

PHYSICA

1/2009

ANUL LIV **2009**

S T U D I A

UNIVERSITATIS BABEŞ–BOLYAI

PHYSICA

1

Desktop Editing Office: 51st B.P.Hasdeu Street, Cluj-Napoca, Romania, phone + 40 264 405352

SUMAR - SOMMAIRE - CONTENTS - INHALT

STUDIA UNIVERSITATIS BABES-BOLYAI, PHYSICA, LIV, 1, 2009

UV-VIS AND FLUORESCENCE STUDY ON PROTEIN ENRICHED SIMULATED BODY FLUID

E. LÁSZLOFFI[1], K. MAGYARI[1], V. SIMON[1,*]

ABSTRACT. UV-vis and fluorescence analyses were carried out to investigate the spectroscopic changes induced by increasing concentration of bovine serum albumin in a solution of simulated body fluid, prepared according to Kokubo protocol. In this study are presented the results obtained from as prepared solutions. The linear increase of absorbance in UV-vis spectral region can be used to evaluate the protein concentration in solution. The fluorescence intensity dependence on BSA concentration has an inflection point at 1.41 mg/ml BSA in SBF, denoting a diminished fluorescence quantum yield for higher BSA concentration.

Keywords: Bovine serum albumin; simulated body fluid; fluorescence; UV-vis spectroscopy.

Introduction

Proteins are the building blocks from which cells are assembled. They are large molecules, with molecular weights in the tens of thousands Da, found in all the cells and tissues of the body. They are formed by the successive addition of hundreds of amino acids, folded into a well defined structure [1]. Serum albumins are the most abundant transport protein in the circulatory system, found in blood plasma, accounting for 60 % of the total serum protein [2-4]. They can bind a wide variety of ligands, e.g., bilirubin, fatty acids, hematin and drugs. In mammals, albumin is synthesized by the liver and possesses a half-life in circulation of 19 days [2, 5]. The main function of serum albumin is to transport metabolites in blood. In human blood serum albumin is present at concentrations in the range of 35 to 45 mg/ml [6], while in the interstitial fluid (tissue fluid) the concentration of albumin is much lower than in the blood [6, 7]. Serum albumin is one of the most studied proteins in the last decades [2, 5]. Bovine serum albumin is a protein commonly used for research purposes due to its stability, water solubility, and versatile binding capacity [2]. Bovine serum albumin has similar effects on human erythrocytes as human serum albumin [9] and it is usually added to simulated body fluids for in vitro tests of biomaterials.

[1] Babeş-Bolyai University, Faculty of Physics & Institute for Interdisciplinary Experimental Research, Cluj-Napoca, Romania
[*] viosimon@phys.ubbcluj.ro

This papers aims to evidence the UV-vis and fluorescence characteristics of as prepared simulated body fluid enriched with low concentrations of bovine serum albumin.

Experimental

Solutions of simulated body fluid (SBF) enriched with bovine serum albumin (BSA) were prepared by adding 0.2 mg – 5 mg of BSA to 1 ml SBF. The SBF obtained according to Kokubo protocol [10] SBF has inorganic ion concentrations similar to those of human extracellular fluid. The ion concentrations of SBF are given on Table 1. The pH of the SBF used in this study was adjusted to pH of 7.40 at 36.5 ^{o}C by using chloride acid.

Table 1.

Ion concentrations of the simulated body fluid and human blood plasma

Ion	Concentration (mmol/l)	
	Simulated body fluid (SBF)	Human blood plasma
Na^+	142.0	142.0
K^+	5.0	5.0
Mg^{2+}	1.5	1.5
Ca^{2+}	2.5	2.5
Cl^-	147.8	103.0
HCO_3^-	4.2	27.0
HPO_4^{2-}	1.0	1.0
SO_4^{2-}	0.5	0.5

The UV spectra were recorded with a Jasco UV-Visible spectrometer V-530 in the spectral range from 240 to 400 nm. Fluorescence measurements were performed on Jasco spectrofluorimeter FP-6300. The excitation wavelength was 295 nm and fluorescence spectra were recorded from 300 to 450 nm.

Results and discussion

The UV-vis spectra (Fig. 1) show that in the fresh prepared solutions the intensity of the absorption band recorded at 278 cm^{-1} increases with BSA concentration. Due to the fact that the absorbance of a solution is directly proportional to the concentration of the absorbing species in the solution and the path length, UV-vis spectroscopy can be used to determine, for a fixed path length, the concentration of the absorber in a solution. It is necessary to know how quickly the absorbance changes with concentration. Proteins contain aromatic amino acid residues like tryptophan, tyrosine, and phenylalanine. The proteins are defined by their unique

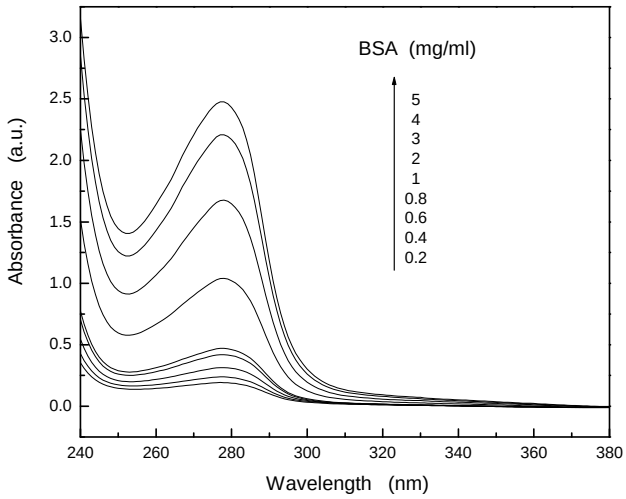

Fig. 1. UV-Vis spectra of as prepared BSA enriched SBF solutions.

sequence of amino acid residues. The 278 nm absorbance band indicates aromatic amino acid residues of proteins [11]. The linear dependence of 278 nm absorbance (Fig. 2) can be used to determine the BSA content in other fresh prepared solutions of different BSA content. The absorbance slope is 0.5 /(mg/ml).

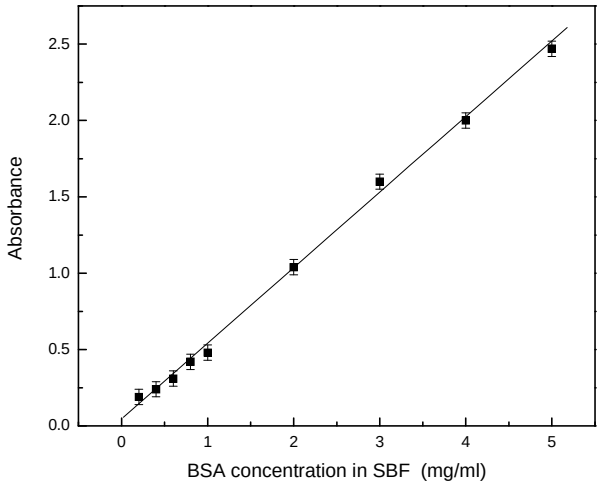

Fig. 2. Dependence of 278 nm absorbance on BSA concentration in SBF as prepared solutions.

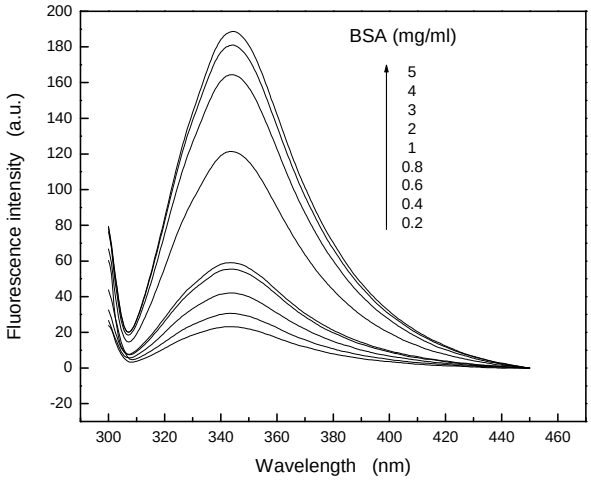

Fig. 3. Fluorescence emission spectra of as prepared BSA enriched SBF solutions.

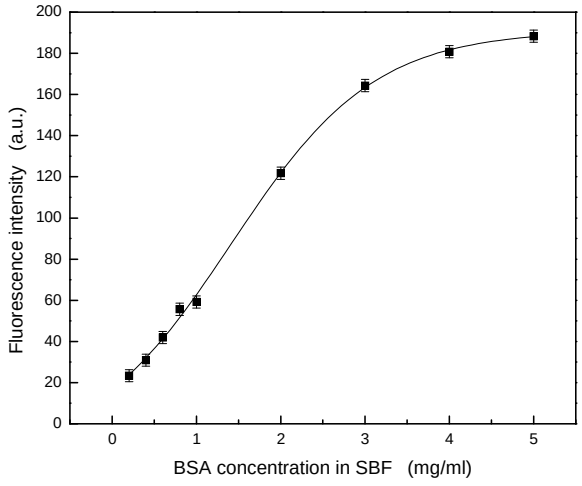

Fig. 4. Dependence of fluorescence intensity on BSA concentration in SBF as prepared solutions.

A similar composition dependence was expected for the fluorescence intensity, but the analysis of fluorescence spectra (Fig. 3) does not confirm it. In this case the experimental data are well fitted with a sigmoidal function (Fig. 4). The sigmoid function, also called logistic function, is described by the equation:

$$y(x) = \frac{1}{1+e^{-x}} \quad (1)$$

The particular sigmoidal function corresponding to Boltzmann sigmoid curve is described by the equation:

$$y(x) = y_2 + \frac{y_1 - y_2}{1+\exp(\frac{x - x^*}{dx})} \quad (2)$$

and is named sigmoidal Boltzmann function. In eq. (2) y_1 is the initial/bottom value, y_2 is the final/top value, x* is the value at halfway between y_1 and y_2, corresponding to inflection point, and dx is the width represented by the change in x corresponding to the most significant change in y values. For the investigated BSA enriched SBF solutions, the fluorescence data show that the point of inflection corresponds to BSA concentration x* = 1.41 mg/ml and dx encompasses a range of 0.85 mg/ml.

UV-vis and fluorescence spectroscopies are complementary techniques. Both imply electronic transitions. Ultraviolet-visible spectroscopy measures transitions from the ground state to the excited state, while the fluorescence spectroscopy measures transitions from the excited state to the ground state. Ultraviolet and visible light promote outer electrons to higher energy levels. The UV-vis spectra are very useful for quantitative measurements, because the concentration of an analyte in solution can be determined by measuring the absorbance at a certain wavelength and applying the Beer-Lambert Law. Based on these results, the data shown in Figure 2 can be used to estimate the concentration of BSA attached on the surface of materials immersed in BSA enriched SBF.

Fluorescence is the observed radiation when an electron makes the transition from the lowest vibrational mode of the electronically excited state to a vibrational mode of the electronic ground state, and the rate of such a transition is in the region of 10^7 to 10^8 s^{-1}. Both bovine serum albumin and human serum albumin excited at 290 nm emit fluorescence attributable mainly to tryptophan residues [12, 13]. In order to explain the changes observed in the dependence of fluorescence intensity on BSA content added to SBF, we have to consider that the intrinsic fluorescence of BSA is due to its tryptophan residues, which have a very high sensitivity to the local environment. Changes in emission spectra of the fluorophore tryptophan provide information on its interaction with the ligand [14].

As can be seen in Fig. 3, the intensity of the fluorescence spectra are not primary dependent on the concentration of BSA, but on the interactions of the fluorophore with the SBF, with respect to water solution and the inorganic species contained therein. One remarks (Fig. 4) a diminished increase of fluorescence signal with increasing protein content. Protein adsorption on various materials has been widely studied and it has been found that electrostatic, hydrophobic and

specific chemical interactions play an important role between protein and the adsorbent materials [15, 16]. For low concentration of surfactants the binding is to specific high energy sites on the protein and the interactions are mainly electrostatic, but hydrophobic contributions are not excluded [2].

When a fluorophore absorbs a photon, an energetically excited state is formed, depending upon the nature of the fluorophore and its surroundings, which finally will loss the energy and return to the ground state. The decrease in fluorescence intensity is called fluorescence quenching and can be caused by several molecular interactions like excited-state reactions, molecular rearrangements, energy transfer, ground state complex formation and collisional quenching [12].

The fluorescence quantum yield is the ratio of photons absorbed to photons emitted through fluorescence, i.e. the quantum yield gives the probability of the excited state to be deactivated by fluorescence rather than by another, non-radiative mechanism. The changes determined by these interactions, in the position or orientation of the BSA tryptophan residues, affect their exposure to solvent, leading to alterations on the fluorescence quantum yield. A diminished fluorescence quantum yield is noticed as BSA concentration in SBF exceeds 1.41 mg/ml.

Two quenching processes are known, static and dynamic quenching. Both of them require molecular contact between the fluorophore and the quencher. Static quenching refers to formation of a nonfluorescent fluorophore–quencher complex. Dynamic quenching refers to the quencher diffusion to the fluorophore during the lifetime of the excited state and upon contact the fluorophore returns to the ground state, without emission of a photon [17]. At the same time, the positions of the two fluorescent tryptophan radicals of BSA are different, one of them is near the surface and the other is deeper and therefore is less accessible to surfactants [18]. In our study, the fluorescence behaviour of the SBF solutions with increasing BSA content indicates that for concentrations higher than 1.41 mg/ml are occurring quenching processes related to the fluorophore interactions with the inorganic species of SBF and molecular rearrangements of tryptophan residues in the SBF solvent.

Conclusions

The linear increase of absorbance in UV-vis spectral region of bovine serum albumin added up to 5 mg/ml to simulated body fluid, with inorganic ion concentrations similar to those of human extracellular fluid, can be used to evaluate the protein concentration in solution. The fluorescence of the same solution has a nonlinear response to increase of the BSA protein concentration. The composition dependence of fluorescence intensity in the investigated BSA concentration range is well fitted with the sigmoidal Boltzmann function, with the point of inflection at 1.41 mg/ml BSA in SBF. This denotes the diminishing of fluorescence quantum yield for higher BSA concentration.

REFERENCES

1. B. Alberts, D. Bray, K. Hopekin, A. Johnson, J. Lewis, M. Raff, K. Roberts, P. Walter, Essential Cell Biology, 2nd ed., Garland Science, New York, 2004.
2. E.L. Gelamo, M. Tabak, Spectrochim. Acta A, 56 (2000) 2255.
3. D. Carter, B. Chang, J.X. Ho, K. Keeling, Z. Krishnasami, Eur. J. Biochem. 226 (1994) 1049.
4. S. De, A. Girigoswami, S. Das, J. Colloid Interf. Sci., 285 (2005) 562.
5. J.R. Brown, P. Shockley, Lipid–Protein Interactions, vol. 1, Wiley, New York, 1982.
6. L.F. Steel, M.G. Trotter, P.B. Nakajima, T.S. Mattu,G. Gonye, T. Block, Mol. Cell. Proteomics 2 (2003) 262.
7. M. Ellmerer, L. Schaupp, G.A. Brunner, G. Sendlhofer, A. Wutte, P. Wach, T. R. Pieber, Am. J. Physiol.-Endocr. Metab., 41 (2000) E352.
8. S. Thijssen, G.Wystrychowski, L. Usvyat, P. Kotanko, N.W. Levin, J. Renal Nutr., 17 (2007) 70.
9. A.W. Jay, Biophys. J., 15 (1975) 205.
10. T. Kokubo, H. Kushitani, S. Sakka, T. Kitsugi, T. Yamamuro, J. Biomed. Mater. Res. 24 (1990) 721.
11. M.G. Mason, A.S. Ball, B.J. Reeder, G. Silkstone, P. Nicholls, M.T. Wilson, Appl. Environ. Microbiol., 67 (2001) 4512.
12. Y.J. Hu, Y. Liu, Z.B. Pi, S.S. Qu, Bioorg. Med. Chem. 13 (2005) 6609.
13. A. Sulkowska, J. Mol Struct., 614 (2002) 227.
14. C. Sun, J. Yang, X. Wu, X. Huang, F. Wang, S. Liu, Biophys. J., 88 (2005) 3518.
15. S . Patil, A. Sandberg, E. Heckert, W. Self, S. Seal, Biomaterials, 28 (2007) 4600.
16. H.S. Mansur, R.L. Oréfice, W.L. Vasconelos, Z.P. Lobato, L.J.C. Machado, J. Mater. Sci. Mater. Med. 16 (2005) 333.
17. Lakowicz JR. Principles of Fluorescence Spectroscopy. New York: Plenum Press; 1983.
18. T. Peter, Adv. Protein. Chem. 37 (1985) 161–169.

STUDIA UNIVERSITATIS BABES-BOLYAI, PHYSICA, LIV, 1, 2009

SPECIFIC SURFACE AREA OF HEAT TREATED ILLITIC MINERAL CLAY

A. VULPOI[1], C. IONESCU[2], V. SIMON[1*]

ABSTRACT. Pristine clay samples were characterized by X-ray diffraction, differential thermal analysis and gravimetric thermal analysis, as well as by nitrogen adsorption/desorption method for specific surface area determination. The samples were thermally treated at different temperatures, up to 1200oC, and for different periods of time, up to 8 hours, in order to investigate the effect of heat treatment parameters on their porosity. The heat treatment applied for 2 hours at 1200oC leads after cooling to dark brown blackish colour, glassy structure and negligible specific surface area.

Keywords: Illite mineral clay, specific surface area, heat treatment effects.

Introduction

The illite, a hydrated potassium-iron-aluminum silicate, is one of the major component of clays used for the production of traditional ceramics, the understanding of its high temperature transformations is of paramount importance for the knowledge of the structural and micro structural properties of fired ceramic products [1]. Illites have their origin in micas, usually muscovite, which is inherited in the soil sequence from the source materials from witch the soil is formed. Most of the general studies describing illite genesis in this manner show large mica flakes breaking into smaller particles until they become clay-sized.

In studies of soil genesis, the illites occurring in the soil are often found to be unstable. This transformation of illites in other less potassic minerals is observed in various types of soil-forming environments. Nevertheless, illite is sufficiently abundant in some cases to warrant a place in soil classification and terminology [2]. Illite clays are also investigated for their potential applications for microbial reduction of iron [3]. Other interesting studies are focussed on the role of microbes in the smectite-to-illite transformation based on a bioreaction [4].

* viosimon@phys.ubbcluj.ro
[1] Babeş-Bolyai University, Faculty of Physics & Institute for Interdisciplinary Experimental Research, Cluj-Napoca, Romania
[2] Babeş-Bolyai University, Faculty of Biology and Geology

Clay materials with controlled porosity found applications in the water treatment by the membrane separation techniques. According to their diameters of the pores, they can be used either as membranes of microfiltration or like supports for membranes of ultrafiltration [5].

In this work we investigate panonian age illite clay from Odorheiul Secuiesc region used to obtain the traditional Marginea black-ceramic, with respect to the changes in surface area induced by increasing heat treatment temperature and duration.

Experimental

The samples are natural clays extracted from the soil from Transylvania, Odorheiul Secuiesc region. The samples were modeled in biscuit forms and cured at different temperatures. After curing the samples were crushed until we obtained a fine powder. Before curing it was made X-ray diffraction analysis (XRD), differential thermal analysis (DTA) and DTG curves. The samples were heat treated at temperatures ranging between 700°C and 1100°C for 2, 4 and 8 hours, as well as at 1200°C for 5 minutes and for 2 hours. Specific surface areas of the pristine and thermally treated samples were determines using BET (Brunauer, Emmett and Teller) method.

BET theory is a well-known rule for the physical adsorption of gas molecules on a solid surface, that is basis for an important analysis technique for the measurement of the specific surface area of a material [6]. The concept of the theory is an extension of the Langmuir theory, which is a theory for monolayer molecular adsorption, to multilayer adsorption with the following hypotheses: (a) gas molecules physically adsorb on a solid in layers infinitely; (b) there is no interaction between each adsorption layer; and (c) the Langmuir theory can be applied to each layer. The resulting BET equation is:

$$\frac{1}{v[(P_0/P)-1]} = \frac{c-1}{v_m \cdot c} \cdot \frac{P}{P_0} + \frac{1}{v_m \cdot c} \qquad (1)$$

where P and P_0 are the equilibrium and the saturation pressure of adsorbates at the temperature of adsorption, v is the adsorbed gas quantity (for example, in volume units), and v_m is the monolayer adsorbed gas quantity, c is the BET constant expressed by:

$$c = \exp\left(\frac{E_1 - E_L}{RT}\right) \qquad (2)$$

E_1 is the heat of adsorption for the first layer, and E_L is that for the second and higher layers and is equal to the heat of liquefaction [6].

The XRD spectra were recorded with a Shimadzu XRD-6000 diffractometer, using Cu K_α radiation (λ=1.5418 Å), with Ni-filter. The measurements were performed at a scan speed of 7 º/min.

The differential thermal analysis (DTA) and gravimetric thermal analysis (GTA) were performed on Shimadzu analyzer DTG-60H witch simultaneously measures TG and DTA, in air, using alumina crucibles, with hitting rate of 10 ºC/min, from room temperature to 1300 ºC.

The Specific Surface Area measurements were made with a Qsurf 9600 Series Surface Analyzer, working on the single point BET principle, using a single gas mixture 30% N_2 in helium equilibrium.

Results and discussions

The XRD pattern shown in Fig. 1 indicates that the pristine sample consists in a mixture of illite quartz and muscovite crystals [7]. The DTA curve (Fig. 2) exhibits three endothermic peaks at 53.88 ºC, 689.53 ºC and 1201.16 ºC. The first one is due to water physisorbed on the clay and it is accompanied by a weight loss peak in the DTG curve. The second peak indicates the destruction of illite by dehydroxylation [1, 8], this peak gives a weight loss in the range of 440–740°C. The third peak represents the melting of the sample.

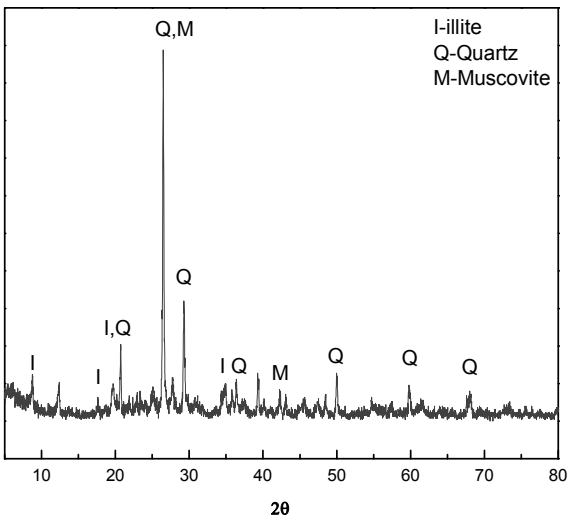

Figure 1. XRD spectrum of the pristine clay sample.

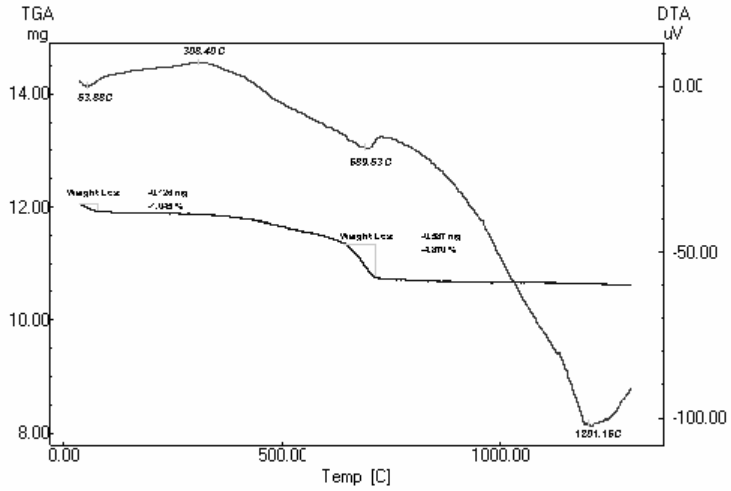

Figure 2. DTA/DTG curves of the pristine illite sample.

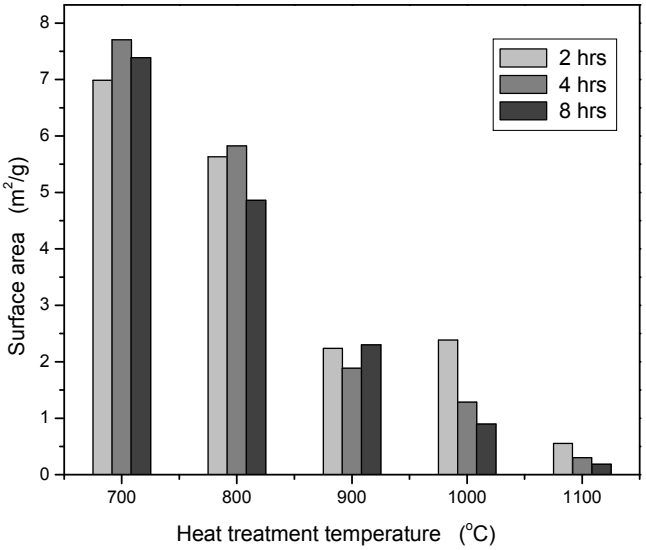

Figure 3. Dependence of specific surface area on heat treatment temperature.

To follow the change of materials porosity during heat treatment, the specific surface area (SSA) was measured. The illite-based materials were treated at different temperatures: 700ºC, 800ºC, 900ºC, 1000ºC, 1100ºC, 1200 ºC, each for

different period of time: 2 hours, 4 hours and 8 hours, except for the sample treated at 1200ºC, because this temperature is the melting temperature of the sample as sown in the DTA curve. At this temperature the sample was treated 2 minutes and 2 hours. The measured SSA for untreated and heat treated samples are presented in Table 1.

Table 1.

Specific surface areas obtained with nitrogen adsorption BET method

Sample code	Curing temperature (ºC)	Curing time (hours)	SSA (m^2/g)
01	0	0	16.1950
1-A	700	2	6.9855
1-B		4	7.7043
1-C		8	7.3863
2-A	800	2	5.6312
2-B		4	5.8263
2-C		8	4.8590
3-A	900	2	2.2342
3-B		4	1.8862
3-C		8	2.2984
4-A	1000	2	2.3874
4-B		4	1.2874
4-C		8	0.8934
5-A	1100	2	0.5553
5-B		4	0.2977
5-C		8	0.1864
6-A	1200	0.1	0.1094
6-B		2	0.0585

The specific surface area obtained for the de pristine clay is 16.1950 m^2/g. The data show a tendency for SSA to decrease with temperature of heat treatment. According to the values summerised in Table 1, by heat treatment at 700ºC the clay looses more than a half of the specific surface area, and SSA decreases from 16.1950 m^2/g to 6.9855 m^2/g. The higher the firing temperature the smaller the specific surface area becomes and with that the denser and less porous the material becomes, and it were more and more difficult to ground. The sample treated at 1200ºC for 2 hours has a dark brown blackish colour after cooling, it achieves a glassy structure and an insignificant specific surface area, as can be seen in Table 1. Another sample was heat treated at 1200ºC only for 5 min. After cooling it has a blackish colour too, contains lot of holes and looks like a hard sponge.

The colour of the samples depend on heat treatment temperature. The pristine clay was gray, after treatment at 700ºC it changed the colour to reddish orange, like oxidized iron, and for higher treatment temperatures the samples became darker, to almost black for heat treatments applied at 1200ºC.

Conclusions

The primary clay consists in a mixture of illite quartz and muscovite crystals. Its melting temperature is close to 1200ºC. The increase of heat treatment temperatures up to 1200^{o}C changes the specific surface area of pristine clay, 16.1950 m^2/g, to the midget value of 0.0585 m^2/g, denoting a very low porosity of high temperature heat treated clay samples. The colour change from gray to black proves that the Marginea ceramic is obtained under high temperature firing conditions of the clay ore.

Acknowledgements: The present work was partially supported by the scientific research project PNII 2241/2008 the Romanian Excellence Research Program.

BIBLIOGRAPHY

1. A. F. Gualtieri, S. Ferrari, Phys.Chem. Miner., 33 (2006) 490.
2. A. Meunier, B. Velde, Illite: origins, evolution, and methamorphism, Springer, 2004.
3. J.L. Seabaugh, H. Dong, R.K. Kukkadapu, D. D. Eberl, J.P. Morton, J. Kim, Clay Clay Miner., 54 (2006) 67.
4. J. Kim, H. Dong, J. Seabaugh, S.W. Newell, D.D. Eberl, Science 303 (2004) 830.
5. Y. Anbri, N. Tijani, J. Coronas, E. Mateo, M. Menéndez, J. Bentama, Desalination 221 (2008) 419.
6. S. Brunauer, P.H. Emmett, E. Teller, J. Am. Chem. Soc., 60 (1938) 309.
7. R.J. Gibbs, Clay Miner., 7 (1967) 79.
8. A. Shvarzman, K. Kovler, I. Schamban, G. S. Grader, G. E. Shter, Adv. Cem. Res., 14 (2002) 35.

STUDIA UNIVERSITATIS BABES-BOLYAI, PHYSICA, LIV, 1, 2009

THEORETICAL ANALYSIS OF PHOTONIC CRYSTAL CAVITIES FROM CORE-SHELL NANO-SIZED ELEMENTS

M. GILOAN[1,*], S. ASTILEAN[2,*]

ABSTRACT. In this paper we analyze the possibility of designing photonic crystal cavities based on core-shell nanoelements. Computer simulations show that different resonant frequencies can be achieved by changing the geometry of the cavity.

Keywords: photonic crystal cavities, core-shell nanoelements, simulations

Introduction

The ability to design materials at nanoscale allows the production of devices with useful properties for light confinement. One of the goals is to control the optical properties of materials. An enormous range of technological developments would become possible if we could engineer materials that respond to light waves over a desired range of frequencies by perfectly reflecting them, or allowing them to propagate only in certain directions, or confining them within a specified volume. It was demonstrated that a material with such properties can be produced by periodically arranging macroscopic media with differing dielectric constants. By analogy with a classic crystal, a periodic arrangement of atoms and molecules, such a material is called a photonic crystal (PhC). Periodic structured materials can inhibit the propagation of light over a certain band of wavelengths, while allowing other bands to propagate [1]. This specific behavior may give rise to a "photonic bandgap" (PBG), which is analogous to the electronic bandgap in semiconductor materials. Within the bandgap of a photonic crystal no modes are allowed. The density of states, the number of possible modes per unit frequency, is zero. By altering the periodicity of a photonic crystal, we can create localized optical modes that have frequencies within the gap. These optical modes are confined in the vicinity of defects as a result of coherent scattering and interference of waves from the surrounding periodic structure. When the perturbation of the regular photonic crystal lattice takes the form of a point the resulting device may be used as a resonant cavity [2].

Optical resonant cavities, which trap light within a finite volume, are an essential component of many important optical devices. Cavities are characterized

[1] "Investeşte în oameni!" doctorand bursier în "Proiect cofinanţat din Fondul Social European prin Programul Operaţional Sectorial Dezvoltarea Resurselor Umane 2007-2013"

[2] email: sastil@phys.ubbcluj.ro

[*] Babes-Bolyai University, Institute for Interdisciplinary Experimental Research, Nanobiophotonics Center, T. Laurian 42, 400271 Cluj-Napoca, Romania

by two main quantities: the modal volume V and the quality factor Q. In many applications high Q's and small V's are highly desirable for high Purcell factor required for controlling the coupling between a quantum emitter, an atom or a semiconductor self-assembled quantum dots, placed in resonance with the nanocavity mode [3 - 5]. For an emitter perfectly coupled to the cavity the Purcell factor is given by $F_P = (3/4\pi^2)\ (Q/V)\ (\lambda/n)^3$ where Q is the cavity quality factor, V is the cavity volume, λ the wavelength of the given transition, and n the refractive index [8].

Over the past few years, an increased attention was paid to studying the interaction between a quantum emitter and a single-field radiation mode. In order to achieve the strong coupling regime between the nanocavity resonant mode and the quantum emitter, we have two alternatives. We can choose as quantum emitter a quantum dot with desirable spectral properties or we can tune the resonant frequency of photonic crystal nanocavity to match the quantum dot exciton frequency [6, 7]. In this work we analyze theoretically the resonant modes of photonic crystal cavities made up from nano-sized core-shell elements. Our results show that the resonant mode frequency can be tuned by changing the size of the central core-shell elements.

Theoretical analysis

In our analysis, we considered a two-dimensional photonic crystal build up from core-shell nanoelements. The photonic crystal consists of a dielectric slab, with a refractive index equal to 3.4, patterned with a hexagonal array of core shell nanoelements, having the lattice parameter, denoted by *a*, equal to 200 nm. The photonic crystal structure is shown in Fig. 1 a). We considered a refractive index equal to 1.45 for the core and a refractive index equal to 2.4 for the shell of the core-shell nanoelements. The inner radius of the core-shell nanoelements is equal to 70 nm and the thickness of the shell is equal to 10 nm. Figure 1 b) shows a cross section through a core-shell element.

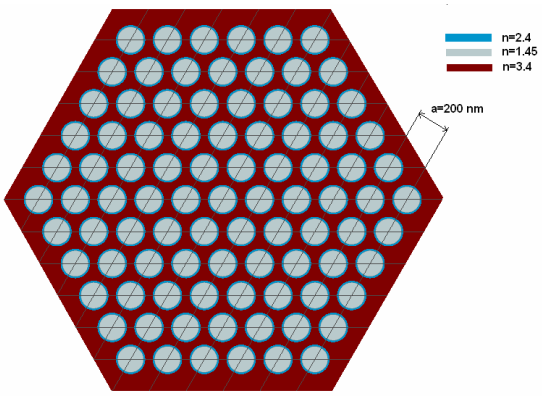

Figure 1. a) Photonic crystal made of core-shell elements in a hexagonal lattice.

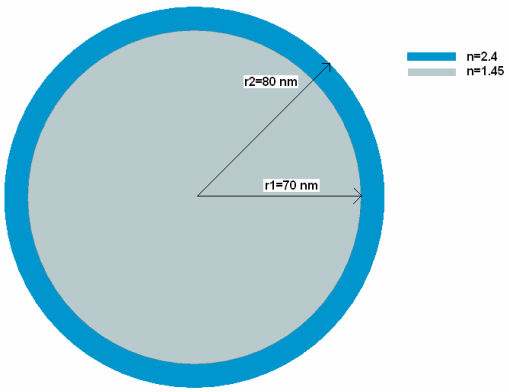

Figure 1. b) Core-shell nanoelement used to design photonic crystal

A resonant cavity can be made by introducing a point defect in a photonic crystal. The defect is obtained by locally modifying the shape, size, or refractive index of the photonic crystal features. Photonic crystal cavities analyzed in this paper are formed by introducing point defects consisting in removing a core-shell nanoelement from the hexagonal lattice and changing the inner radius and the thickness of those six nanoelements surrounding the removed one. Figure 2 a) shows a nanocavity obtained using the method presented above. By removing the central nanoelement the refractive index in the center of the cavity will increase to 3.4 the same value as for the rest of the dielectric slab. Also, we changed the inner radius of the nonoelements placed on the vertices of the central hexagon to 20 nm while maintaining the thickness equal to 10 nm. Combining different values for the inner radius of the central nanoelements, 20, 30, 40, and 50 nm with different values for the thickness of the central nanoelements, 10, 20, and 30 nm, we designed twelve distinct nanocavities.

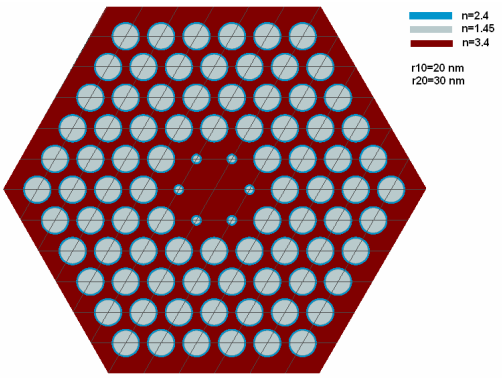

Figure 2. a) Resonant cavity made by introducing a point defect in a photonic crystal

Computer simulations were performed to find the resonant frequencies of the resulting cavities. In these simulations we used the finite difference time domain method (FDTD) [9]. The FDTD method has become the state-of-the-art method for solving Maxwell's equations in complex geometries. It gives both time domain and frequency domain information to the user, offering unique insight into all types of problems and applications in electromagnetics and photonics. To perform our simulations we used the Lumerical FDTD Solutions software [10]. In our simulations we used a source of electromagnetic radiation placed in the middle of the cavities. The source was a magnetic dipole with a transversal electric (TE) polarization. Figure 3 shows the distribution of source intensity versus wavelength and frequency. The source has the central frequency f_0=550 THz and a frequency span Δf=500 THz. The response of the cavity depicted in Fig. 2 a) is presented in Fig. 2 b). It shows a resonance at frequency f_R=458 THz corresponding to a free space wavelength λ_R=654 nm.

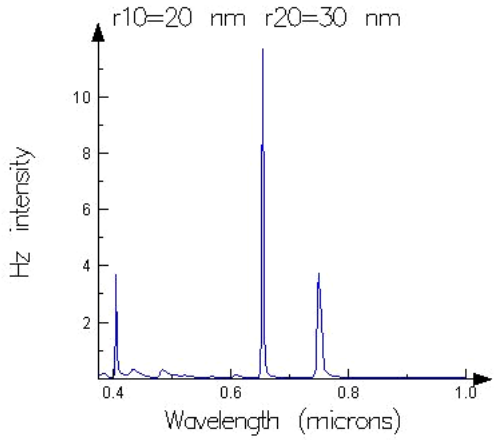

Figure 2. b) The response of the resonant cavity depicted in Fig. 2.a) shows a resonance at λ_R=654 nm

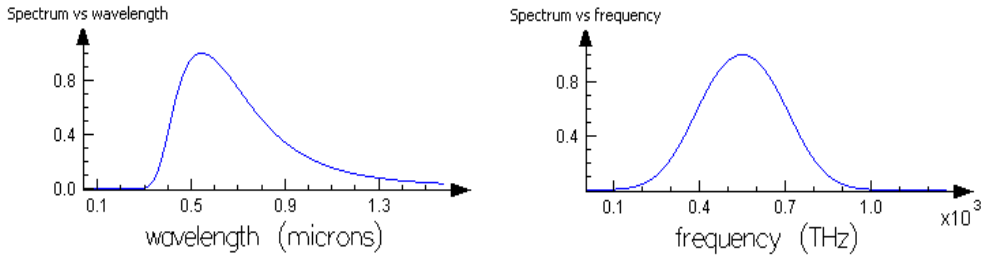

Figure 3. Spectral distribution of the source used in simulations

Results and discussion

Designing photonic crystal cavities with specific resonant frequencies and high quality factor is desirable when such cavities are used to enhance energetic transitions of a system accompanied by emission or absorption of a photon at a particular frequency. In many experiments, quantum dots were used as light emitters and photonic crystal cavities as single light-field mode systems. A strong coupling between the quantum emitter and the resonant cavity can be achieved by precisely matching their frequencies. Also it is required for the quantum emitter, placed inside the cavity, to overlap the maximum of the field intensity inside the cavity [1].

We analyzed the frequency response of twelve photonic crystal cavities based on core-shell nanoelements. Each simulation was performed with the same electromagnetic source described in the previous section. Simulation results shows that the resonant frequencies of a cavity can be tuned by changing the inner radius or the thickness of the central nanoelements. Figure 4 a) – c) shows the magnetic field intensity H_Z graphs with respect to the wavelength of the radiation in free space for different cavities.

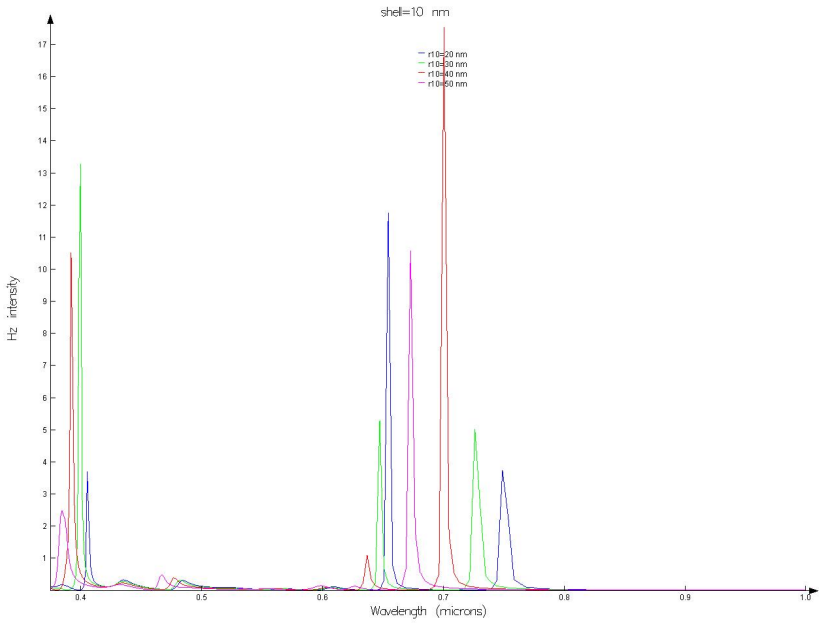

Figure 4. a) H_Z intensity graphs with respect to free space wavelength of four cavities having the following parameters of the central nanoelements: shell thickness 10 nm, inner radius r_{10}=20 nm (blue), r_{10}=30 nm (green), r_{10}=40 nm (red), and r_{10}=50 nm (magenta)

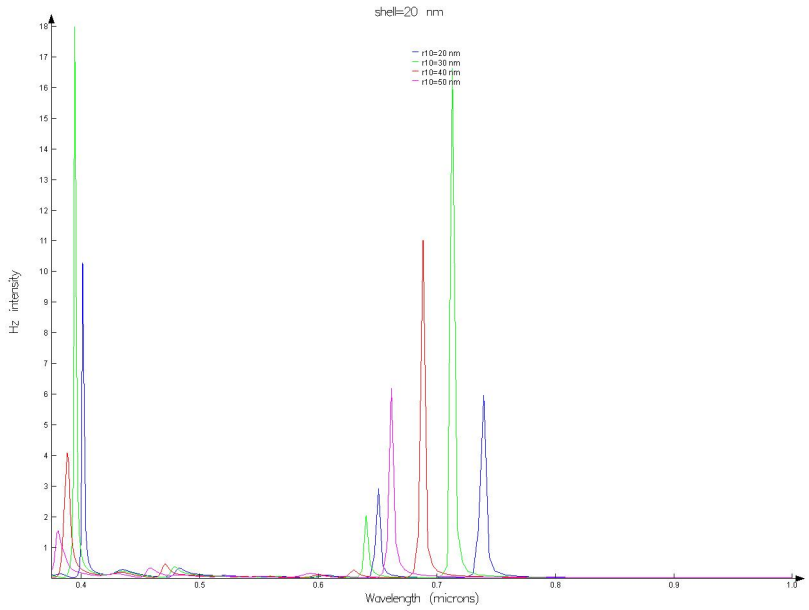

Figure 4. b) H_Z intensity graphs with respect to free space wavelength of four cavities having the following parameters of the central nanoelements: shell thickness 20 nm, inner radius r_{10}=20 nm (blue), r_{10}=30 nm (green), r_{10}=40 nm (red), and r_{10}=50 nm (magenta)

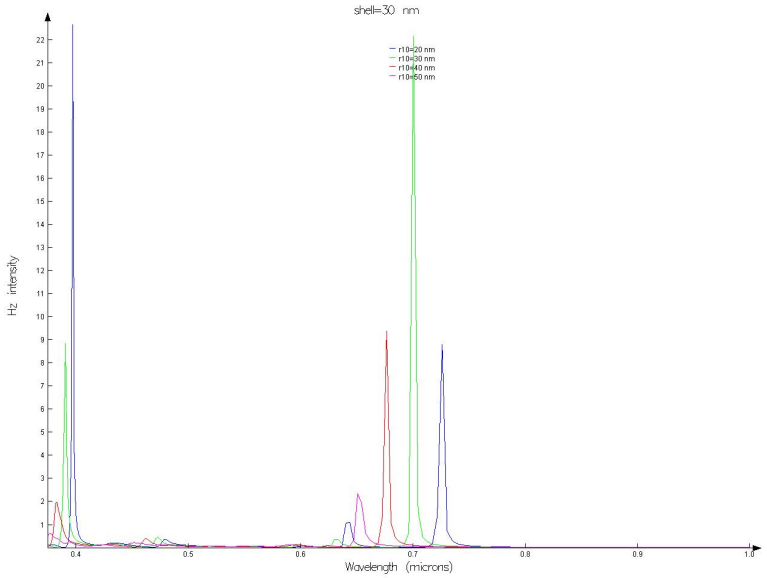

Figure 5. c) H_Z intensity graphs with respect to free space wavelength of four cavities having the following parameters of the central nanoelements: shell thickness 10 nm, inner radius r_{10}=20 nm (blue), r_{10}=30 nm (green), r_{10}=40 nm (red), and r_{10}=50 nm (magenta)

Conclusions

In this paper we analyze photonic crystals built up from core-shell nanoparticles. Using this particular approach we designed photonic crystal cavities capable to host the desired photonic mode. Resonant modes of photonic crystal cavities where studied by performing computer simulations using finite difference time domain (FDTD) method. The geometry of the nano-sized constituent elements of the photonic crystal cavity influence the resonant frequencies of the cavity. Changing the dimensions of the central nanoelements of the cavity one can tune the resonant frequencies to match a particular value.

REFERENCES

1. J. D. Joannopoulos, S. G. Johnson, J. N. Winn, R. D. Meade "*Photonic Crystals Molding the Flow of Light*" second edition, Princeton University Press, 2008
2. D. W. Prather, S. Shi, A. Sharkawy, J. Murakowski, G. J. Schneider "*Photonic Crystals Theory, Applications, and Fabrication*" Wiley, 2009
3. T. F. Krauss "Photonic Crystals: Cavities without leaks" Natures Materials Vol. 2, December 2003
4. H. Benisty, "Photonic Crystals: New designs to confine light" Nature Physics, Vol. 1, October 2005
5. D. Englund, I. Fushman, and J. Vuckovic, "General recipe for designing photonic crystal cavities" Optics Express, 5961, 8 August 2005 / Vol. 13, No. 16
6. J. Vuckovic, M. Loncar, H. Mabuchi, and A. Scherer "Design of photonic crystal microcavities for cavity QED" Physical Review E, Vol. 65, 21 December 2001
7. K. Hennessy, A. Badolato, M. Winger, D. Gerace, M. Atature, S. Gulde, S. Falt, E. L. Hu, and A. Imamoglu, "Quantum nature of a strongly coupled single quantum dot–cavity system" Nature, 445, 896-899, 2007
8. M. Munsch, A. Mosset, A. Auffeves, S. Seidelin, J. P. Poizat, J.-M. Gerard, A. Lemaitre, I. Sagnes, and P. Senellart, "Continuous-wave versus time-resolved measurements of Purcell-factors for quantum dots in semiconductor microcavities" HAL: hal-00391093, version 1, 1-3 Jun 2009, http://hal.archives-ouvertes.fr
9. K. S. Yee, "Numerical solution of initial boundary value problems involving maxwell's equations in isotropic media" IEEE Trans. Antennas Propagat., vol. AP-14, pp. 302-307, 1966
10. Lumerical Solutions, Inc. "*FDTD Solutions User Manual*" Release 6.0 https://www.lumerical.com

STUDIA UNIVERSITATIS BABES-BOLYAI, PHYSICA, LIV, 1, 2009

SEA BUCKTHORN OIL STUDY BY GC/MS AND IR

CORNELIA MESAROS[1], ANDREEA IORDACHE[1], MONICA CULEA[1], CORA CRĂCIUN[1], ONUC COZAR[1], RADU FECHETE[2], EUGEN CULEA[2]

ABSTRACT. A sensitive analytical method, very useful for determination of fatty acids, vitamin F and E and sterols, in biological samples, was developed by gas chromatography/ mass spectrometry (GC/MS). The method was applied for testing fatty acids, vitamin E, sterols, after the treatment of sea buckthorn oil (Hippophäe rhamnoides L) at different kGy doses with accelerated electrons. The internal standard used for fatty acid methyl esters determination was C11:1. Liposoluble compounds from sea buckthorn oil represent a polivitaminic complex with regenerator action upon the cellular metabolism. Our method is suitable for fatty acid screening and quantitative determination and to state the changes of the nutrients after treatment with accelerated electron. GC/MS analyses were performed on a Trace DSQ. Comparisons with other methods, as HPLC and by IR for sea buckthorn oil changes are presented.

Keywords: GC/MS analyses , sea buckthorn oil, fatty acid

Introduction

Sea buckthorn (*Hippophae rhamnoides)* is a wild shrub producing berries, widely found in Asia and Europe [1]. Besides naturally growing plants, sea buckthorn hybrids of different subspecies are cultivated in order to prevent desertification, since it forms strong root and it is resistant to extreme temperature, drought and poor soil [2]. There is a long tradition in Asia for using sea buckthorn berries in folk medicine. It was demonstrated that the oils extracted from flesh and seeds have regenerating, anti-inflammatory, anti-ulcerogenic, hepatoprotective, cytoprotective properties [3-5]. Sea buckthorn berries are exceptionally rich in both lipophilic and hydrophilic bioactive compounds and represent an important resource for pharmacy and food industry [6, 7]. An impressive number of studies were dedicated to the oil content and fatty acids composition of pulp and seeds. The pulp oil has a special composition with a very high content of unusual palmitoleic acid (up to 54 % of total fatty acids),

[1] Babes-Bolyai University, Biomedical Physics Dept., 1 Kogalniceanu str, 3400 Cluj-Napoca, Romania
e-mail: mculea@phys.ubbcluj.ro
[2] Technical University of Cluj-Napoca, 15 Daicoviciu Str, 400020 Cluj-Napoca, Romania
eugen.culea@phys.utcluj.ro

while the seeds oil is rich in linoleic and α-linolenic acids [8-13]. Sterols, tocopherols and tocotrienols are other important compounds of sea buckthorn oil, and their content and profile depend on the berries origin, growth condition and oil processing method [13-15].

The aim of this study was to develop a sensitive analytical method for determination of fatty acids, vitamin F and E and sterols in sea buckthorn oil, by gas chromatography/ mass spectrometry (GC/MS). The method was applied for testing the lipophilic compounds after the treatment of sea buckthorn oil (*Hippophäe rhamnoides* L) at different kGy doses with accelerated electrons. Some measurements with other analytical techniques as high performance liquid chromatography (HPLC) and IR are presented.

Materials and method

Methanol was obtained from Merck (Darmstadt, Germany). Standard of fatty acids methyl esters and acetyl chloride was from Fluka (Buchs, Switzerland), α-tocopherol standard was from Sigma-Aldrich (Munich, Germany). All other chemicals were from Comchim (Bucharest). The oil samples were from Hofigal (Bucuresti).

GC-MS

A Trace DSQ ThermoFinnigan quadrupol mass spectrometer coupled with a Trace GC was used. The derivatized fatty acids were separated on a Rtx-5MS capillary column, 30 m x 0.25 mm, 0.25μm film thickness, using a temperature program from 70 ^{o}C (1 min) to 100 ^{o}C, at 20 ^{o}C/min; then 30 ^{o}C/min to 310 ^{o}C. The following conditions were used: transfer line temperature 250^{o}C, injector temperature 200 ^{o}C; ion source temperature 250 ^{o}C; Splitter: 10:1. Electron energy was 70eV and emission current, 100μA.

Fatty acid methyl esters (FAME) were obtained by esterification reaction of known quantities of oil with 100 μl 3M HCl methanol at 100^{o}C for 60 min followed by evaporation to dryness under N_2 stream. 0.5 mg of the internal standard C11:1 was added at 100 μl oil. Then sample was solved in 100 μl DCM or ethyl acetate, and 3 μl were injected into GC-MS.

HPLC analysis of α-tocopherol: The sea buckthorn oil was saponified with 60 % KOH in ethanol, in the presence of ethanol and pyrogallol, at 75°C for 45 min. The sample mixture was extracted with hexane: ethyl acetate (9:1). The organic layer was washed with 5 % sodium chloride solution and then evaporated to dry and dissolved in methanol.

The samples were injected into HPLC system containing LC20 AT Shimadzu pumps and a Waters 990 PDA detector. A Supelco Discovery C18 (25 cm x 4.6 mm, 5 μm particle diameters) HPLC column was used. The mobile phase consisted in methanol: water (98:2) and chromatogram was monitored at 292 nm. Tocopherol identification was based on the retention time of α-tocopherol standard (Sigma) and UV-VIS spectra. Quantitative analysis was done using a calibration curve with α-tocopherol (0.01 - 0.2 mg/ml), r = 0.989.

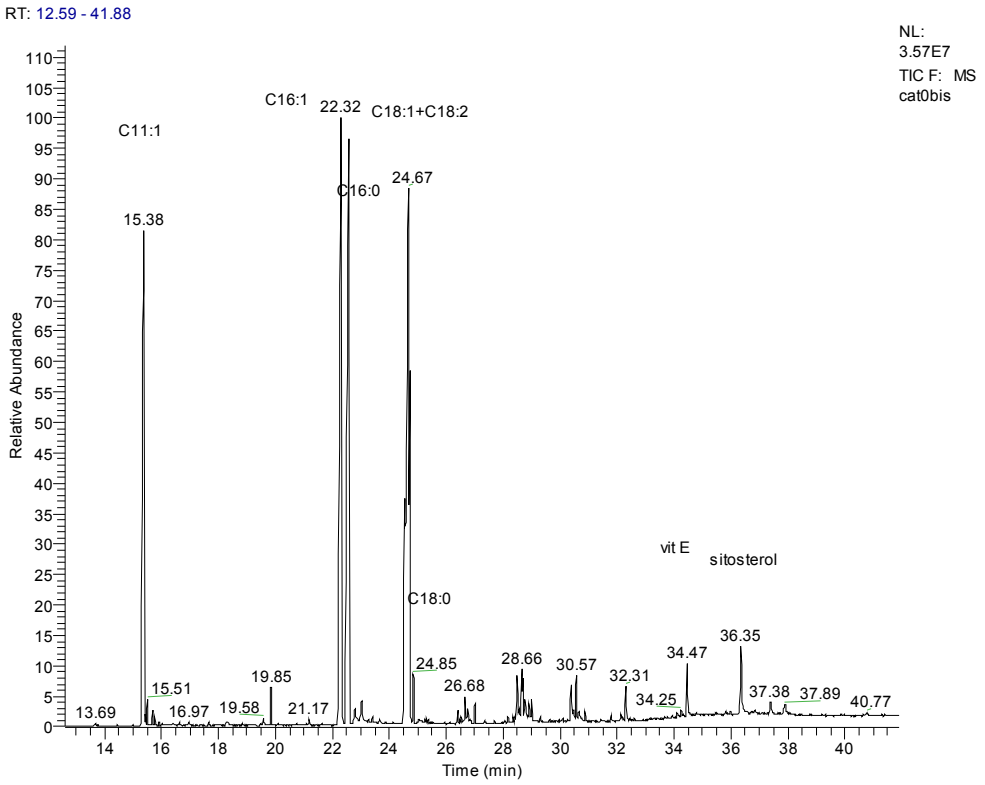

Fig. 1. The chromatogram of separation of sea buckthorn oil FAME by GC-MS

FTIR measurements were performed in the 4000-400 cm^{-1} range, on a Jasco 6200 FT/IR equipment, at room temperature The liquid drops of the sea buckthorn oil were placed between two KBr windows or on the surface of a single window. After recording, FTIR spectra of the samples were corrected by subtraction with a reference spectrum of KBr recorded in the same conditions.

Results and Discussion

The results obtained for the sea buckthorn oil by GC-MS are presented in Table 1. The NIST library was used for compounds identification. In Fig. 2. is presented the variation of the ratio of unsatureated fatty acids (vitamin F) per saturated fatty acids with doses (kGy). The unsaturated fatty acids seems to decrease with applied doses and also vitamin E and sterols (Fig. 3).

Table 1

The compounds identified in sea buckthorn oil by GC-MS

Compounds	**RT(min)**	**area %**
Methyl myristate (C14:0)	19.85	0.79
methyl palmitoleate(C16:1)	22.36	30.68
methyl palmitate(C16:0)	22.63	24.53
methyl oleate +linoleat(C18:1+C18:2)	24.73	37.18
methyl stearate (C18:0)	24.89	0.63
C20:1	26.83	0.55
methyl arachinate (C20:0)	27.01	0.30
C22:1	28.93	0.86
behenic acid methyl ester(C22:0)	29.03	0.22
C24:1	30.57	0.41
methyl lignocerate (C24:0)	30.89	0.14
C26:0	32.31	0.26
vitamine E	34.47	0.60
sitosterol	36.36	2.13
lupeol	37.41	0.42
urs-12-en-28-ol	40.8	0.31

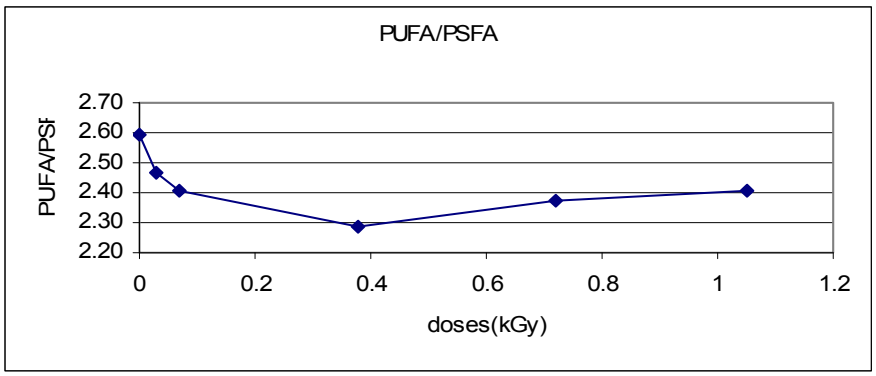

Fig 2. PUSFA/PSFA variation wth applied doses

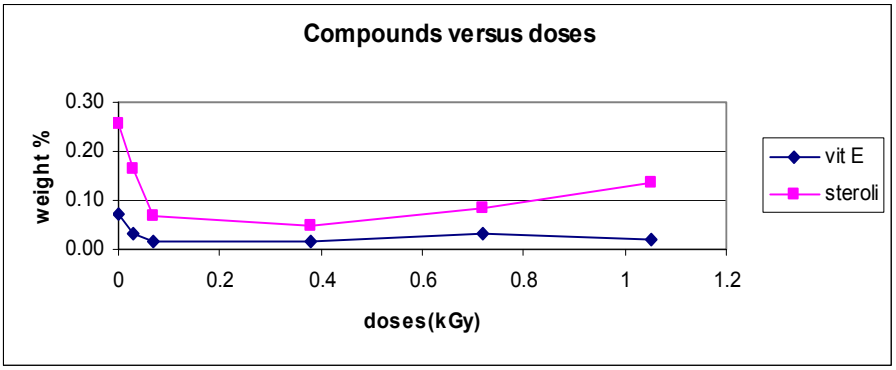

Fig. 3. Vitamin E and sitosterol (% weight) versus applied doses (GC-MS determination)

In Table 2 and Fig. 4 are presented the values measured by HPLC for vitamin E in the oil samples versus doses. Vitamin E is considerably affected by doses of radiation.

Table 2.

Vitamin E determination by HPLC at different doses (kGy)

Dose (kGy)	α-tocopherol mg/100 ml oil
0	57.75
0.03	50.52
0.07	29.1
0.38	26.8
0.72	25.9
1.05	25.8

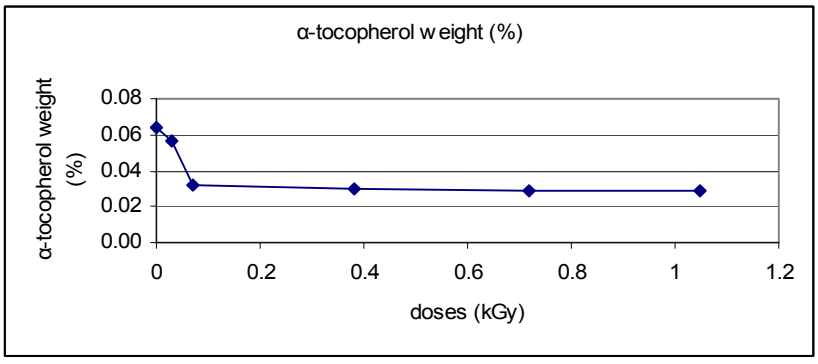

Fig. 4. Vitamin E variation (% weight) versus applied doses (HPLC measurements)

According to the composition of the sea buckthorn oil, the main contribution to the IR spectrum is given by K and E vitamins, carotenoids, sterols and fatty acids [16]. Fatty acids are carboxylic acids with saturated or unsaturated unbranched aliphatic chain. Saturated fatty acids present only simple C-C bonds along their chain. Except the carbon atom from the carboxylic group –COOH, all the other carbons are saturated (contain in their coordination sphere as many hydrogens as possible). In unsaturated fatty acids, one or more singly-bonded $–CH_2–CH_2–$ groups of the chain are replaced by doubly-bonded –CH=CH– groups [17]. In general, the main difference between the IR spectra of fatty acids is due to the presence for unsaturated acids of the stretching vibration ν(C=C) at 1640-1680 cm^{-1}, which is missing for saturated acids.

The sea buckthorn oil contains both saturated and unsaturated fatty acids, their content depending on the source of the oil (the pulp, seeds or the total fruit), the extraction type and the condition of storing [18]. The most abundant saturated acids are: the palmitic (C16:0), stearic (C18:0) and myristic (C14:0), which differ by the length of the main chain $(CH_2)_n$ and therefore, their IR spectra are similar. They contain vibration bands in the regions 2850-3000 cm^{-1} (ν(C-H)), 2500-3300 cm^{-1} (ν(O-H)), 1450-1500 cm^{-1} (δ(C-H)+ δ(O-H)), 1200-1300 cm^{-1} (ν(C-O)), 900 cm^{-1} (for the long chain $(CH_2)_n$).

Some of the most abundant unsaturated acids in the sea buckthorn oil are: palmitoleic (C16:1(n-7)), oleic (C18:1(n-9)), vaccenic (C18:1(n-7)), linolenic (C18:3(n-3)), α-linoleic (C18:2(n-6)), myristoleic (C14:1(n-5)). Compared to the saturated acids, IR spectra of the unsaturated acids show splitting of the bands at 1450-1500 and 1200-1300 cm^{-1} and present the band corresponding to ν(C=C) stretching vibration at 1640-1680 cm^{-1}. From the unsaturated acids, the ν(C=C) vibration is strongest for the linolenic acid, due to its three –CH=CH– groups. The linolenic acid also distinguishes from the other fatty acids by its band of medium intensity appearing at ≈ 700 cm^{-1}. The vitamins K and E, the sterols (in the sea buckthorn oil, from the most abundant sterols are β-sitosterol, erithrodiol, β-amirol) contain aromatic, OH, C=O groups and chains of simple C-C and double C=C bounds. The vibrations of all these functional groups superpose on those of the fatty acids.

Fig. 5 presents the FTIR spectra obtained for a reference non-irradiated sample of sea buckthorn oil (a) and for three samples irradiated at increasing doses of accelerated electrons radiation. The most important changes in the IR spectra after irradiation of the samples is seen in the ν(C=C) (≈ 1640 cm^{-1}) and ν(C-H) (2850-3000 cm^{-1}) regions. The intensity of the ν(C=C) band decreases by irradiation, but not monotonous with the radiation dose. These decrease can arise from the breaking of C=C double bonds in some constituents of the sea buckthorn oil (unsaturated fatty acids, K and E vitamins, sterols, carotenoids). In general, aromatic C=C bounds present stretching vibrations (weak) at 1600 and 1500 cm^{-1}, which for the

sea buckthorn oil are very small, are hidden by the ν(C=C) vibration at ≈ 1640 cm^{-1}. This shows that the C=C bonds that are broken down by the radiation most likely belongs to the long chains of the molecules.

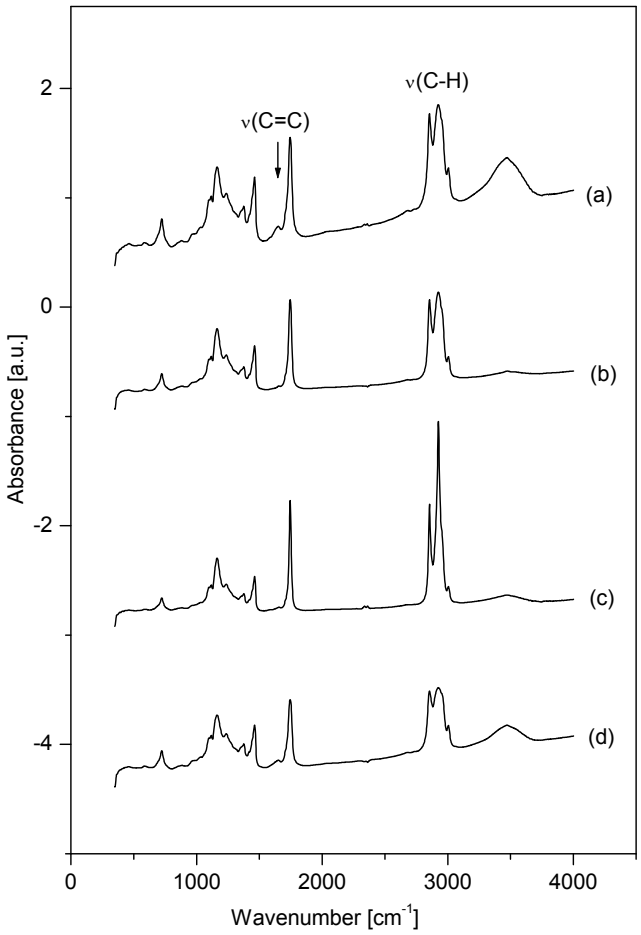

Fig. 5. FTIR spectra of the sea buckthorn oil: non-irradiated sample (a) and irradiated samples at 1.12 kGy (b), 2.73 kGy (c) and 5.23 kGy (d)

Conclusions

GC-MS, HPLC and IR methods developed showed significant changes of vitamins with doses in the study of fatty acids, vitamin E and sterols after the treatment of sea buckthorn oil at different kGy doses with accelerated electrons. Optimisation of treatment for decontamination of oil is necessary to avoid loses of its important nutrients

REFERENCES

1. A. Roussi, Annales Botanici Fennici, 8, 177 (1971).
2. W. Xiufeng, L. Jian, *Proceeding of the 1st Congress of the International Seabuckthorn Association, Berlin*, 2003, p. 54.
3. S. Geetha, M. Sai Ram, V. Singh, G. Ilavazhagan, R.C. Sawhney, J. Ethnopharmacol., 79, 373 (2002).
4. C. Eccleston, B. Yang, R. Tahvonen, H., Kallio, G.H. Rimbach, A.M. Minihane, J. Nutr. Biochem., 13, 346 (2002).
5. B. Yang, H. Kallio, Trends Food Sci. Technol., 13, 160 (2002).
6. K. Heilscher, *Proceedings of the 1st Congress of the Internationala Seabuckthorn Association, Berlin*, 2003, p. 7.
7. C. Socaciu, A. Pintea, A.. Varga, F. Ranga, S. Cristurean, H.A. Diehl, Buletin USAMV-CN (A), 57, 271(2002).
8. B. Yang, H. Kallio, J. Agric. Food Chem., 49, 1939 (2001).
9. G.A. Berezhnaya, I.P. Yeliseev, V.D. Tsydendambaev, A.G. Vereshchagin, Applied Biochem. Microbiol., 24, 568 (1988).
10. G.A. Loskutova, V.G. Baykov, A.V. Starkov, F.A. Medvedev, Rastit. Resursi., 25, 97 (1989).
11. G.A. Berezhnaya, O.V. Ozerinina, I.P. Yeliseev, V.D. Tsydendambaev, A.G. Vereshchagin, Plant Physiol. Biochem., 31, 323 (1993).
12. A. Pintea, A. Marpeau, M. Faye, C. Socaciu, M. Gleizes, Phytochem. Analysis, 12, 293 (2001).
13. B. Yang, R. Carlsson, P. Oksman, H. Kallio, J. Agric. Food. Chem., 49, 5620 (2001).
14. H. Kallio, B. Yang, P. Peippo, J. Agric. Food Chem., 50, 6136 (2002).
15. L. Vlase, N. Olah, A. Marculescu, Revista de Chimie, 57, 320(2006).
16. A. Zeb, Journ. of Biol. Sciences, 4, N687 (2004).
17. S. Cenkowski, R. Yakirnishen, R. Przybylski, W.E. Muir, Canad. Biosyst. Eng., 48, 3.9(2006).
18. A. Kaminskas, V. Briedis, R. Budrionienė, V. Hendrixson, R. Petraitis, Z. Kučinskienė,Biologija, 2, 39(2006).

STUDIA UNIVERSITATIS BABES-BOLYAI, PHYSICA, LIV, 1, 2009

STRUCTURAL BEHAVIOUR OF MnBi COMPOUND

MARIA-SIMONA GUTOIU[1], EUGEN DOROLTI[1], OLIVIER ISNARD[2], VIOREL POP[1], IONEL CHICINAŞ[3]

ABSTRACT. The scientific interest regarding MnBi hard magnetic phase results from the high magnetocrystalline anisotropy of low-temperature phase (LTP) and large Kerr rotation angle of quenched high temperature phase (QHTP).

The MnBi phase was obtained by melting of elemental Mn and Bi components. The sample obtained after melting were annealed at different temperatures: 258 °C, 300 °C, 400 °C and 420 °C under vacuum (10^{-5} mbar). The X-ray patterns show a better cristallinity of the structure after annealing. In both as melt and annealed samples some quantity of free Bi phase was evidenced due to hard diffusion of the elemental components in MnBi matrix. The magnetic coercivity is reinforced by increasing the temperature and a value $\mu_0 H \approx 2.5$ T was obtained at 450 K for melted samples and subsequently milled for 2 h and annealed at 300 °C. In order to test the influence of milling on the MnBi phase stability, the as melted samples and the annealed samples were mechanically milled. The quantity of the unreacted Bi phase increases after milling.

Keywords: MnBi, hard magnetic phase, nanostructured magnetic materials

1. Introduction

An important challenge in the study of the nanostructured magnetic materials consists in the understanding and the exploitation of the peculiar physical properties when goes from the bulk to the nanomaterials. A material which can presents such interesting properties could be the intermetallic MnBi phase used as hard phase in spring magnet type nanocomposites. Although this compound has been studied since the beginning of the fifties, its study has regained interest at the end of the 1990 as it was considered an alternate solution for the permanent magnet without rare earth metals. The small number of studies reported in the literature about this compound could be explained by the difficulty in the phase formation and complex behavior of this compound: i) the existence of first order transition around 613 K from the ferromagnetic state, LTP - low temperature phase, of NiAs

[1] Faculty of Physics, Babes-Bolyai University, 400084 Cluj-Napoca, Romania
[2] Institut Néel, CNRS, University Joseph Fourier de Grenoble, BP 166X, 38042 Grenoble, Cédex 9, France
[3] Materials Sciences and Technology Dept., Technical University of Cluj-Napoca, 103-105 Muncii ave., 400641 Cluj-Napoca, Romania

type structure with magnetization oriented along c axis to a paramagnetic phase, HTP – high temperature phase, with a disorder structure of Ni_2In type phase; ii) manganese segregation at peritectic temperature of 719 K and the low diffusion of Mn in MnBi phase [1, 2]. According to the phase diagram of Mn-Bi, versus temperatures, there are three different zones: (1) in the temperature range from 719 K to Curie temperature, T_c=628 K, a mixture of paramagnetic high temperature MnBi phase (HTP) and liquid Bi, (2) from T_c to 535 K, mix of ferromagnetic low temperature MnBi phase (LTP) and liquid Bi, (3) below 535 K a composite of LTP MnBi phase and solid Bi [3]. Due to its magnetization, 600 kA/m at 300 K, and to important axial anisotropy at high temperature (~ $3 \cdot 10^6$ J/m^3 at 500 K), the MnBi compound has been considered to be of interest for the application as a permanent magnet and for magneto-optic devices [4, 5]. The maximum energetic product $(BH)_{max}$ obtained for these compounds is 61.30 kJ/m^3 (7.7 MGOe) at room temperature and 36.62 kJ/m^3 (4.6 MGOe) at 400 K, respectively, which is less than the theoretical prediction of 87.57 kJ/m^3 (11 MGOe) [6]. Regarding the orientation of magnetic moments Chen *et al*. found that it rotates from the direction parallel to the c axis at room temperature to the basal plane under 90 K [4]. Other studies [6] showed that the magnetic moments starts to rotate from the direction parallel to c axis at 200 K to a direction almost perpendicular to c axis under 50 K but the orientation of magnetization is not entire within the basal plane even at 10 K. This study concludes that within the temperature range 10 – 240 K the MnBi compound shows a conical magnetic structure.

In comparison with the great majority of magnetic materials the coercivity of the LTP increase with increasing the temperature reaching a largest value $\mu_0 H_c$ of 1.9 T at 227 ºC and having a positive coercivity coefficient [7].

For the MnBi compound, obtained by milling and subsequent annealing [7], the coercivity increase significantly for short milling time. Longer milling time would increase the coercivity with a slower rate. A longer milling time of 10 h bring the coercivity at a maximum value, which suggest that the material is close to the single domain dimension [7].

For a sample milled at various time a heat treatment will increase the coercivity due to the increase of the anisotropy energy [5, 7], showing a maximum value $\mu_0 H_c$ of 2.5 T for a heat treatment of 10 hours at 300 ºC [7]

Due to the smaller magnetisation of the MnBi phase, the maximum energy product in MnBi based magnets is low in comparison with that of the rare-earth magnets. This inconvenient could be partly overcome in “exchange spring” type composite magnets, where the low magnetisation of hard MnBi phase can be compensate by the high magnetisation of soft magnetic phases. These materials could be obtained by different techniques including mechanical milling. In this study we investigate the stability of the MnBi, LTP, obtained by arc melting and subsequent mechanical milling.

2. Experimental details

An alloy ingot with the MnBi nominal composition was prepared by arc melting under argon atmosphere. An excess of Mn was used in order to compensate the preferential evaporation of manganese during melting. The purity of the elements was 99.9 %. The obtained ingots were annealed at several temperatures: 258 °C, 300 °C, 400 °C and 420 °C, for times between 2 h to 4 days, under vacuum (10^{-5} mbar). For the annealed sample at 400 °C for 2 h, the ingot was crushed into small pieces and it was subsequently mechanically milled for two hours in a high energy planetary mill (Frisch Pulverisette 4) under helium atmosphere. The MnBi powder thus obtained was annealed at 300 °C, 350 °C and 400 °C for 30 minutes.

X-ray diffraction patterns were recorded in the angular range 2θ = 20 - 100° using a Bruker D8 Advance diffractometer with a Kα cooper radiation and a SIEMENS D500 powder diffractometer with the Kα1 radiation of cobalt.

The magnetization curves were realised by extraction method in a continuous magnetic field of up to 10 T [8].

3. Results and discussions

Comparison of the X-ray diffraction patterns of the MnBi samples obtained for as melted and annealed samples between 258 ºC and 420 ºC for 2 hours and 4 days are presented in figure 1.

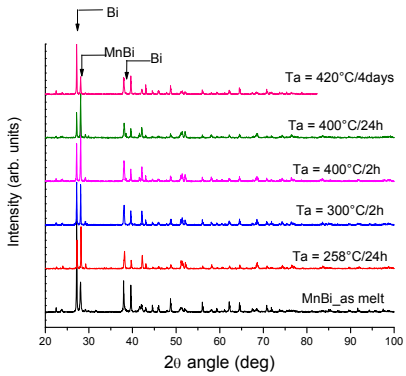

Fig 1. X-ray diffraction patterns of the MnBi sample melted and annealed between 258 ºC and 420 ºC for 2 hours and 4 days, obtained with Cu Kα radiation

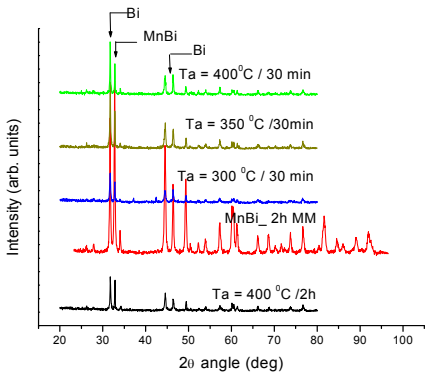

Fig 2. X-ray diffraction patterns of the MnBi samples milled for 2 h, 2h MM, and annealed between 300 ºC and 400 ºC for 30 minutes; obtained with a diffractometer with Co Kα1 radiation

The Bragg peaks corresponding to the annealed MnBi phase are better resolved in comparison with those of the as melt samples. Two phases are evidenced by X-ray diffraction before and after the annealing: a MnBi (NiAs type) phase and

the metallic Bi phase. The presence of the free unreacted starting metals in the alloys can be given by the hard diffusion of the elemental components in MnBi matrix. The best ratio between MnBi phase and unreacted Bi phase is obtained for sample annealed at 400 °C/24h, figure 1.

In order to study the influence of the milling on the MnBi phase stability, the sample annealed at 400 °C for 2 h was mechanically milled for 2 h. After milling the samples were annealed at 300, 350 and 400 °C for 30 minutes. The diffraction patterns of these samples are given in figure 2. The Bragg peaks corresponding to MnBi and Bi phases are broadened by milling. The diffraction peaks are better resolved after annealing but we still observe the presence of the both MnBi and Bi phases. The most favourable ratio for the MnBi phase was obtained for the sample annealed at 300 °C [9].

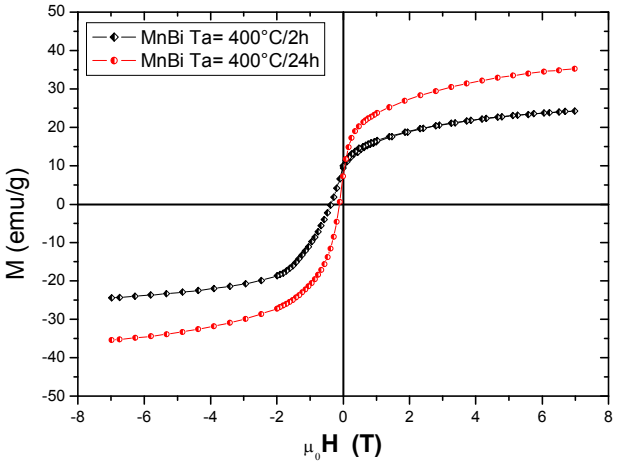

Fig. 3. Demagnetization curves for MnBi compounds melted and annealed at 400 ºC for 2h and 24 h

The magnetic behaviour was studied on both melted and milled MnBi samples. The demagnetisation curves of the melted and annealed samples are given in figure 3. The demagnetisation curves show that the highest coercivity is obtained for sample annealed at 400 °C for 2h. As shown before, the structural studies point out the presence of optimum ratio between MnBi phase and Bi metallic phase for samples annealed at 400 °C for 4 days. The larger coercivity for the sample annealed for only 2 h could be eventually explain by the microstructure peculiarity.

The magnetic hysteresis loops for the melted MnBi sample annealed at 400 °C for 2h and measured at different temperatures are presented in figure 4. A coercivity around 0.5 T and the remanence magnetisation of about 21 Am^2/kg was obtained for the sample measured at 450 K. The demagnetisation curves for MnBi mechanically milled and annealed at 300 °C for 30 min, measured for different temperatures, show an increase of the coercivity by increasing temperature. The highest coercivity field of 2.5 T was measured at 450 K, while the highest value of the remanence of around 20 Am^2/Kg was obtained for the sample measured at 300 K [9]. This behaviour can be explain by the fact that the uniaxial anisotropy decrease with decreasing temperature and became a planar anisotropy below 100 K [6].

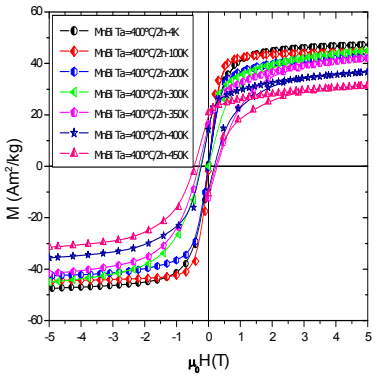

Fig. 4. Demagnetization curves and magnetic hysteresis loops for MnBi melted samples, annealed at 400 ºC for 2 h, measured at different temperatures.

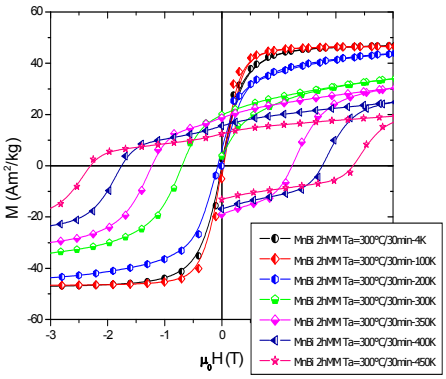

Fig. 5. Demagnetization curves and magnetic hysteresis loops for MnBi samples milled for 2 hours and annealed at 300 ºC for 30 minutes, measured at different temperature.

4. Conclusions

The MnBi phase was obtained by arc melting of elemental Mn and Bi in argon atmosphere. In both melted and annealed samples some quantity of free Bi phase was evidenced. The appropriate annealing of melted sample results in improvement of MnBi phase quantity in the alloy. The influence of milling on the MnBi phase stability of melted samples was also studied. The proportion of unreacted Bi phase increases after milling. The coercivity increases after milling and annealing. The magnetic coercivity increases by increasing temperature and the value of $\mu_0 H \approx 2.5$ T was obtained at 450 K for milled samples annealed at 300 ºC. The high coercivity evidenced in MnBi samples points out the possibility of using MnBi as hard magnetic phase in spring magnet nanocomposite. Further magnetic and crystallographic studies are in progress in order to improve the stability of the MnBi phase obtained by different methods: melting, mechanical milling, thin films, etc.

ACKNOWLEDGMENTS

This work was partly supported by the Romanian Ministry of Education and Research, grant PNCD II 72-186/2008.

REFERENCES

1 X. Guo, A. Zaluska, Z. Altounian and J. O. Ström-Olsen, J. Mater. Res. **5**, 2646 (1990).
2 C. Guillaud, J. Phys. Radium **12**, 223 (1951).

3 Yongsheng Liu, Jincang Zhang, Shixun Cao, Xiaoyoung Zhang, Guangqiang Jia, Zhongming Ren, Xi Li, Chao Jing, Kang deng. Phys. Review B 72, 214410 (2005).
4 D. Chen and R. L. Aagard, J. Appl. Phys. **41**, 2530 (1970).
5 T. Chen and W. E. Stutius, IEEE Trans. Magn. **10**, 581 (1974).
6 J. B. Yang, W. B. Yelon, W. J. James, Q. Cai, M. Kornecki, S. Roy, N. Ali, and Ph l'Heritier, J. Phys. Condens. Matter. **14**, 6509 (2002).
7 S. Saha *et al.* J. Appl. Phys. **91**, 8525, (2002).
8 A. Barlet, J. C. Genna, P. Lethuillier, Cryogenics **31** (1991) 801.
9 S. Gutoiu, Master thesis, Babes-Bolyai University Cluj-Napoca, Romania.

STUDIA UNIVERSITATIS BABES-BOLYAI, PHYSICA, LIV, 1, 2009

FINITE DIFFERENCE TIME DOMAIN (FDTD) CALCULATIONS OF SURFACE PLASMON RESONANCE OF DIFFERENT SIZE AND SHAPE METALLIC NANOPARTICLES

FRANÇOIS K. GUEDJE[1,*], SANDA BOCA[1], MONICA POTARA[1], ARINA MODREA[2], SIMION ASTILEAN[1]

ABSTRACT. In this work we employ the Finite Difference Time Domain (FDTD) method to calculate the optical spectra and the intensity of local electromagnetic field at the surface of different size, shape and assembling configuration of nanoparticles (NPs) with a view to optimize their sensing activity. We first consider gold nanospheres of 20 nm diameter where analytical solutions are available for comparison. The other shapes we consider include gold nanorods and silver nanoprisms which are particularly important for applications, because they allow tuning the plasmon resonances across the whole visible and near infrared range. The theoretical spectra are compared with experimental data from synthesized samples in our laboratory.

Keywords: nanoparticle, plasmonics, FDTD.

1. Introduction

In recent years, plasmonics has attracted a great deal of attention due to its important potential toward applications in sensing, medical imaging and information processing [1]. This branch of photonics develops new concepts to confine light beyond the diffraction limit and enhance the electromagnetic field at the nanoscale. The past decade has seen significant advances in the synthesis and fabrication of disperse noble metal nanoparticles with a variety of shapes, from spheres to branched multipods. These particles are studied for a large variety of applications due to their localized surface plasmon resonance (LSPR). LSPR occurs when the electromagnetic field of light drives the collective oscillations of a nanoparticle's free electrons into resonance.

[*] On leave from the International Chair in Mathematical Physics and Applications, Université d'Abomey-Calavi, 01 BP 526 Cotonou, Bénin

[1] Babes-Bolyai University, Faculty of Physics and Institute for Interdisciplinary Experimental Research, Nanobiophotonics Center, Treboniu Laurian Street 42, 400271 Cluj-Napoca, Romania

[2] Petru Maior University, Faculty of Engineering, Tirgu-Mures, Romania

The LSPR enables many relevant applications including biological and chemical sensing [2-3], biological imaging labels [4], and nanoscale optical waveguides [5]. In particular, LSPR in the near-infrared (NIR) enables a significant step toward diagnostic and therapeutic in cancer research and other biomedical applications [6].

Here we employ the FDTD method to evaluate the plasmonic resonances and the intensity of local electromagnetic field at the surface of different size, shape and assembling configuration of GNPs in view of optimizing their sensor sensitivity. We first consider gold nanospheres, and we compare the results with available analytical solutions. Then we consider the nanorods with variable aspect ratio. For other particles of sufficiently anisotropy, like the case of nanoprism, it can give rise to additional peaks in the absorption spectrum as a result of multipolar plasmon excitation. In most of the works dedicated to investigating metallic nanostructures the background is usually air. In this work, we study the optical properties of the nanostructure within a natural surrounding medium different from air. This allowed to explain and better understand the effect of layers of cetyltrimethyl ammonium bromide (CTAB) surfactant and methoxy polyethylene glycol-thiol (mPEG-SH) in case of gold nanorods and chitosan polymers in case of silver nanoparticles.

2. Numerical Methodology

Mie [7] was the first who solved exactly and completely the problem of plane electromagnetic wave scattering by a homogeneous dielectric sphere. To properly treat the interaction of nanoparticles with optical fields, a full electromagnetic solution to the Maxwell's equation is needed. For more complex geometries, one has to rely on numerical simulations. Several methods for numerically solving electromagnetism for arbitrary geometry exist. Of all, the finite difference time domain (FDTD) technique of Taflove [9] and Sullivan [10] has proved to be a powerful tool to calculate the spectra as well as the near field properties of metal colloids.

This method solves the time-dependent Maxwell's equations by discretizing space and time and involves a relativity simple time-stepping algorithm. The electric flux dependent form of Maxwell's equations is given by:

$$\frac{\partial \vec{D}}{\partial t} = \nabla \times \vec{H} \tag{1}$$

$$D(\omega) = \varepsilon(\omega) E(\omega) \tag{2}$$

$$\frac{\partial \vec{H}}{\partial t} = -\frac{1}{\mu_0} \nabla \times \vec{E} \tag{3}$$

Where $\vec{H}$, $\vec{E}$, and $\vec{D}$ are the magnetic, electric, and displacement field, respectively. μ_0 is the permeability of free space and $\varepsilon(\omega)$ the complex dielectric constant.

The technique consists of solving these equations on a discrete grid, replacing all derivatives with finite differences. Following the Yee algorithm [11], both $\vec{D}$ and $\vec{H}$ are offset in both space and time. This allows one to use central differences, making the algorithm second-order accurate. In one dimension, Equation (1) can be written as:

$$\frac{D^{n+½}(k)-D^{n-½}(k)}{\Delta t}=\frac{H^{n}(k+½)-H^{n}(k-½)}{\Delta x} \tag{4}$$

Where k is the spatial coordinate and the superscript n denotes time. It is then straightforward to solve for $D^{n+½}(k)$ in terms of $D^{n-½}(k)$, $H^{n}(k+½)$ and $H^{n}(k-½)$ which are already stored in memory. Two points must be taken into account. First, the grid Δu must be fine enough to describe the smallest spatial features, whether it is the particle geometry or particle separation, where u is the side of a cubical cell. The time step Δt must be chosen with even greater consideration. The FDTD algorithm is stable only if the condition $\Delta t \le \frac{\Delta u}{c\sqrt{3}}$ is verified. The simulation is generally computationally intensive when high spatial precision is required.

Typically, FDTD calculations have been carried out for dielectric materials. Recent advances have extended the use of FDTD to the treatment of the materials with frequency dependent, complex dielectric constants [12]. It is the category of real metals.

If the metal is assumed to follow the Drude model, one can write the permittivity ε as

$$\varepsilon(\omega)=\varepsilon_{\infty}-\frac{\omega_p^2}{\omega^2+i\nu_c\omega} \tag{5}$$

Where ω is the angular frequency, ω_p is the plasma frequency, ν_c is the collision frequency and ε_{∞} the high frequency dielectric constant. The Drude model is appealing in that it is derived from the simplest physical picture of free electron gas. The response of near-field probe has been simulated [13] under Drude model using FDTD. However, the Drude model does not accurately describe the real and imaginary indices of refraction of noble metals over a wide frequency range. Also, the Fourier transform of the susceptibility is often not numerically stable.

3. Computation of optical spectra and field enhancements for nanoparticles of different shapes

Figure 1 shows the nanostructures we study using the code from Lumerical™ [14] and compare their theoretical spectra with experimental data from synthesized samples in our laboratory. All our results refer to absorption spectra

and field enhancement of gold nanosphere (diameter 20nm), gold nanorod (diameter 24nm, length 53nm), and regular silver nanoprisms (edge length of 100nm with variable thickness) in water solution.

Figure 1. Example of nanoparticles shapes (sphere, rod, and prism) we study in this work.

3.1 Gold nanosphere

In a first step, we calculate here the absorption for gold nanosphere by using FDTD method and compare our result with that given from the Mie theory [7, 15]. Figure 2a shows for comparison, the experimental data obtained in our laboratory, our result and Mie Theory, for gold nanosphere of diameter 27 nm in water. Figure 2b present the field enhancement at the Plasmon resonance (523.6nm). It shows the amplitude of the local charge density oscillation for the sphere. From the symmetries of the distribution, the resonance peak can be labeled as the dipole resonance.

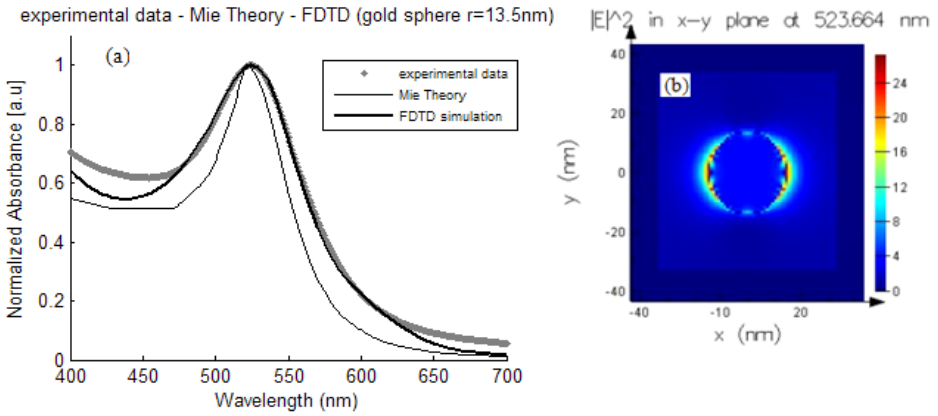

Figure 2. (a) The absorption spectra of a gold sphere with r =13.5nm radius calculated by FDTD and Mie theory. The experimental absorption spectrum is shown with dots for comparison. (b) The field enhancement ($|E^2|$) at the surface of nanoparticles calculated by FDTD. The field polarization is along x axis. The grid is 0.5 nm.

For gold dimers or particle chains, the spectra change drastically with the interparticle distance. We present in Figure 3 the results of the FDTD calculations. For the interparticle distance $d > D$, D being the sphere diameter, the electromagnetic

coupling is very weak and the spectrum calculated for such a dimer coincides with that of an isolated particle. It can be seen from Figure 3a that the transverse and longitudinal local surface resonances appear at shorter and longer wavelengths for $d << D$ when the electromagnetic coupling between particles is strong. When the spheres are in contact, the resonance splits into two distinct peaks. The first is the transversal resonance and the second is the longitudinal resonance for the dimer illuminated with incident plane wave. The longitudinal LSPR at 632 nm is not due to dipolar (521nm) but due to higher-polar collective oscillation of conduction electrons. Figures 3b show that the electromagnetic field at the junction excited by the light polarized along x-axis is larger than that excited by light polarized along y-axis. One can conclude that the SERS enhancement by longitudinal LSPs is due to the presence of enhanced electromagnetic field at an interparticle junction on the long axis of the dimer of gold nanospheres.

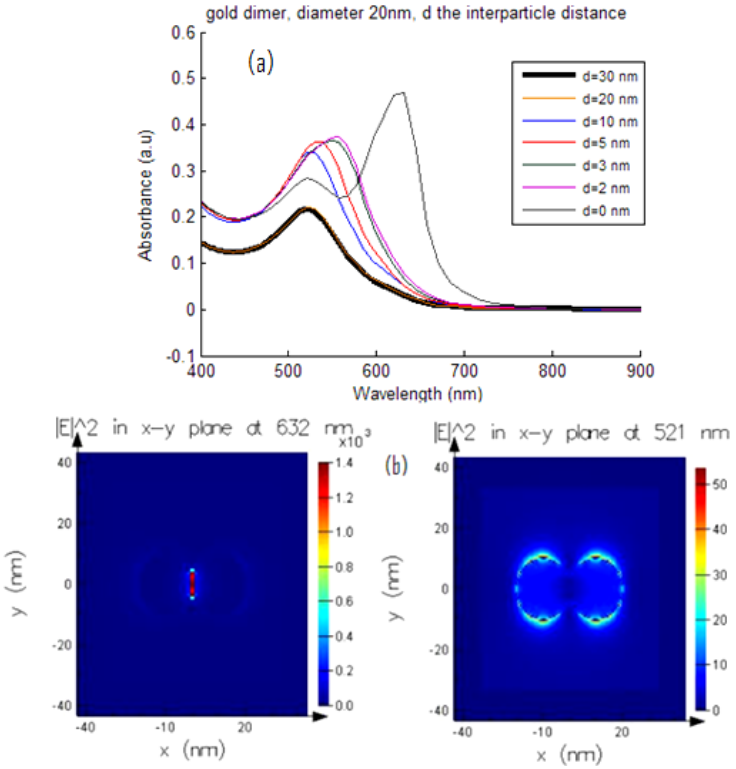

Figure 3. (a) FDTD calculated spectra of two spheres (diameter 20nm), where d is the distance between the spheres. As the particles are brought together until they are touching (d=0), the plasmon resonance peak shifts red. (b) Electric field near the dimer calculated by the FDTD model at the resonances 632 and 521nm for the particle close together. Note the incident light is propagating along the z-axis and is polarized along the x-axis (left) and along y-axis (right).

3.2 Gold nanorod

For our calculations, the nanorod is modeled as a cylinder which ends are capped by half spheres, the aspect ratio is defined as the ratio between its length and diameter. The layer of 5nm of CTAB is wrapped around a longitudinal face of the gold nanorod while the mPEG polymer sticks at both ends of the rod. First we study the nanorod of 55nm length and 24nm diameter. For CTAB we consider a value of 1.41 for its refractive index and 1.42 for mPEG. The presence of these polymers on the surface of gold nanorods plays on their optical properties. As the aspect ratio increases, the intensity of the absorption coefficient increases due to the larger degree of anisotropy of the particle. The results show a linear increase in the maximum of the longitudinal Plasmon resonance intensity and wavelength as the aspect ratio is increased in Figure 4. The transverse Plasmon is not presented here, as it is insensitive to the aspect ratio with fixed diameter.

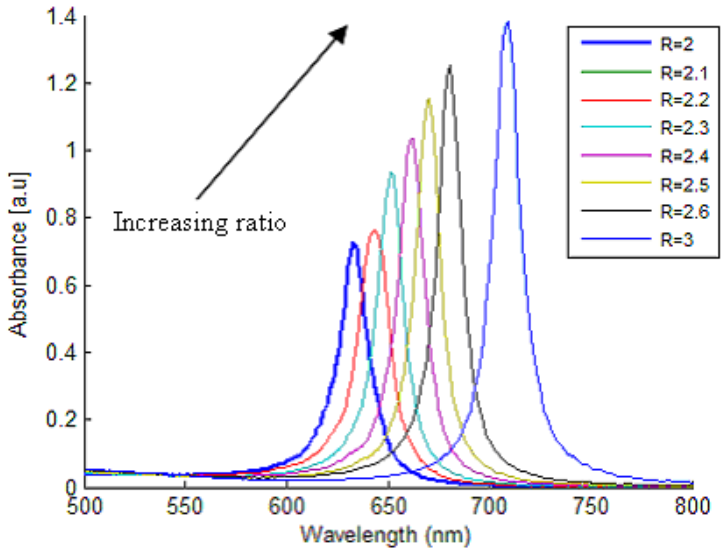

Figure 4. Longitudinal plasmon resonance absorption of single gold nanorod with diameter 24nm, coated with 5nm thickness of CTAB, calculated for different aspect ratios using FDTD simulations with 1.5nm grid resolution and incident light polarization along the major axis of the nanorod.

Figure 5 represents the near field on the rod excited with a field propagated along z-axis and polarized along the long x-axis of the rod at 646nm. One can see a collective oscillation of the charges along the long axis of the rod. This great field enhancement is important in the development of diagnostics tools. Nanorods are observed to have higher SERS signals than spheres, due to the higher electric field generated at the tips of the nanorod.

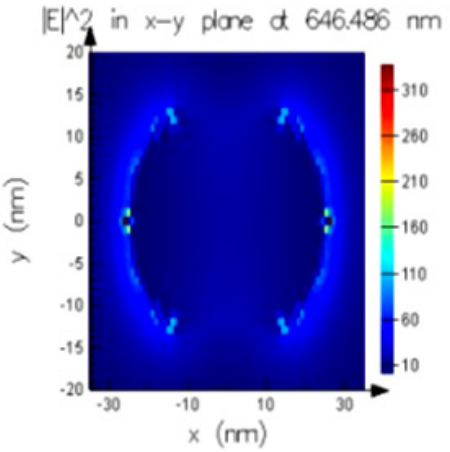

Figure 5. Electric field enhancement near the rod coated in CTAB, The incident light is propagating along the z-axis and is polarized along the x-axis.

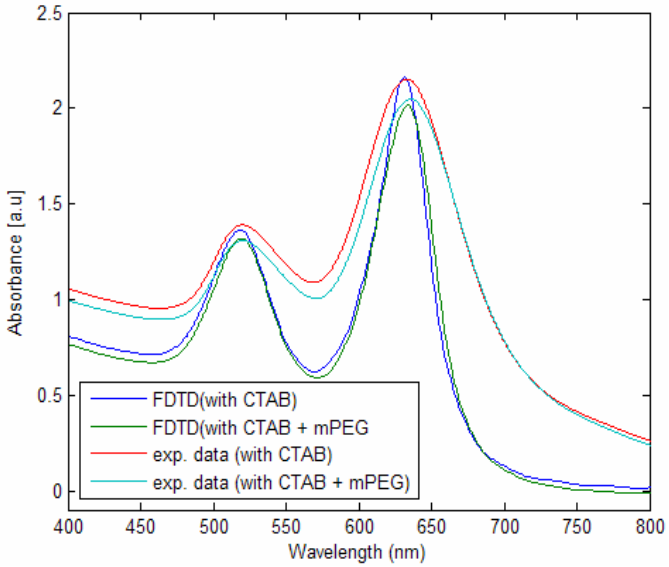

Figure 6. Absorption spectra of gold nanorods with 2.2 aspect ratio (L=53 nm, D=24 nm). From the top, the first and the second (red and turquoise) curves represent the experimental spectra of gold nanorods embedded in CTAB, and of nanorods conjugated with mPEG-SH respectively. The third and the fourth (blue and green) spectra are the FDTD corresponding simulations. We model the CTAB as 5 nm layer with n=1.41 refractive index around the longitudinal face of the rod. The mPEG is modeled by a 2 nm thickness half spherical outer layer, having n=1.42 refractive index around the half sphere situated at the end of the rod. λ_{T1}= 519.6 nm and λ_{T2}= 520.8 nm λ_{L1}= 632.6 nm and λ_{L2}= 635.4 nm

Figure 6 represents the results of our calculations compared with the experimental data. The calculations are done for a single nanorod with 2.2 aspect ratio. This result proves that the maximum contribution is referred to this ratio and that the mPEG has a slight effect on the position of the plasmon resonances. Moreover, the methoxy (polyethylene glycol)-thiol (mPEG) can be used to overcome the cytotoxicity caused by the presence of residual cetyltrimethyl ammonium bromide (CTAB), a surfactant required for nanorod synthesis and stabilization.

3.3 Silver nanoprism

In this section, we calculate with FDTD the optical properties of regular triangular silver prisms in water. We consider a diverse set of prisms to cover the range of possible excitations for this structure. It was noted that the full orientation could be approximated using three orientations [16], but orientations where the polarization vector E is parallel to the triangular cross section are most important to the overall extinction, while orientations where the polarization vector is perpendicular to the plane contribute much less.

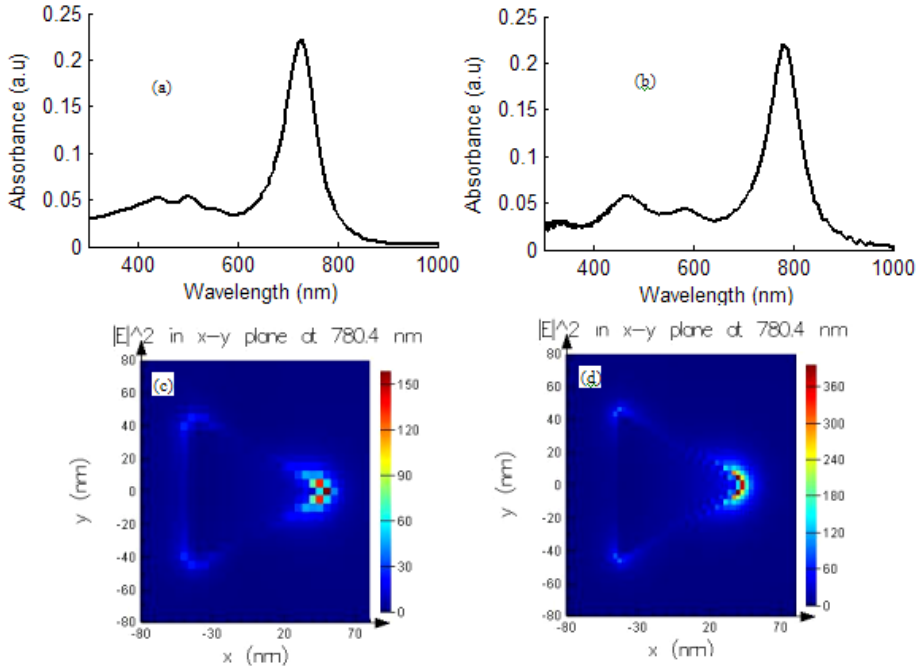

Figure 7. Absorption spectra of a triangular silver nanoprism in water solution.(a) edge length of 100nm and thickness of 20nm, (b) edge length of 100nm and thickness of 15nm, (c) corresponding electric field enhancement at 781.4nm, (d) corresponding electric field enhancement at 781.4 nm. In every case the incident light is propagating along the z-axis and is polarized along the x direction.

We see in these figures 7a and 7b that for each particle there are three dominant peaks in the absorbance spectrum, corresponding to different modes of plasmon excitation. In Figure 7a, we have abroad resonance with two maxima at 441.2 and 503.8nm attributed to quadrupole excitation, and a peak at 727.2nm corresponding to in-plane dipolar excitation. In Figure7b we find that the most intense peak 781.4nm corresponds to in-plane dipolar excitation. Also, the middle resonance 467.2nm is associated with in-plane quadrupole excitation and the bluest resonance which is at 334.4nm refers to out-of-plane quadrupole excitation. The positions of plasmon resonances depend, among other parameters, on particle size, or more specifically on the ratio between lateral dimensions and thickness (aspect ratio). Calculations indicate that the extinction spectrum of the nanoprisms is also sensitive to the thickness of the particles. For increasing the prism aspect ratio for fixed edge length, we note a red shift of the resonance corresponding to the dipole mode from 727.2 to 781.4nm. Figures 7c and 7d show the field enhancement for the two cases of nanoprisms we consider here, plotted as contours of $|E^2|$. One can see that the intensity of the near field is sensible to the prism aspect ratio. The anisotropic nanoparticles produce much stronger electric fields than that of the simpless structures as nanospheres, particularly for nanoparticles with sharp points such as triangular nanoprisms and branched nanocrystals.

4. Conclusion

In this work we calculate the optical properties of gold and silver nanoparticles of different shape and size. First we studied the gold sphere properties and the calculations are compared with the analytical existing results. The computed spectra agree very well with experimental results. The simulations showed a local electric field enhancement around the nanostructures, and in particular the nanoparticles assemblies show the largest field enhancement, confirming their utility in surface-enhancement Raman spectroscopy. We finish by theoretical calculations of the optical spectra of regular triangular silver prism and discuss their properties as function of edge length. The ability to provide large electric field enhancements make the triangular nanoprisms and branched nanostructures very attractive for applications in SERS.

Acknowledgments

The first author gratefully acknowledges the financial support from AUF (Agence Universitaire de la Francophone) project No CE/MC/466/08. Other authors gratefully acknowledge the financial support from CNCSIS project IDEI 477 /2007.

REFERENCES

1. Albert Polman, *Plasmonics Applied,* Science, 322, 2008, 868-869.
2. Andrea Alu and Nader Engheta, *Cloaking a sensor*, Phys Rev Lett. 102, 2009, 233901.
3. R. Elghanian., J.J. Storhoff, R.C. Mucic, R.L. Letsinger, C.A. Mirkin, *Selective Colorimetric Detection of Polynucleotides Based on the Distance-Dependent Optical Properties of Gold Nanoparticles ,* Science, 277, 5329, 1997, 1078-1081.
4. S. Schultz, D.R. Smith, J.J. Mock, D.A. Schultz, *Single-target molecule detection with nonbleaching multicolor optical immunolabels,* Proc. Natl. Acad. Sci. U.S.A, 97, 3, 2000, 996-1001.
5. S.A. Maier, P.G. Kik, H.A. Atwater, S. Meltzer, E. Harel, B.E. Koel, A.A.G. Requicha, *Local Detection of Electromagnetic Energy Transport Below The Diffraction Limit in Metal Nanoparticle Plasmon Waveguides,* Nat. Mater, 2, 4, 2003, 229-232.
6. M. Baia, S. Astilean, T. Iliescu, *Raman and SERS investigations of pharmaceuticals*, Ed. Springer,2009.
7. G. Mie, Ann. Phys., 4, 25, 1908, 377.
8. J.P. Kottmann, O.J.F. Martin, D.R. Smith, S. Schultz**,** *Plasmon resonances of silver nanowires with a non-regular cross-section*, Phys. Rev. B, Vol. 64, Issue 23, 2001, pp.235402.1-10.
9. A. Taflove, S.C. Hagness, *Computational Electrodynamics: The finite-difference time domain method,* Artech. House, Inc., Norwood, MA, 2000.
10. D.M. Sullivan, *Electromagnetic Simulation Using the FDTD Method,* IEEE Press: Piscataway, NJ, 2000.
11. K.S. Yee, *Numerical solution of initial boundary value problems involving Maxwell's equations in isotropic media*, IEEE Trans. Antennas Propag., 14, 1966, 302-307.
12. R.J. Luebbers, F. Hunsberger, and K.S. Kunz, *A Frequency Dependent Time Domain Formulation for Transient Propagation in Plasma*, IEEE Trans. Antennas Propag, 39, 1991, 29-34.
13. R.X. Bian, R.C. Dunn, X.S. Xie and P.T. *Leung, Single molecule emission characteristics in near-field Microscopy,* Phys. Rev. Lett., 75, 1995, 4772-4775.
14. Lumerical (ID:4D3AB99E).
15. C.F. Bohren and D.R. Huffman, *Absorption and Scattering of Light by Small Particles,* Wiley, New York, 1983.
16. R. Jin, Y. Cao, C.A. Mirkin, K.L. Kelly, G.C. Schatz, and J.G. Zheng, *Photoinduced Conversion of Silver Nanospheres to Nanoprisms,* Science 294, 5548, 2001, 1901-1903.

STUDIA UNIVERSITATIS BABES-BOLYAI, PHYSICA, LIV, 1, 2009

MASS SPECTRAL STUDY OF MOLECULAR CLEAVAGE PATHWAYS IN SOME ESTERS OF AMIDOTHIOPHOSPHONIC ACIDS

IOAN FENESAN[1], SIMONA NICOARA[2,3], MONICA CULEA[4], ANDREI HANTZ[1], ALEXANDRU ALEXANDRI[4]

ABSTRACT. The paper presents the general synthesis procedure and mass spectral analysis of some oxyminic esters of the cyclohexyl- and phenyl- thiophosphonic acids, respectively. The compounds are expected to have biologic potential owing to their elemental composition and chemical structure, confirmed via IR, ^{1}H-NMR and mass spectrometry analyses. EI mass spectra at 70 eV, high resolution mass measurements and metastable ions cleavage were used to elucidate the possible fragmentation processes.

Keywords: oxyminic amidothiophosphonic esters, electron impact ionization, mass spectrometry, molecular cleavage pathways

INTRODUCTION

Cyanoxyminic phosphorilic and thiophosphorilic esters have biologic activity, mainly showing insecticidal properties [1-7]. The compounds studied here: 2-cyano-2-(dimethyl-amino-cyclohexyl-thiophosphono-oximino)- acetamide (**1**), 2-cyano-2-(morfolinyl-cyclohexyl-thioposphono-oximino) acetamide (**2**), 2-cyano-2-morfolinyl-cyclohexyl-thiophosphono-oximino)- ethylacetate (**3**), and 2-cyano-2-(diethylamino-phenyl-thiophosphono-oximino)-acetamide (**4**), having the molecular structure shown in Table 1 and figure 1(a), were synthesized at the Chemistry Institute „Raluca Ripan", Cluj-Napoca, according to reactions summarised in figure 1 (b).

Biology studies on compounds **1-4** showed that, owing to their molecular structure and composition, they develop a certain insecticidal activity (against *Tribolium confusum,* a flour and grain parasite insect, compounds **3** and **4)**, and a good fungicidal activity (against *Botrytis cinerea,* a grapes fungus, compounds **2** and **3)** [8].

[1] Chemistry Institute "Raluca Ripan", Al. Vlahuta str., Cluj-Napoca, Romania
[2] Physics Department, Technical University, 15 C. Daicoviciu str., Cluj-Napoca Romania, snicoara@phys.utcluj.ro
[3] Planetary and Space Scinces Research Institute, The Open University, Walton Hall, Milton Keynes, MK7 6AA, UK, s.c.nicoara@open.ac.uk
[4] Faculty of Physics, "Babes-Bolyai" University, 1 M. Kogalniceanu str., Cluj-Napoca, Romania

Table 1.

Chemical composition of the cyanacetamide oxyminic and cyanacetilacetate oxyminic esters of the cyclohexyl- and phenyl- thiophosphonic acids **1-4**.

Compound (**M,** amu)	**1** (302)	**2** (344)	**3** (373)	**4** (324)
R (mass, amu)	C_6H_{11} (83)	C_6H_{11} (83)	C_6H_{11} (83)	C_6H_5 (77)
R'$_2$ N (mass, amu)	$(CH_3)_2N$ (44)	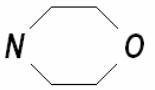 (86)	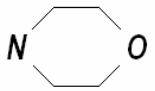 (86)	$(C_2H_5)_2N$ (72)
X (mass, amu)	NH_2 (16)	NH_2 (16)	OC_2H_5 (45)	NH_2 (16)

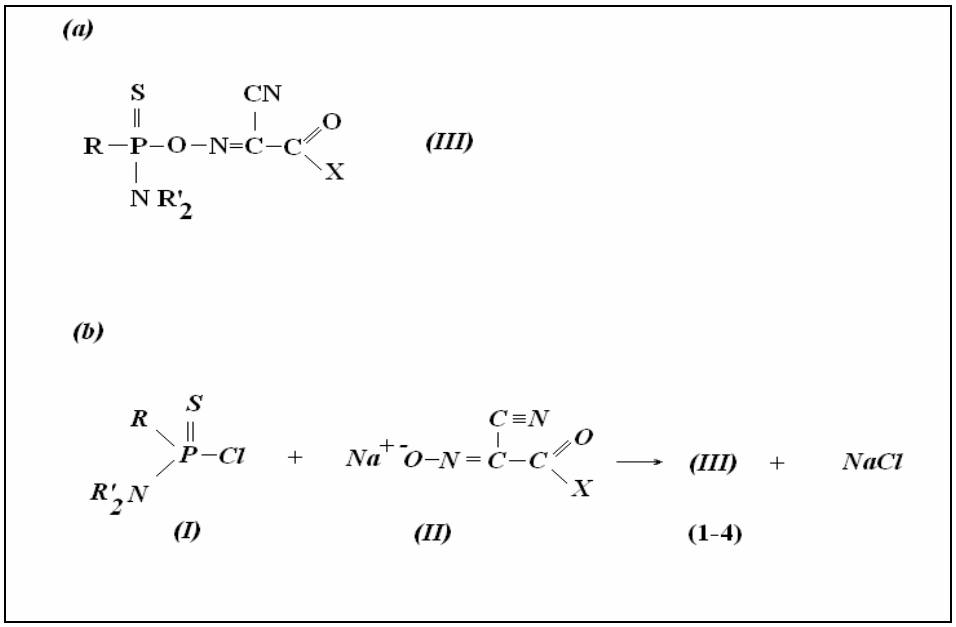

Figure 1. (a) Formula and structure of compounds **1-4**; (b) General equation of the synthesis reaction for compounds **1-4**, structure **III**.

EXPERIMENTAL

General procedure of synthesis for compounds 1-4

Potassium salt of the oximinic derivatives (0,011 moles) and amidothiophosphonic chloride (0,010 moles) in 5 ml of dimethylformamide were stirred for 2 h at 50 ^oC. The mixture was cooled (20 ^oC) and suspended in a saturated

solution of $NaHCO_3$ (100 ml). The precipitate was then solved in ethylic ether and dried ($MgSO_4$). After filtration and solvent removal, with recrystallization from ethylic ether:petroleum ether 1:1, the white compounds **1-4** were obtained (yield 90 %).

MS measurements

All mass spectra were recorded on an electron impact double focusing mass spectrometer MAT-311, set at 70 eV electron energy, 100 μA electron emission current and 150 ^oC ion source temperature. The direct inlet system was maintained at the optimum evaporation temperatures for each compound, in the range 170-200 ^oC. Fragmentation channels were elucidated based on metastable ions transitions in MIKE scanning, and HR mass measurements in the peak matching mode, using PFK ions as reference masses.

RESULTS AND DISCUSSION

Synthesis

Compounds **1-4** were obtained by the nucleophilic substitution reaction (Figure 1. b) of chlorine from the corresponding thiophosphorilic chloride (***I)*** by the sodium salt (***II)*** of 2-cyano-2-hydroximino-acetamide (X= NH_2), or of 2-cyano-2-hydroximino-ethylacetate (X= OC_2H_5), in dimethylformamide as a solvent. IR spectra and ^{1}H-NMR results are consistent with the chemical structures of the compounds synthesized:

Compound **1**: mp: 139-140 ^oC; IR (KBr) cm^{-1} 2235 (C≡N), 630 (P=S); 1615 (C=N); 1730 (C=O amidic); 3450 (NH_2 amidic assym.); 3235 (NH_2 amidic symm.); ^{1}HNMR (D_2O 10 %, 60 MHz) δ_{ppm}: 1-2 (cC_6H_{11}, m), 2.84 [$N(CH_3)_2$, d], $J_{P\text{-}N\text{-}CH3}$ 11,22 Hz, 2.87 (NH_2 amidic, s).

Compound **2**: m.p. (^oC): 146-148; IR (KBr) cm^{-1} 2230 (C≡N), 630 (P=S), 1615 (C=N), 1725 (C=O amidic), 3395 (NH_2 amidic assym.), 3225 (NH_2 amidic symm.); ^{1}HNMR (D_2O 10 %, 60 MHz) δ_{ppm}: 1-2 (cC_6H_{11}, m), 5.56 [$P\text{-}N(CH_2)_4O$, m], 2.9 (NH_2 amidic, s)

Compound **3**: m.p. (^oC): 83-84; IR (KBr) cm^{-1} 2225 (C≡N), 630 (P=S), 1570 (C=N); 1770 (C=O esteric); ^{1}HNMR (D_2O 10 %, 60 MHz) δ_{ppm}:1-2 (cC_6H_{11}, m), 5.56 [$P\text{-}N(CH_2)_2O$, m].

Compound **4**: m.p. (^oC): 157-158; IR (KBr) cm^{-1} 2230 (C≡N), 630 (P=S), 1615 (C=N), 1725 (C=O amidic), 3390 (NH_2 amidic assym.), 3228 (NH_2 amidic symm.); ^{1}HNMR (D_2O 10 %, 60 MHz) δ ppm: 5-5.5 (C_6H_5, m), 1.07 [$P\text{-}N(CH_2\text{-}CH_3)_2$, t]. $J_{H\text{-}H}$ 6.08 Hz, 3.24 [$P\text{-}N(CH_2\text{-}CH_3)_2$, m], 3.03 ($NH_2$ amidic, s).

Mass spectral data

Figures 2 (a) and (b) show the 70 eV mass spectra of compouns **1** and **4**, respectively. Figure 3 presents the cleavage pathways proposed for the cyclohexyl-thiophosphonamido derivatives **1-3.** In the low abundance (2 %) molecular ions $\mathbf{M_{1\text{-}3}^{+\cdot}}$**,** the simple fission of the P-N bond, is likely to produce the abundant ion *a*,

m/z ($^{+}NR_2'$), that gives the base peak in (**1**) and (**3**),and an intense ion (60 %) in (**2**). Its composition $^{+}N(CH_2)_4O$, at m/z 86 (**2, 3**), with the positive charge at the N atom, was reported for other phosphorylic-amido derivatives [9-11].

The abundant ion *b*, m/z 44 of 80 % in compound **1**, giving also the base peak in compound (**2**), may result from the cyanacetamidoximinic group, stabilized by the resonance: NH_2-C+=O⇔$[NH_2=C=O]^+$ [10].

In all three spectra, the relatively abundant (18-20 %) ion *c*, m/z (NR'_2+H) is probably formed by the fragmentation involving the H transfer from the cyclohexil group to N, through a 5 member transition state, as found in molecules with similar moieties [11,12].

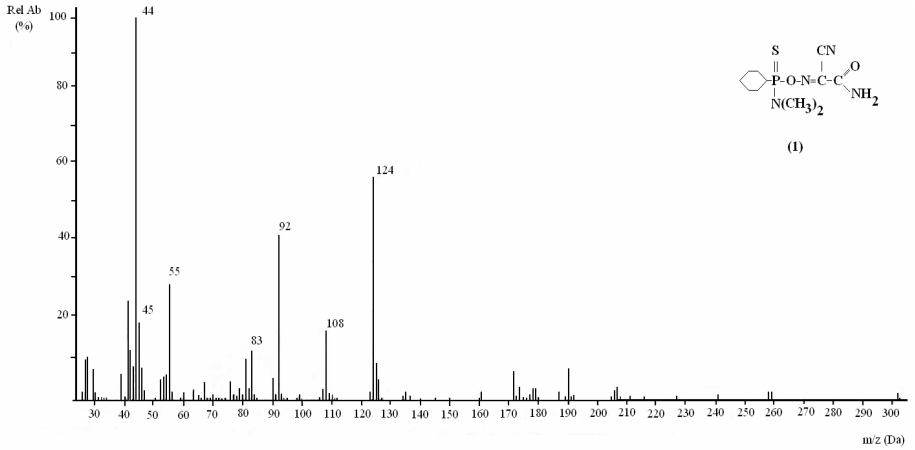

Figure 2. (a) 70 eV mass spectrum of 2-cyano-2-(dimethyl-aminocyclohexyl-thiophosphono-oximino)-acetamide (**1**)

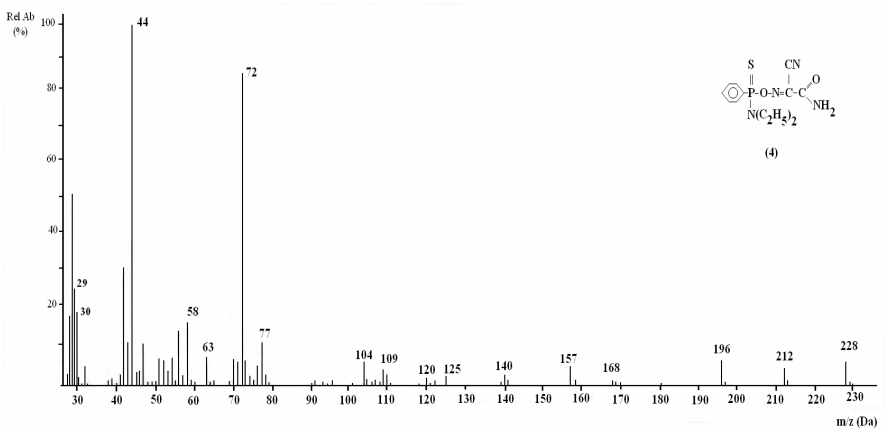

Figure 2. (b) 70 eV mass spectrum of the 2-cyano-2-(diethylamino-phenyl-thiophosphono-oximino) acetamide (**4**)

In compounds **2** and **3**, the ion *a* undergoes a ring contraction to the structure *a'*$_{2,3}$, m/z 56 (20-26 %), by eliminating the neutral molecule CH_2O. The process was detected as metastable ions transition and was also found in similar molecules [11].

The simple fission of the P-C bond in $\mathbf{M}^{+\cdot}$ in compounds **1-3**, leads to the relatively abundant (20-25 %) cyclohexil ion *d*, m/z 83 (20-25 %). MIKE spectra confirmed further cleavage to typical fragment ions *e*, m/z 55, and *f*, m/z 41 [11,12]. The low abundance (5 %) ion *g*, m/z 259 is probably formed from the molecular ion $\mathbf{M_1}^{+\cdot}$ in compound **1**, via a H atom rearrangement from the dimethylamido moiety to the S atom, and the subsequent elimination of a neutral radical NC_2H_5 [13]. A relatively abundant (12%) ion *h*, m/z (146+NR'$_2$) is likely to

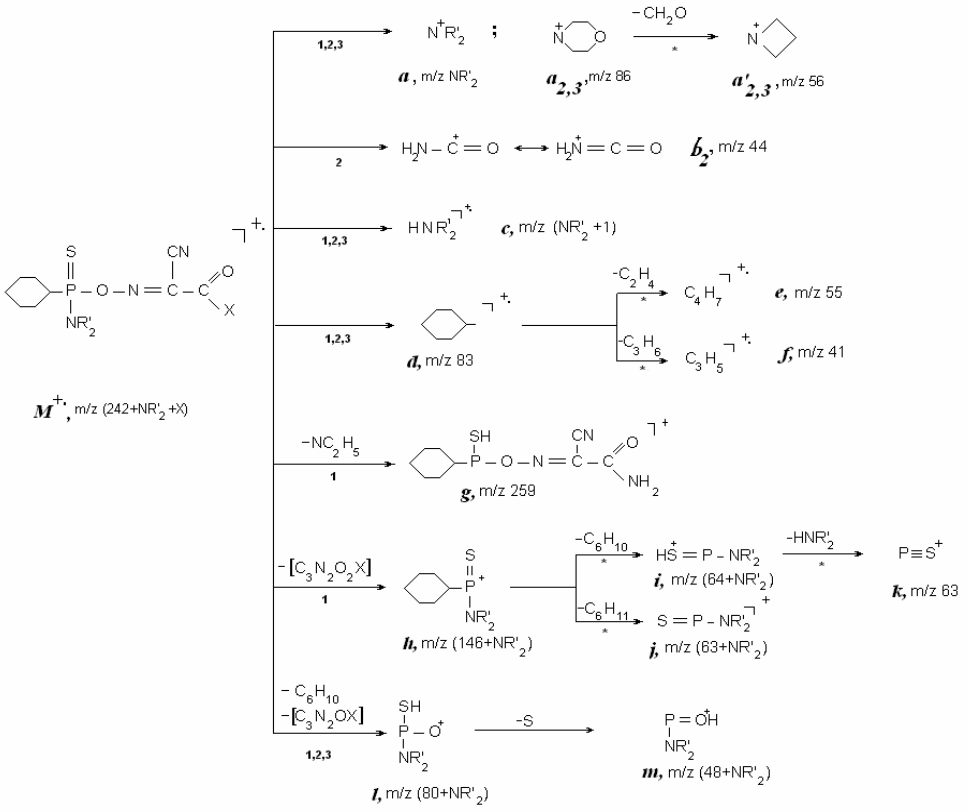

Figure 3. Unimolecular cleavage pathways proposed in compounds **1-3.** Metastable ion transitions detected in MIKE scaning in compound **(1).**

result from the molecular ion $\mathbf{M_1}^{+\cdot}$**,** by the simple fission of the P-O bond. MIKE spectra supported its further cleavage to the ion structure *i*, m/z (64+NR'$_2$) by the loss of the neutral group C_6H_{10}, subsequently loosing the neutral molecule HNR'$_2$, to result in the fragment ion *k*, m/z 83. Along another fragmentation process, the ion *h* eliminates a neutral radical C_6H_{11} and results the ion *j,* m/z (63+NR'$_2$), process recorded as metastable ion cleavage in compound **1**.

The molecular ion $\mathbf{M_1}^{+\cdot}$ may generate the abundant (60 %) ion *l*, m/z (80+NR'$_2$), via a more complex process, involving *(i)* the rearrangement of a H atom from the cyclohexyl to the S atom, with the elimination of the neutral radical C_6H_{10}, and *(ii)* the fission of the O-N bond, with the loss of the neutral group N=C(CN)C(X)=O. The ion *l* may further lose the S atom, to form the abundant (45 %) ion *m*, m/z (48+NR'$_2$).

Figure 4 shows the fragmentation pathways proposed for the phenyldiethylamidothiophosphonic acid (**4**). The mass spectrum (fig. 2.b) shows a barely visible molecular ion $\mathbf{M_4}^{+\cdot}$ (1 %) that is likely to undergo the cleavage of the P-N bond to result in the abundant ion a_4, m/z 72 HR mass measurements confirmed its elemental composition $^{+}N(C_2H_5)_2$, and that of the protonated ion $HN^{+}(C_2H_5)_2$ at m/z 73, with a relatively low abundance (5 %).

The base peak at m/z 44 is possibly generated by two processes: *(i)* the elimination of a neutral ethene molecule C_2H_4 from the diethylamidic group in a_4, resulting in ion b_4 i figure 4, with the elemental composition $[NC_2H_6]^{+}$, a process described in similar molecules [10], and *(ii)* by the simple fission of the C-C bond in $\mathbf{M_4}^{+\cdot}$**,** leading to the ion c_4, from the cyanacetamidic group, stabilized by the resonance $H_2N\text{-}C^{+}\text{=}O \leftarrow \rightarrow H_2N^{+}\text{=}C\text{=}O$ [10].

The fission of the P-O bond in $\mathbf{M_4}^{+\cdot}$ produces the ion d_4, m/z 212 (140+NR'$_2$) (5 %). This may eliminate the neutral group NC_4H_9, to form the ion e_4, m/z 141. The latter subsequently loses the neutral atom S, resulting the fragment ion f_4, m/z 109. The ion d_4 may lose the neutral radical $N(C_2H_5)_2$ to produce the ion g_4, m/z 140, which subsequently eliminates the sulfhydril group and gives the low abundance ion h_4, m/z 107. These typical fragmentation processes and products were found in other phenyl morpholinyl-thiophosphonic alkylesthers [14].

The fission of the O-N bond in $\mathbf{M_4}^{+\cdot}$**,** loosing the neutral group $[C_3H_2N_3O]$, is likely yo result in the ion i_4, m/z 228 (156+NR'$_2$). This undergoes a rearrangement of a H atom from N to O, further losing the neutral radical NC_4H_9, to give the ion j_4, m/z 157. Similar fragmentations were reported in other MS studies on phenyl-morpholinyl-amidothiophosphonic esthers [14]. Metastable ions analysis further supported the formation of the ion k_4, m/z (124+NR'$_2$) by the P-S bond fission in the thion-thiolic isomer of the molecular ion $\mathbf{M'_4}^{+\cdot}$, m/z 324, as observed in other thiono-phosphorylic esthers with aromatic substitutes [10,13].

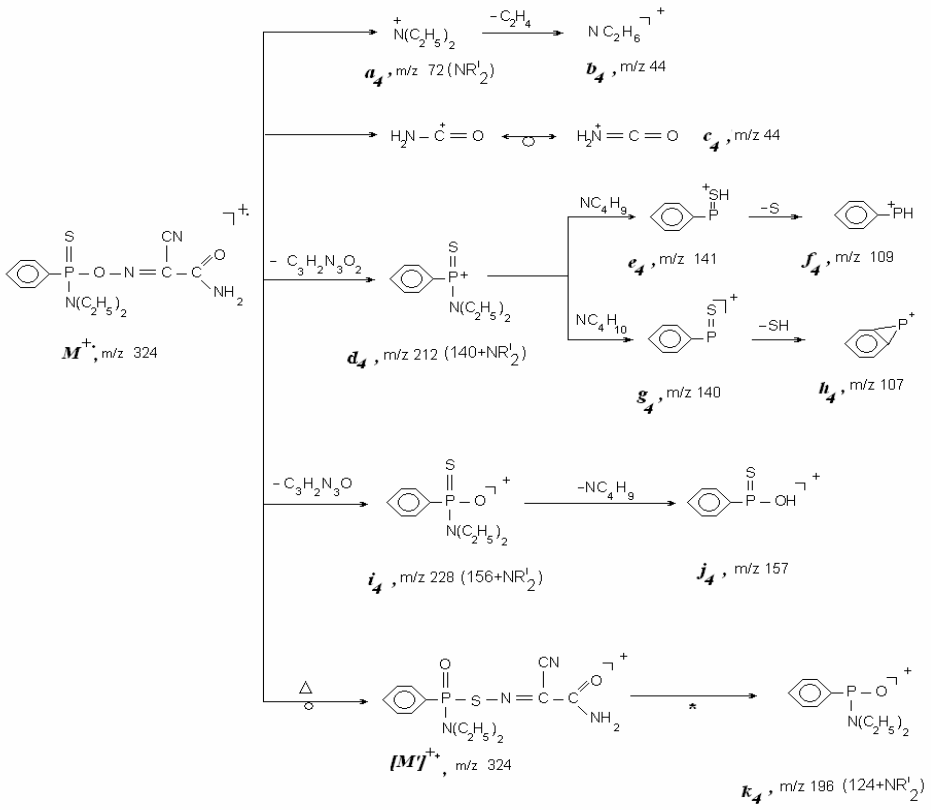

Figure 4. Unimolecular cleavage pathways proposed in compound **4**

CONCLUSIONS

A series of cyanacetamid- and cyanethylacetate oximinic esthers of amidothiophosphonic acids **1-4,** with biological potential, were synthesized and studied by EI mass spectrometry. Very low abundance molecular ions reflect the instability induced by the cyanacethyloximinic group. In compounds **1, 2** and **4,** the cyancetamidic group forms the abundant ion $[NH_2CO]^+$ at m/z 44, stabilized by resonance. The fission of the P-O and O-N bonds generates relatively abundant ions in compounds **1-3**. Rearrangement processes were observed, involving the H transfer from the cyclohexyl- (**1-3**) and diethylamido- (**4**) P substitutes, to the thionic S atom.

REFERENCES

1. Lorentz W., Fest Ch., Hammann I., Federmann M., Fluke W., Stendel W., Farbenfabriken Bayer A.G., DAS 1238902.
2. Billet I., Piscateway N.I., A.P. 3.642.957.
3. Safta M., Hantz A., Chioreanu I., *Rom. P.* 96.504.
4. Safta M., Hantz A., *Rom. P*. 100.896.
5. Fukuto T.R., Metcalf R.L., Jones R.L., Myers R.O., *J. Agr. Food Chem*, **17**; 1969: 923-928.
6. Kromer W., Riebel H.J., Bayer A.G., DE 34 29434 A1.
7. Almasi E., Fenesan I., Biro V., "Uber heteroorganische Verbindungen. LII. Thiophosphonsaureamide und ihre Derivate", *J. Prakt Chemie*, **321**; 1979: 913-920.
8. Fenesan I., Hantz A., Culea M., Alexandrescu S., *"Timisoara Academic Days",* 1995: 123-124.
9. Yamauchi K., Mitsuda Y., Kinoshita H., "Peptides containing aminophosphonic acids, IV- Mass Spectra of the peptides containing aminometylphosphonic acid", *Org. Mass Spectrom*., **12**; 1977: 119-126.
10. Opreanu I., "Spectrometria de masa a compusilor organici", Ed. Dacia, Cluj-Napoca, 1974.
11. Moldovan Z., Palibroda N., Culea Monica, Fenesan I., Hantz A., "Electron impact fragmentation of some cyclohexylthiophosphoroorganic amides", *Org. Mass Spectrom*, **24**; 1989: 81-86.
12. Moldovan Z., Nicoara Simona, Culea Monica, Cozar O., Fenesan I., Vegh P., Rios J.J., "Mass spectra interpretation of some thiophosphororganic compounds", *J. Molec. Structure*, **348**, 1995: 393-396.
13. Fenesan I., Popescu R., Supuran C.T., Nicoara Simona, Culea Monica, Palibroda N., Moldovan Z., Cozar O., "Electron impact mass spectral interpretation for some thiophosphoryl-p-acetylaminobenzene sulfonamides", *Rapid Commun. Mass Spectrom*., **15**, 2001: 721-729.
14. Moldovan Z., Culea Monica, Palibroda N., Fenesan I., Popescu Rodica, "Electron impact mass spectrometry of phenyl thiophosphororganic amides", *Org. Mass Spectrom.*, **26,** 1991: 840-846.

STUDIA UNIVERSITATIS BABES-BOLYAI, PHYSICA, LIV, 1, 2009

STUDY OF INTERACTION BETWEEN GOLD NANOPARTICLES AND PORPHYRINIC DYES

SORINA GARABAGIU[1,2,*], GHEORGHE MIHAILESCU[1]

ABSTRACT. The goal of our research is to investigate the coupling of gold nanoparticles (GNP) with porphyrins molecules. Our work reported here has revealed that a strong and large absorption band is obtained when a complex between gold nanoparticles (GNP) and porphyrin dye is formed. The exchange of the initial ligand (citrate ions) with porphyrins formed hybrid nanostructures and change the electronic properties of GNP. Porphyrins could be used for designing dye sensitized solar cells. The correlation between their band gap HOMO-LUMO and the conduction band of the semiconductor (TiO_2) allow the electron transfer from the dye to the electrode, through the semiconductor.

Keywords: DSSC, GNP

1. Introduction

The production of electrical energy by the direct conversion of solar energy is one of the main issues concerning alternative sources of energy for this century. Currently the most popular methods are silicon based solar cells.

The production of electrical power from sunlight in organic solar cells involves the following: firstly, sunlight photons are absorbed within a photoactive layer leading to the formation of excitons. The excitons migrate to the interface of a donor-acceptor semiconductor hetero-junction and dissociate to form free charges, consisting of electrons and holes, and these charges are moved to the electrodes to eventually yield a photocurrent in an external circuit.

Dye-sensitized solar cells have many advantages over the conventional silicon solar cells [1]. These cells work on principles similar to the processes in natural photosynthesis. They use an organic dye to absorb the incoming light and

[1] National Institute for Research and Development of Isotopic and Molecular Technologies, Ro-400293 Donath str., no. 65-103, P.O. Box 700, Cluj-Napoca, Romania
[2] Babes Bolyai University, Faculty of Physics, Kogalniceanu str. No 1, 400084, Cluj-Napoca, Romania
[*] E-mail: sgarabagiu@itim-cj.ro

produce excited electrons which will generate electrical current. The absorption band of the dye has to be as large as possible, from 350 nm to 900 nm, in the visible and near-infrared region of the solar spectrum. TiO_2-Ru dye sensitized based on solar cells have limited availability and undesirable environmental impact, due to Ru atoms. These facts led to search for cheaper and safer organic-based dyes. Given their efficacy in photosynthesis, porphyrin dyes have great potential in this regard [2-4].

In this work, we investigate the coupling between gold nanoparticles and porphyrins, and these new materials will be helpful to the design of dye sensitized solar cells (DSSC).

2. Experimental

2.1 Materials and methods

Hydrogen tetrachloroaurate ($HAuCl_4$ $.3H_2O$) was purchased from the Institute of Chemistry in Cluj-Napoca, whereas sodium citrate, dichloromethane and tetrabutylammonium perchlorate from Sigma. The porphyrin dye P1:Zn(II)-tetrapyridylporphyrin and P3: Co(II)-tetrakis-4-metoxifenil-porphyrin were synthesized at the Institute of Chemistry, in Timisoara. P2: 2,3,7,8,12,13,17,18-octaethyl-porphyrin was purchased from Aldrich. Double distilled water was used in all experiments.

UV-Vis and fluorescence spectroscopic studies were carried out using a Jasco 550 and Jasco FP-6500.

Gold nanoparticles were prepared using Turkevich method [5]. TEM images (using a JEOL JEM 1010 Transmission Microscope) demonstrated that we have obtained 30 nm gold nanoparticles.

2.2 Discussion and results

After dissolving the porphyrin molecules in dichloromethane, we acquired the absorption spectra of these dyes. The porphyrin dyes have an intense and narrow absorption band at 420 nm (Soret band) and a large, weak band between 500–700 nm (Q band), as seen in figure 1.

Analising the Soret band, with the λ-onset method, we determinate the energy gap between HOMO and LUMO (ΔE_g).

$\Delta E_g(eV)=1240/\lambda$ onset(nm)

Using cyclic voltammetry we obtained the electrochemical spectra of the porphyrins (figure 2), solved in dichloromethane.

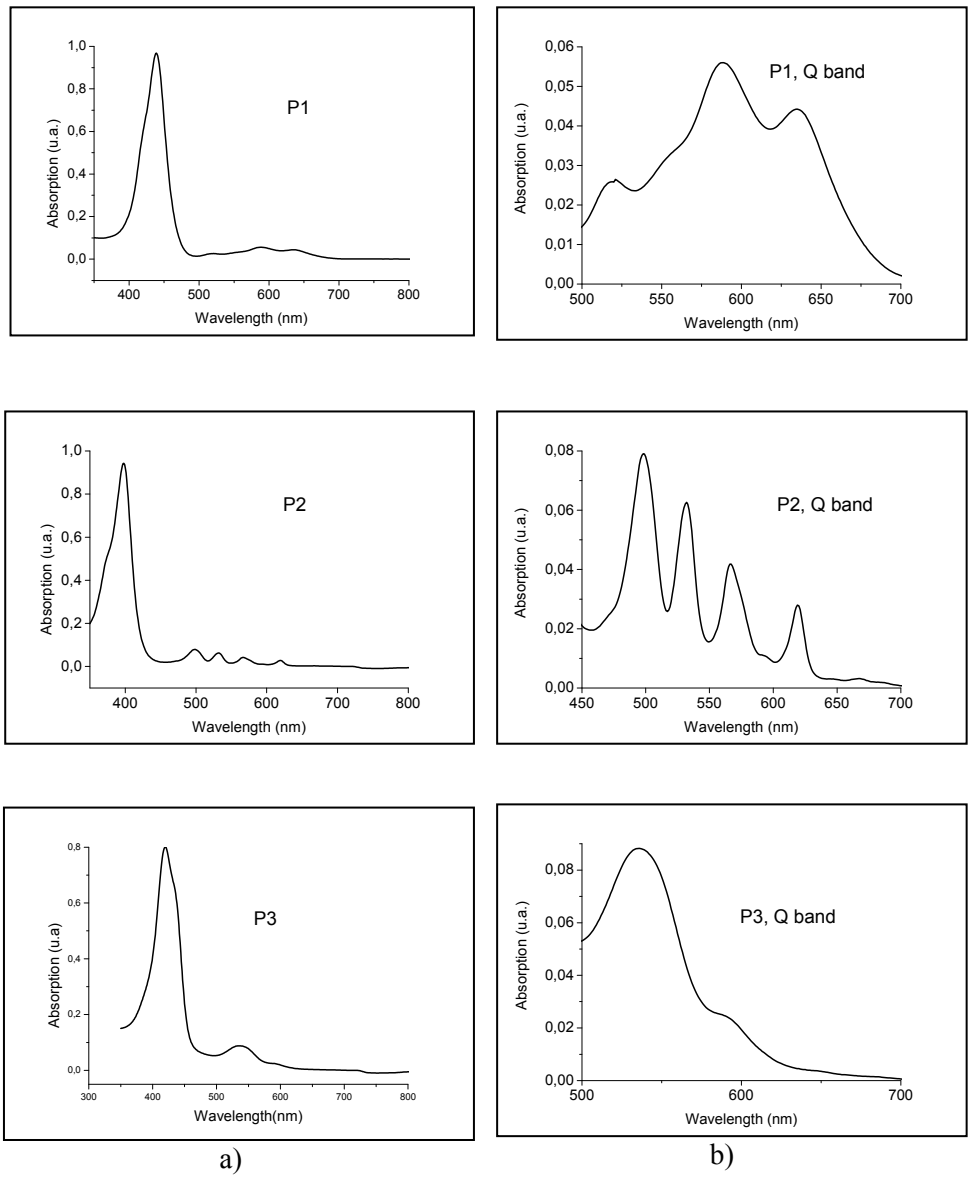

Figure 1. UV-Vis spectra of porphyrins: a) the entire spectra, b) Q band of porphyrins

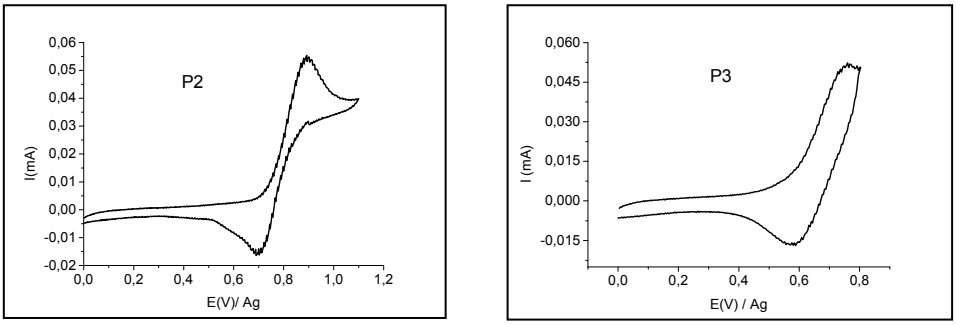

Figure 2. Cyclic voltammograms of P2 and P3

An Ag wire was used as reference electrode. From the cyclic voltammogram, we calculated the redox potential E_0. A conversion was made to NHE. With ΔE_g and E_0 known, it is possible to determine the energy levels HOMO and LUMO, and to compare them with the levels of the semiconductor (TiO_2). The results are shown in Table 1.

Table 1.

E_0, HOMO, LUMO for porphyrins, TiO_2 and electrolyte, with NHE reference

Porphyrin	λ onset (nm)	ΔE_g (eV)	E_0 (eV)	HOMO (eV) (valence band)	LUMO (eV) (conduction band)
P1	469	2.64	-	-	-
P2	423	2.93	0.972	0.972	-1.958
P3	461	2.69	0.852	0.852	-1.838
TiO_2	-	3.2	-	3	-0.2
Electrolyte	-	-	0.3	-	-

To design dye-sensitized solar cells, it is necessary that the dye absorb the visible light and then transfer the photoelectron from his LUMO state to the semiconductor. This orbital must have a higher energy than the conduction band of the semiconductor, so the electron could pass to the semiconductor and then from the electrode, in the external circuit. Also, HOMO energy level of the dye must be lower than the redox potential of the electrolyte.

As can be seen in Table 1 (with NHE reference; view figure 4), LUMO energy state of P2 and P3 have a higher value than the conduction band of TiO_2, which means that the electronic transfer between dye and semiconductor could happen. Also,

the value of redox potential of the electrolyte (E_0) is higher than the corresponding values of the dyes and this facilitate the electron transfer to the oxidized dye.

TiO_2 act like n-type semiconductor, while the dye act like p-type semiconductor. This is why a junction is formed at the interface, and the electrons could pass through it. The figure below shows the electronic transfer in a DSSC.

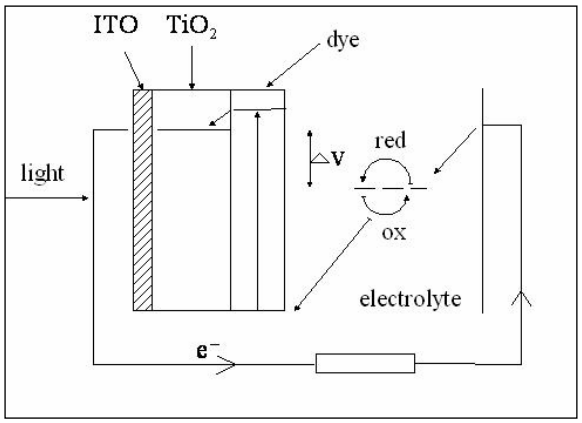

Figure 3. DSSC principle scheme [6]

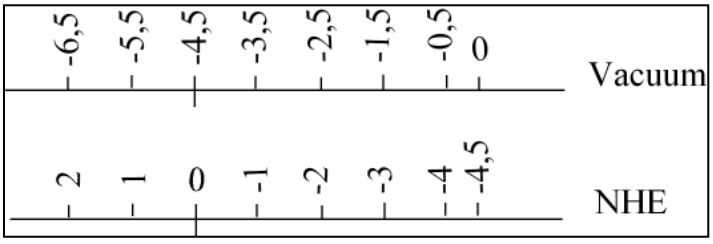

Figure 4. Potential scale of NHE comparative to vacuum

One way to encompass a broader absorption band is the attachment of functional groups on the basis of porphyrins. However this action involves organic synthesis. Gold colloids bearing surface negative charge readily bind the functional groups. This negative charge must be compensated by adding an acidic solution.

These conditions facilitate functionalization and linking of GNP to nitrogen atoms in the porphyrinic structure.

The influence of pH on the reaction between GNP and porphyrins was investigated. There is no shift in the maximum peak position in the UV-Vis absorption spectra of gold nanoparticles until the pH value is 2.5. Our experiments were made at pH=2.52 and the porphyrin we used was P1. In figure 5 is presented the UV-Vis spectra for GNP and the sequential addition of P1, with modified pH. One can see that the plasmon surface peak of GNP in figure 5(a) is attenuated and a signal for the newly formed complexes appear between 500–700 nm. When we mixed a fixed quantity of porphyrin solution with GNP, by adding small drops of the GNP solution, the spectra in figure 5 (b) demonstrate that GNP bind to the porphyrinic ring, as a shift appears in the maximum peak position.

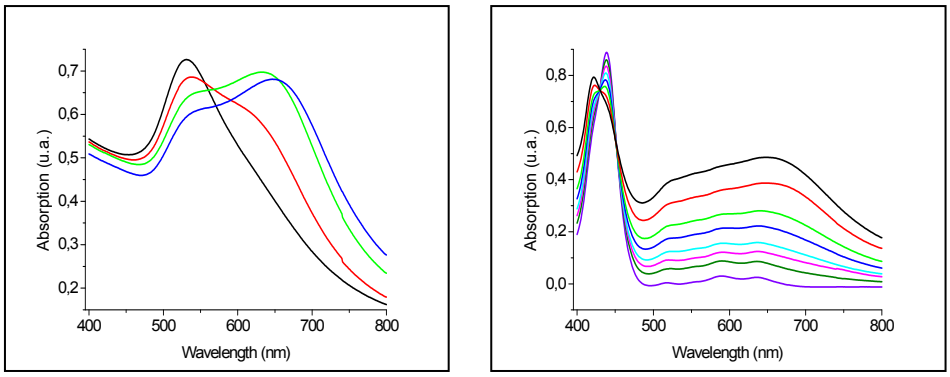

Figure 5. UV-Vis absorption spectra of: a) GNP+$P1_{drops}$; b) P1+GNP_{drops}

This could be due to the attachment of porphyrin molecules to GNP. Metal atoms in the porphyrinic ring are decisive for the lifetime of the electronic excited states, which influence the electron transfer between the dye and the conduction band of TiO_2. Zn porphyrins are more efficient than Cu porphyrins for solar cells because they have a longer lifetime of the electronic excited states [2].

3. Conclusion

In this work we demonstrated that porphyrins could be used for TiO_2 sensitization. An electronic transfer from the porphyrinic dye to TiO_2 is possible due to their HOMO-LUMO energy states. We also proved that some porphyrins interact with gold nanoparticles, and a strong and large absorption band is obtained when a complex between gold nanoparticles and porphyrin dye is formed.

REFERENCES

1. M. Gratzel, *Nature,* **414**, 338, 2001
2. W. M. Campbell, A. K. Burel, D. Officer and K. W. Jolley - *Coord.Chem. Rev.* **248**, 1363, 2004
3. M. Gervaldo, F. Fungo, E. N. Durantini, J. J. Silber, L. Sereno and L. Otero - *J. Phys. Chem. B,* **109**, 20953, 2005
4. J. R. Fish, E. Kubaszewski, A. Peat, T. Malinski, J. Kaczor, P. Kus and L. Czuchajowski - *Chem. Mater.* **4**, 795, 1992
5. J. Turkevich, P. C. Stevenson and J. Hillier - *Discuss. Faraday Soc. II,* **55**, 1951
6. E. Fagadar-Cosma, D. Vlascici, G. Fagadar-Cosma - *Porfirinele, de la sinteza la aplicatii*, Editura Eurostampa, Timisoara, 2008

STUDIA UNIVERSITATIS BABES-BOLYAI, PHYSICA, LIV, 1, 2009

FORCED OSCILLATIONS OF STRATIFIED THIN CORONAL LOOPS DRIVEN BY EIT WAVES

G. MOCANU*, A. MARCU, B. ORZA

ABSTRACT. We study the interaction between thin stratified solar coronal loops and global EIT waves (waves observed in the solar corona in the extreme ultraviolet band filter), considering non–zero gravity and an appropriate density profile for the plasma inside the loop. The EIT force is as an external driver. We discuss the effects of gravitational stratification on the amplitude of forced vibration modes perpendicular to the coronal magnetic field. Our basic mathematical tool is the linear MHD approximation.

Key words: Sun, EIT waves, MHD equations, coronal loops

1. Introduction:

Observations with instruments onboard SOHO, TRACE/EUV, STEREO/EUVI [1, 2] show strong interactions between coronal structures, such as coronal loops and the global EIT wave. EIT waves are global waves propagating in the low solar corona and are generated by coronal mass ejections or flares. Observations show that an EIT wave has two stages. First, the driven stage, where the wave is correlated with radio bursts (the propagating wave can excite plasma radiation and energized particle population serving as a source of radio emission). The second stage consists of a freely propagating wave front. In this stage EIT waves consist of a faster propagating piston–driven portion[1] and a more slowly propagating portion due to the opening of the field lines (correlated with erupting filaments) which interact with coronal loops, forcing them to oscillate. The strength of the interaction and the resulting vibrations depend on the local and global parameters of the loop, such as the loop length and local profile density and also on the energy carried by the wave [1].

In this paper we investigate the transversal spatial displacement induced in a thin stratified loop by interaction with EIT waves. We have derived the governing equations for transversal oscillations based on the equilibrium of forces correlated with continuity of mass and magnetic flux. In the first section, the model and basic equations are presented. The next section includes analytical and numerical analysis

* Department of Theoretical and Computational Physics, Babes-Bolyai University, Cluj Napoca, Romania

for a driving force modeled by a pulse in space, acting in the loop apex. In the last section we summarize our results and discuss some possible extensions.

2. Model and basic equations:

We assume that the coronal loop can be described (with little loss in accuracy) by a magnetic straight flux tube embedded in a magnetic free environment (Figure 1). The atmosphere is isothermal and the plasma inside the tube is in thermal equilibrium with its surroundings. The surrounding atmosphere exhibits the longest timescale in the model, so that $\partial p_e / \partial t = 0$ (the external pressure is constant in time). Gravitation acts on every element of volume and the profile of the equilibrium density is

$$\rho_0(x,z) = \rho_{00}[\rho_{0z}(0)\rho_{0x}(x) + \rho_{0x}(0)\rho_{0z}(z)], \tag{1}$$

where the variations of density along each of the two coordinates are considered to be independent, and

$$\rho_{0z}(z) = e^{-z/L} + \rho_e / \rho_{00}, \tag{2}$$

$$\rho_{0x}(x) = (1 - \rho_e / \rho_{00}) \sec h^2(x/a) + \rho_e / \rho_{00}, \tag{3}$$

where L - distance from the loop foot point to the apex, ρ_e - density of the external medium, assumed to be constant, ρ_{00} - density of the loop at its foot point, a - width of the loop.

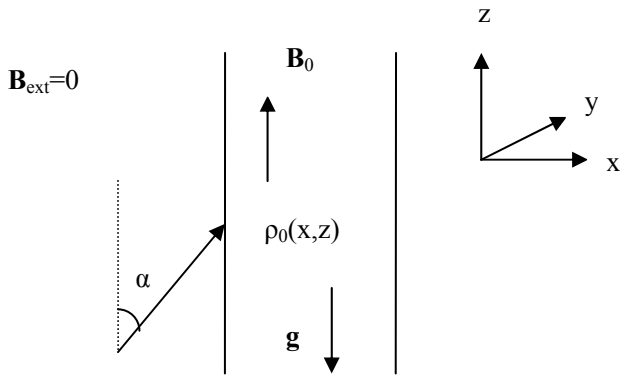

Figure 1. Basic geometry of the model

Starting from the ideal MHD equations (no dissipative mechanisms), in the absence of a background flow in the tube, the liniarized equations yield a system of two coupled differential equations with $v_x(x,z,t)$ and $v_z(x,z,t)$ as unknowns. Further on, we assume that the force exerted by the EIT wave on the loop can be written as [3]

$$F_{EIT}(x,z,t) = \tilde{F}(x,z)e^{i\omega_{EIT}t}, \tag{4}$$

and also that the perturbed velocities are [4]

$$v_x(x,z,t) = \tilde{v}_x(x,z)e^{i\omega t}, \tag{5}$$

$$v_z(x,z,t) = \tilde{v}_z(x,z)e^{i\omega t}.$$

Due to constraints imposed on theoretical models by analysis of observational data, the second order derivatives in the equilibrium density vanish

$$\frac{\partial^2 \rho_0}{\partial x^2} = 0\,,\ \frac{\partial^2 \rho_0}{\partial z^2} = 0. \tag{6}$$

In the thin flux tube approximation (we neglect the variations of all physical quantities with the x coordinate and focus on how the equilibrium is perturbed along the direction of the magnetic field), the two equations uncouple and the equation describing the propagation normal to the magnetic field becomes:

$$v_A^2(x,z)\frac{\partial^2 \tilde{v}_x}{\partial z^2} - \omega^2 \tilde{v}_x = -\frac{1}{\rho_0(x,z)}\omega_{EIT}\sin\alpha\tilde{F}(x,z), \tag{7}$$

where $v_A^2(x,z) = B_0^2/(\mu\rho_0(x,z))$ is the Alfven speed, B_0 is the equilibrium magnetic field and μ is the magnetic permeability of the medium.

The equation describing longitudinal propagation was found to be

$$\tilde{v}_z(\omega^2 + g/\rho_0(x,z)) + \frac{\partial \tilde{v}_z}{\partial z}\left[g + \frac{c_s^2}{\rho_0(x,z)\gamma}(1+\gamma)\right] = \frac{1}{\rho_0(x,z)}\omega_{EIT}\cos\alpha\tilde{F}(x,z), \tag{8}$$

where g is the gravitational constant in the solar corona, c_s is the sound speed and γ is the adiabatic index.

The particular case when the EIT wave hits the loop perpendicularly was considered. The force can be modeled as a pulse in space and the impact takes place at the apex of the loop and so we set $\alpha = \pi/2$ and $\tilde{F}(x,z) = E_{EIT}/\lambda_e\delta(z-L)$ [3]. This analysis was performed for a strong magnetic field and focused on following the behavior of the perturbations along the loop axis. The analytical solution of Eq. (7) is a superposition of Bessel functions, which leads to an overall linear dependency of the perturbed velocity on the distance from the loop's footpoint (Figure 2).

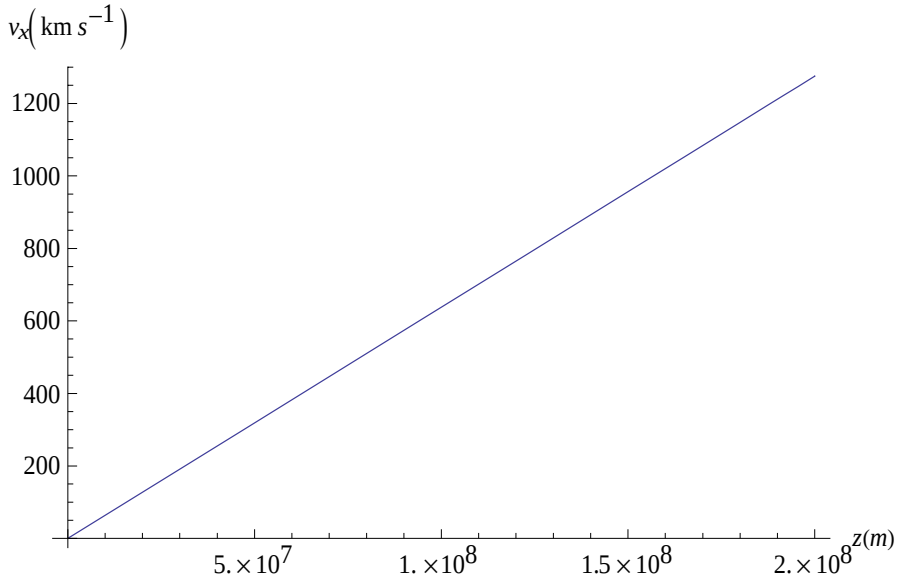

Figure 2. Amplitude of the transversal propagation velocity, for $\alpha = \pi / 2$

This linear behavior was to be expected, since the impact is at the apex and the EIT wave is known to carry a considerable amount of energy. Another observation regarding our results is that the final solution of propagation perpendicular to magnetic field lines does not depend, in the thin loop approximation, on gravity. The calculations we performed show that considering a thick loop would induce a gravity dependency.

3. Results and conclusions:

We obtained two differential equations describing the interaction between a thin loop, under gravitational stratification and a global EIT wave, modeled as a pulse in space, centered at the apex of the loop.

For propagation normal to the magnetic field we found an overall linear dependency on height, with a maximum in the loop apex and no influence of gravity. Analytical calculations show that gravity would be of importance for a thicker loop. Also, the longitudinal propagation is influenced by the effects of gravity in the thin flux tube approximation, as seen in equation (8).

Performing the same analysis but setting the impact angle to a smaller value, does not change the behavior of the disturbance. However, there is a drop in the magnitude of the perturbation velocity. For example, for $\alpha = \pi / 3$ the mean drop in velocity is approximately $200 km / s$. This is consistent with a different distribution of the energy carried by the EIT wave after the impact.

The equilibrium magnetic field is found to have a strong connection with the magnitude of the propagation amplitude. A strong magnetic field will oppose

propagation of disturbances and contribute to lowering their amplitude. The EIT wave will have an apposite effect: propagation amplitudes behave as a signature of the EIT wave energy. Otherwise stated, large amplitude can lead to the conclusion that the EIT wave source is located near the observed loop.

The model presented is a simplification of actual coronal conditions. Further steps can me made to bring the model closer to reality: considering a non–zero external magnetic field and taking into account dissipative mechanisms in order to account for the observed damping of the forced oscillations [8, 9].

REFERENCES

1. I. Ballai, R. Erdelyi, B. Pinter, ApJ, 633, L145, 2005
2. D.M. Long, P.T. Gallagher, R.T.J. McAteer, D.S. Bloomfield, ApJ, 680, 81, 2008
3. I. Ballai, M. Douglas, A. Marcu, A&A, 488, 1125, 2008
4. B. Roberts, SoPh, 69, 27R, 1981
5. B. Roberts, SoPh, 69, 39R, 1981
6. B.J. Thompson, J.B. Gurman, W.M. Neupert et al., ApJ, 517, 151, 1999
7. M.J. Aschwanden “Physics of the Solar Corona”, Springer Praxis Books, Subseries “Astronomy and Planetary Science”, 2006
8. M.S. Ruderman, B. Roberts, ApJ, 577, 475, 2002
9. J. Terradas, R. Oliver, J.L. Ballaster, A&A, 441, 371, 2005

STUDIA UNIVERSITATIS BABES-BOLYAI, PHYSICA, LIV, 1, 2009

INFLUENCE OF THE SINTERING TEMPERATURE ON STRUCTURE, ELECTRIC AND MECHANICAL PROPERTIES OF THE POLYCRYSTALLINE (Bi,Pb):2223 SUPERCONDUCTORS

A.V. POP[1*], ROXANA COLDEA[1], C. LUNG[1], GABRIELA STIUFIUC[1], MARIANA POP[2]

ABSTRACT. Bulk superconducting materials with nominal composition $(Bi_{1.6}Pb_{0.4})(Sr_{1,8}Ba_{0,2})Ca_2Cu_3O_y$ were synthesized by solid state reaction method by using different sintering temperature (in the range 840^0C- 850^0C). X-ray diffraction pattern shows that in all samples the majority phase is 2223, with some traces of Bi:2212. The electrical properties of the samples were examined by electrical resistance versus temperature, R(T). By using the linear behavior for R(T), the influence of sintering temperature on the parameters related to inter-grain resistivity and the percolation conduction were evaluated. To study the mechanical properties of Bi:2223 samples, Vickers micro hardness were measured. The variation of micro hardness with load is nonlinear, and described by Mayer's law.

Keywords: Bi2223 bulk HTS, different sintering temperature, X-ay diffraction, electric resistance, Vickers micro hardness

1. Introduction

Since the BSCCO phases have a plate-like morphology with a high current carrying capacity in the a–b plane and also owing to the importance of this system, researchers have been trying to develop the practical application potential of it. BSCCO system contains basically two high - Tc phases, one is 2212 (Tc =80 K) and the other is the high 2223 phase (Tc =110 K).

In bulk materials, grain boundaries present barriers to the passage of current and acts as a weak links (structural misalignment, dirt or other impurity phases, oxygen vacancies etc) [1].The current can pass through many different path through grain boundaries, and the bulk SC is a multiple Josephson junction array. Misalignment between grains and their boundaries causes degradation of J_c, particularly in magnetic fields.

[*] *E-mail address*: avpop@phys.ubbcluj.ro, Tel:+4-0264-594315/int.5150; Fax:+4-0264-591906
[1] University Babes-Bolyai, Faculty of Physics, University "Babes-Bolyai",400084 Cluj-Napoca, Romania
[2] Technical University Cluj-Napoca, Faculty of Materials Science and Engineering, 400641, Cluj-Napoca, Romania

The bulk (Bi,Pb):2223 material consists of grains weakly coupled at the grain boundaries by junctions or weak links. The quadratic temperature dependence of J_{cj} near T_c suggests SNS junctions between the grains [2,3].

The intra- and intergrain properties of (Bi,Pb):2223 system are different influenced by the partial substitution of copper (Cu) by 3d elements [4,5]. It is difficult to synthesize 2223 in single phase from $Bi2Sr2Ca2Cu3O_y$ alone. The annealing process is one of the important methods to accelerate the formation of the 2223 phase [6] and to obtain materials with superconducting and Vickers hardness properties for commercially useful applications.

In this paper we report the influence of sintering temperature on electrical resistance and Vickers micro hardness of (Bi,Pb)(Sr,Ba):2223 bulk superconductor.

2. Experimental

Bulk samples with nominal composition $(Bi_{1.8}Pb_{0.4})Sr_{1.88}Ca_2Cu_3O_y$ (Sample A_1) and $(Bi_{1.6}Pb_{0.4})(Sr_{1.8}\ Ba_{0.2}\ )\ Ca_{\ 2}\ Cu_3\ O_y$ (Sample T_1 sintered at 850^0C and sample T_2 sintered at 855^0C) were obtained by the conventional solid-state reaction of appropriate amounts of the metal oxides and carbonates of 99.99% purity. The partial substitution of Sr by Ba was used to induce the reduction of the modulation period [7]. Appropriate amounts of Bi_2O_3, PbO, $SrCO_3$, BaO, $CaCO_3$, and CuO were mixed in agate mortar and calcined at 800 ^{0}C for 36 hours. The calcinated powder was pressed into pellets and presintered at 845 ^{0}C for 200 hours and finally sintered at 850^0C for 150 hours (samples A_1 and T_1) and 855 ^{0}C respectively (sample T_2).

At the end of sintering process the pellets were allowed to furnace-cool to room temperature.

We have evaluated both the phase purity and the texture degree in bulk samples by means of X-ray diffraction analysis (XRD) preformed in a Bruker diffractometer. The patterns were taken at room temperature using CuK_α radiation in the with a 0.02^0 (2θ) step size and 5 s of counting time.

The standard dc four point method was used for electrical resistance measurements. We used conductive silver paste with which golden leads were attached to the specimens.

After cooling the sample in zero applied magnetic field down to 77 K, an excitation current of 1 mA was injected along the slab sample.

The temperature was collected when the temperature was raised slowly to 300 K.

The Vickers microhardness was measured using a microhardness tester with pyramid indenter. For the examined samples, the contact loads (P) ranged from 2.490 N to 0.245 N. A loading time of 10 s was used to measure the diagonal length of indentation (d) with an accuracy of ±0.1 μm. An average of 6 indentations at different locations on the specimen surface was done to obtain representative mean values for each load.

3. Results and discussions

Figure 1 shows the X-ray diffraction patterns taken on bulk samples A_1, T_1 and T_2. The (XRD) analysis confirmed that all samples have similar chemical composition. All the indexed reflections for sample T_2 are related to the high - Tc Bi - 2223, and with a few of peaks belonging to the "2212" and "2201" phases in A_1 and T_1 samples.

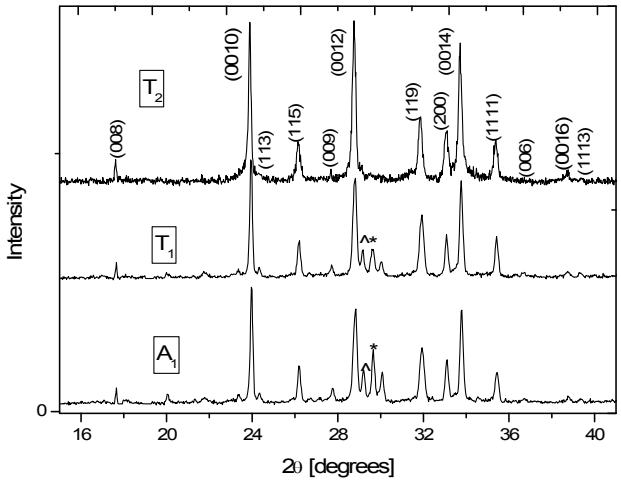

Figure 1. X-ray diffraction patterns of samples sintered at different temperatures A1, T1 and T2. The reflections belonging to the Bi-2223 phase are marked by Miller indexes , the reflections from Bi:2212 by stars(*) , and the reflections from Bi:2201 by (^).

The unit-cell parameters were calculated with respect to an orthorhombic unit cell and the obtained values a = 5.418 Å, b = 5.421 Å, and c = 37.164 Å are very similar for all samples. These calculated values are in excellent agreement with the ones reported elsewhere for the similar compounds [8].

Another feature of the above X-ray diffraction patterns are related to the behavior of some reflections with the increasing sintering temperature. A careful analysis of height of the X-ray diffraction patterns data indicates that the height of peaks (0010), (0012) and (0014) increases with increasing sintering temperature for sample T_2, in contrast with the decrease of the relative intensity of the peak (200). These results suggest that the increase of sintering temperature improved the grains orientation and then the texture of sample T_2.

Figure 2 shows the temperature dependence of the electrical resistivity $\rho(T)$ of samples A_1, T_1 and T_2. The curves for T_1 and T_2 exhibit a midpoint critical transition temperature to the superconducting state T_c = 109.5 K and the curve for A_1 exhibit T_c =108K. The temperature in which the zero resistance state at sample

level is observed, $T_c(\rho=0)$, increases with increasing sintering temperature (see Table 1). The $T_c(\rho=0)$ data indicate that the increase of sintering temperature result in a better connectivity between grains, besides a higher alignment of them along the c-axis, as inferred from the XRD analysis.

Above the excess conductivity region, in the 190K-290K temperature range, our samples are characterized by a linear temperature dependence of the electrical resistivity:

$$\rho = \rho_0 + a*T \quad (1)$$

where ρ_0 is the residual resistivity and a is the slope of resistivity in the normal state.

The metallic-like behavior in the normal-state region of ρ (T), suggest that the electrical current flows preferentially along the ab-plane of the oriented grains in these samples.

As shown in Table1, the ρ_0 and a parameters were influenced by the chemical composition and thermal treatments. The increase of ρ_0 with sintering temperature suggest that the number of scattering centers increase.

The measured normal resistivity in bulk samples is related to the intrinsic resistivity in CuO_2 (a-b) plane of a single crystal, by the relation [14]:

$$\rho = p(\rho_{ab} + \rho_{ct}) \quad (2)$$

The coefficient p account for a mean percolative lengthening of the conduction paths and for the mean shrinking of the current cross-section [1, 9]:

$$\rho_{ab} = \rho_{0i} + \alpha_i*T \quad (3)$$

is the in plane resistivity for a single crystal and ρ_{ct} is associated with the contact resistance between the grains.

We obtain $p = a/\alpha_i$, by using for Bi:2223 single crystal the intrinsic value is around $\alpha_i = 0.75\ \mu\Omega\ cm\ K^{-1}$.

In A_1 and T_1 samples, approximately the same value of p suggest for the percolative conduction, similarly transport cross sections and lengthening of conduction path. For T_2 sample, the decrease of p suggests a gradual increase of the transport current cross sections and decreasing lengthening of conduction paths with increasing sintering temperature.

On the other hand, the term ρ_{ct}, in Eq. (2), is the average intergranular electrical resistivity that is assumed to be temperature - independent, and can be obtained by utilizing the expression $\rho_{ct} = \rho(0)/p$ (see table 1).

Similarly results were obtained on single phase $Bi_{1.65}Pb_{0.35}Sr_2Ca_2Cu_3O_{10+d}$ ceramic samples, obtained by solid-state reaction method and pressed uniaxially at different compacting pressures ranging from 90 to 600 MPa before the last heat treatment [10].

Table 1.

The parameters obtained from resistivity data.

Sample	T_c [K]	$T_c(\rho=0)$ [K]	$\rho(0)$ [μΩ.cm]	$a=d\rho/dT$ [μΩ.cm/K]	p	$\rho_{ct.}$ [μΩ.cm]
T2	109.5	108	50	1.27	1.7	29
T1	109	106.5	196	3.88	5.17	38
A1	108	105	228	4.65	6.2	37

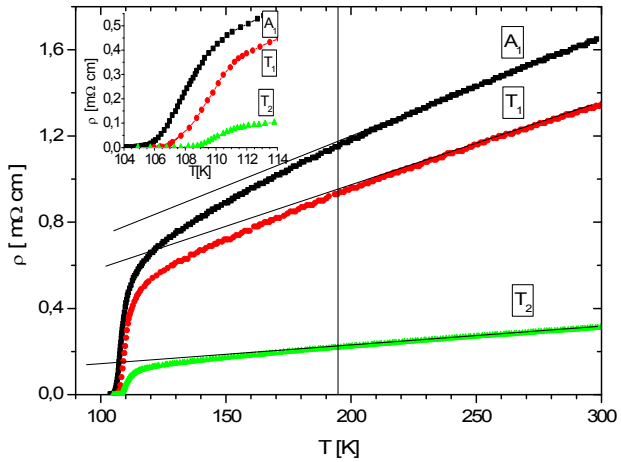

Figure 2: Temperature dependence of the electrical resistivity of samples A_1, T1 and T2. The extrapolation of linear fitting of ρ (T) curves are displayed.

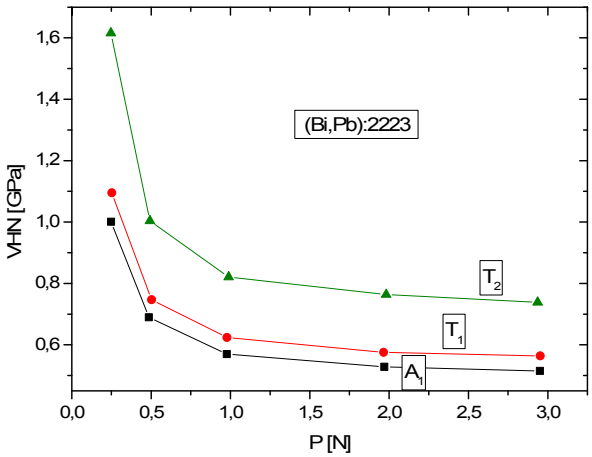

Figure 3. The variation of microhardness with applied load of samples A_1 ,T_1 and T_2.

Figure 3 displays the change of the Vickers microhardness (VHN) values with the applied load for of samples A_1, T_1 and T_2. For a load around 0.25 N, the increase of VHN values from 1 GPa to 1.6 GPa by increasing sintering temperature (samples T1 and T2) may be ascribed to the formation of good conducting channels between superconducting grains which can enhances the bridging between them. The curves in the graph show that the microhardness values decrease non-linearly as the applied load increases up to 0.9 N, thereafter, the VHN values tend to attain saturation. This type of non-linear behavior has also been observed for $Bi_4Sr_3Ca_3Cu_6O_x$ superconductor and is termed an indentation size effect (ISE) and this behavior was explained qualitatively on the basis of penetration depth of the indenter [11].

For small loads, the indenter penetrates only the surface layers and the change in microhardness is pronounced. By increasing loads the effect of inner layers becomes more prominent, and the change in microhardness is small.

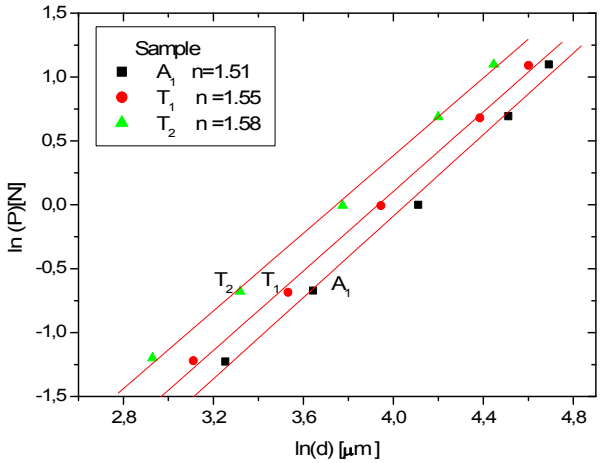

Figure 4. The applied load LnP with the Vickers diagonal Lnd for the samples A_1, T_1 and T_2.

The simplest way to describe the relationships between the applied test load ‘‘P’’ and indentation diagonal length ‘‘d’’ is Meyer’s Law (1908) [12, 13]:

$$\text{Log } P = n\log d + \log K,$$

where ‘‘n’’ is the Meyer number (or index) and ‘‘K’’ is the standard hardness constant. The values of Meyer’s index n are used as a measure of ISE.

The values of n and K in may be obtained from the plots of LnP against Lnd. Typical plots of the dependence of LnP and Lnd for BSCCO samples A_1, T_1 and T_2 are shown in Figure 4. The determined n values obtained from the slopes of the best-fit lines for samples A1, T1, T2 are:1.51;1.55 and 1.58, respectively. The values $n < 2$, shows that the hardness increases with decreasing applied load, which

is termed normal ISE [11]. These values of n indicate that Meyer's Law is obeyed in our results. This observation is in agreement with experimental results in the literature [11, 14].

4. Conclusions

X-ray diffraction analysis shows that the majority phase in all samples are Bi: 2223, and suggest that the increase of sintering temperature improved the grains orientation and then the texture of sample.

Above the excess conductivity region all studied samples are characterized by a linear temperature dependence of the electrical resistivity. The residual resistivity and the coefficient p evaluated from resistivity data, are sensitive to sintering temperature. The decrease of p suggests a gradual increase of the transport current cross sections and decreasing lengthening of conduction paths with increasing sintering temperature.

The Vickers microhardness (VHN) was found to increase by increasing sintering temperature of samples.

The measured microhardness values of the BSCCO materials are loaded dependent. The variation of microhardness with load is non-linear and related to the indentation size effect (ISE).

Acknowledgments

The authors are grateful to CNMP-PN II (grant 71-140) and CNCSIS Romania for the financial support.

REFERENCES

1. J. Halbritter, Phys. Rev. B **48** 9735(1993).
2. D. Pandey, S.S.R. Inbanathan, P.K. Srivastava, A. Banerjee and G. Singh, Physica **C261**, 157(1996).
3. A.V. Pop, R. Deltour, A. Harabor, D. Ciurchea and Gh. Ilonca, *Int. J. Mod. Phys*. **B11**, 3461(1997).
4. A.V. Pop, Gh. Ilonca, D. Ciurchea, M. Ye, I.I. Geru, V.G. Kantser, V. Pop, M. Todica and R. Deltour, *J.Alloys and Compounds* **241**,116(1996).
5. A.V. Pop, Supercond. Sci. Technol. **12** 672(1999).
6. S.M. Khalil, A.M. Ahmed, Physica **C 452** 21-28 (2007).
7. A.A. El-Abar, P.J. King, K.J. Maxwell, J.R. Owers-Bradley and W.B. Roys, Physica **C 198**,81(1992).
8. E. Govea-Alcaide, R.F. Jardim, P. Mune, Physica **C 423**,152–162 (2005).
9. A. Diaz, J. Maza, F. Vidal, Phys. Rev. **B 55**, 1209 (1997).

10. E. Govea-Alcaide, R.F. Jardim, P. Mune, Physica **C 423,** 152–162 (2005).
11. S.M. Khalil, A.M. Ahmed, Physica **C 452**, 21–28.
12. (2007) K. Sangwal, B. Surowska, Mater. Res. Innov. **7,** 91 (2003).
13. R. Tickoo, R.P. Tandon, K.K. Bamzai, P.N. Kotru, Mater. Chem.Phys**. 80**, 446 (2003).
14. U. Kolemen, O. Uzun, M. Yilmazlar, N. Guclu, E. Yanmaz, J. Alloys Compds., 415 (2006).

STUDIA UNIVERSITATIS BABES-BOLYAI, PHYSICA, LIV, 1, 2009

CRYSTALLOGRAPHIC AND ELECTRONIC STRUCTURE OF $Ni_{0.7-X}Al_XMn_{0.3}$ ALLOYS

V. REDNIC[1,2], M. COLDEA[1], O. ISNARD[3], M. NEUMANN[4], L. REDNIC[1]

ABSTRACT. X-ray diffraction and photoelectron spectroscopy measurements of $Ni_{0.7-x}Al_xMn_{0.3}$ (x=0.0, 0.1, 0.2, 0.3, 0.4, 0.5, 0.7) alloys are reported. A change in the crystallographic structure takes place around x=0.2 from $AuCu_3$ to CsCl (B2) structure type. The decrease of the Ni 2p satellites as the Al concentration increases may be explained by the hybridization of the Ni 3d and Al 3sp states, which leads to a partial filling of the Ni 3d band. The Ni 2p core level lines and the valence band centroids are shifted towards higher binding energies and the density of states at Fermi level decreases as the Al concentration increases, confirming the partial filling of the Ni 3d band. XPS core-level spectra evidenced the existence of local magnetic moments confined at Mn sites.

Keywords: transition metal, alloy, magnetic measurements, XPS spectra, local moments

1. Introduction

The problem of local moments confined to the transition metals (T) sites, i.e., localized behaviour in some aspects of itinerant electrons, is one of the most important issues in the physics of the magnetic alloys and intermetallic compounds [1]. It was found experimentally that under certain conditions the magnetic moment of a transition metal remains localized when solute in another transition metal. The condition for the existence of the local moment at the T site is $\pi\Delta / U < 1$, where Δ is the width of the d states (corresponds to the virtual bound states in the Friedel's model [2]) and U is the Coulomb correlation energy between d electrons [3].

The 3d band width $\Delta \approx Z^{1/2}J_h$ depends on the number of near-neighbors Z with d orbitals and the hopping integral J_h, which is very sensitive to the distance between the atoms [4]. On the other hand, the strength and the sign of the interaction between the neighboring local moments are determined by the occupation fraction of d-orbitals and the orientation of these orbitals in the lattice [5]. By alloying with other elements, the vicinity of the transition metal atom is changing. This leads to structural modifications with remarkable variations in the electronic structure and magnetic properties of the parent compound.

[1] Babes-Bolyai University, Faculty of Physics, Kogalniceanu 1, 400084 Cluj-Napoca, Romania
[2] National Institute for Research and Development of Isotopic and Molecular Technologies, P. O. Box 700, 400293 Cluj-Napoca, Romania
[3] Laboratoire de Crystallographie CNRS, Asocie a l'Universite J. Fourier, 38042 Grenoble Cedex 9, France
[4] University of Osnabrück, Fachbereich Physik, 49069 Osnabrück, Germany

The aim of this paper is to study the effect of substitution of Ni by Al atoms on the crystallographic and electronic structure of $Ni_{0.7-x}Al_xMn_{0.3}$ alloys.

2. Experimental

Seven samples from the $Ni_{0.7-x}Al_xMn_{0.3}$ system (x=0.0, 0.1, 0.2, 0.3, 0.4, 0.5, 0.7) were prepared by argon arc melting method. The samples were melted repeatedly (at least four times) in the same atmosphere to ensure homogeneity. The weight loss of the final furnace-cooled samples was found to be less than 1%. The purity of starting materials was 99.999% for Al and 99.99% for Mn and Ni. XRD measurements were performed on polished surfaces using a Bruker D8 Advance diffractometer, due to the hardness of the samples. The broad character of the peaks indicates the presence of the strains in the samples.

The XPS spectra were recorded using a PHI 5600ci ESCA spectrometer with monochromatized Al Kα radiation at room temperature. The pressure in the ultra-high vacuum chamber was in the 10^{-10} mbar range during the measurements. The samples were cleaved in situ. The surface cleanness was checked by monitoring the O 1s and C 1s core levels in the survey spectra.

3. Results and discussions

X-ray diffraction patterns are presented in Fig.1. All the investigated alloys are single phases except for $Al_{0.7}Mn_{0.3}$ and $Ni_{0.5}Al_{0.2}Mn_{0.3}$ alloys. XRD measurements revealed a change in the crystallographic structure around x = 0.2 from $AuCu_3$ to CsCl (B2) structure type. $Ni_{0.5}Al_{0.2}Mn_{0.3}$ appears as a mixture of these two structures. The results from the single phase alloys only are presented.

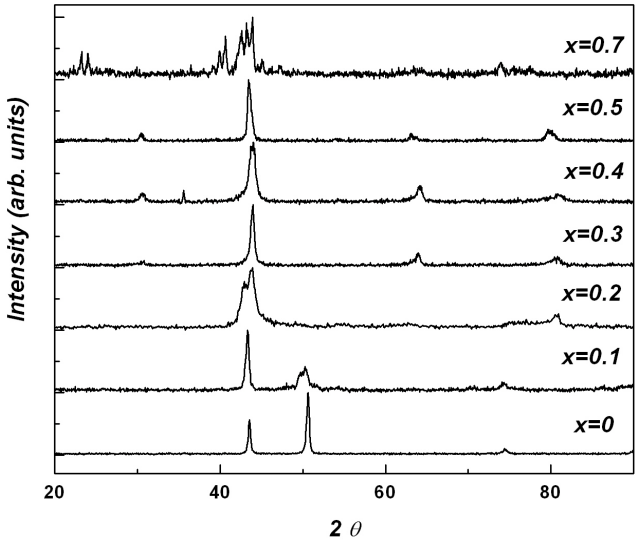

Fig. 1. X-ray diffraction pattern of $Ni_{0.7-x}Al_xMn_{0.3}$ alloys

XPS valence band spectra of the $Ni_{0.7-x}Al_xMn_{0.3}$ alloys are shown in Fig. 2. For Al K_α radiation, the Ni 3d cross section is about four times larger than the Mn 3d cross section [6]. Taking also into account the ratio between the contents of Ni and Mn in the alloys, one can say that the valence-bands spectra of $Ni_{0.7-x}Al_xMn_{0.3}$ alloys, at high Ni concentrations, are dominated by the Ni 3d states, which are preponderant at the Fermi level as in metallic Ni.

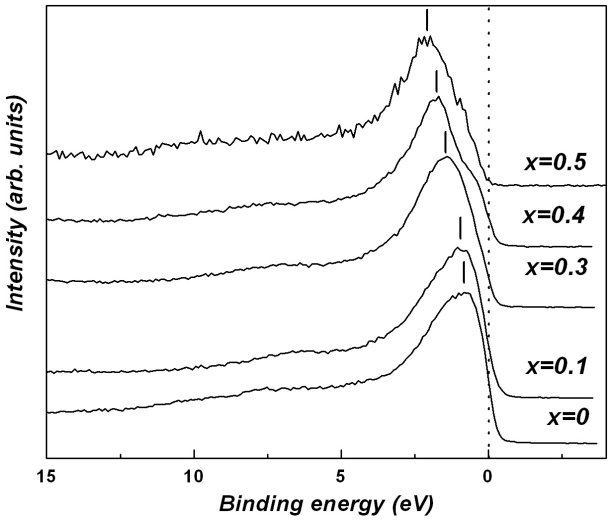

Fig. 2. XPS valence band spectra of $Ni_{0.7-x}Al_xMn_{0.3}$ alloys. The dotted line and the bars indicate the Fermi level and the position of the valence band centroids

The Mn 3d states are concentrated at the bottom of the valence band in the region around 3 eV binding energy [7-9] and become more visible at low Ni concentrations. The XPS valance band spectra for small x present satellite structures at about 6.5 eV, which gradually disappears with the increase of Al content. The valence band centroids are shifted towards higher binding energies and the density of states at Fermi level decreases as the Al concentration increases, suggesting a gradual filling of the Ni 3d band due to hybridization of the Al 3sp and Ni 3d states. In d-band metals and alloys the 3d states are shifted gradually to higher binding energy with the increase in the d-state occupancy and consequently a decrease in the density of states at the Fermi level occurs[10]

The Ni 2p core-level spectra of $Ni_{0.7-x}Al_xMn_{0.3}$ alloys are shown in Fig. 3. The Ni $2p_{3/2}$ core level spectra exhibit satellite structures at about 6.5 eV higher binding energy. In fig. 4 are given the curve fitting results for x=0, x=0.5 alloys and the Al concentration dependence of Ni $2p_{3/2}$ satellite area. As the Al concentration increases, the Ni 2p core-level lines are shifted to higher binding energy. These small chemical shifts are due to the change in the filling degree of the Ni 3d band, which leads to an increase in the electronic density around the Ni 2p shell.

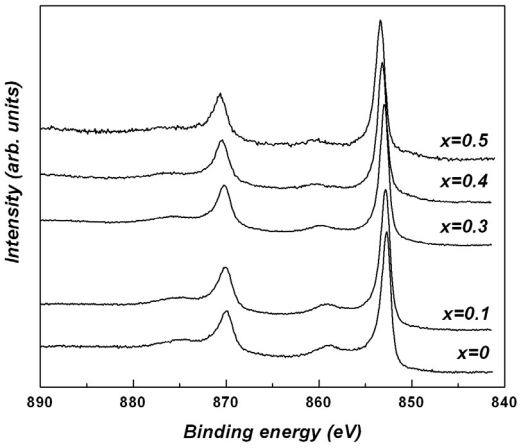

Fig. 3. Ni 2p XPS spectra of $Ni_{0.7-x}Al_xMn_{0.3}$ alloys

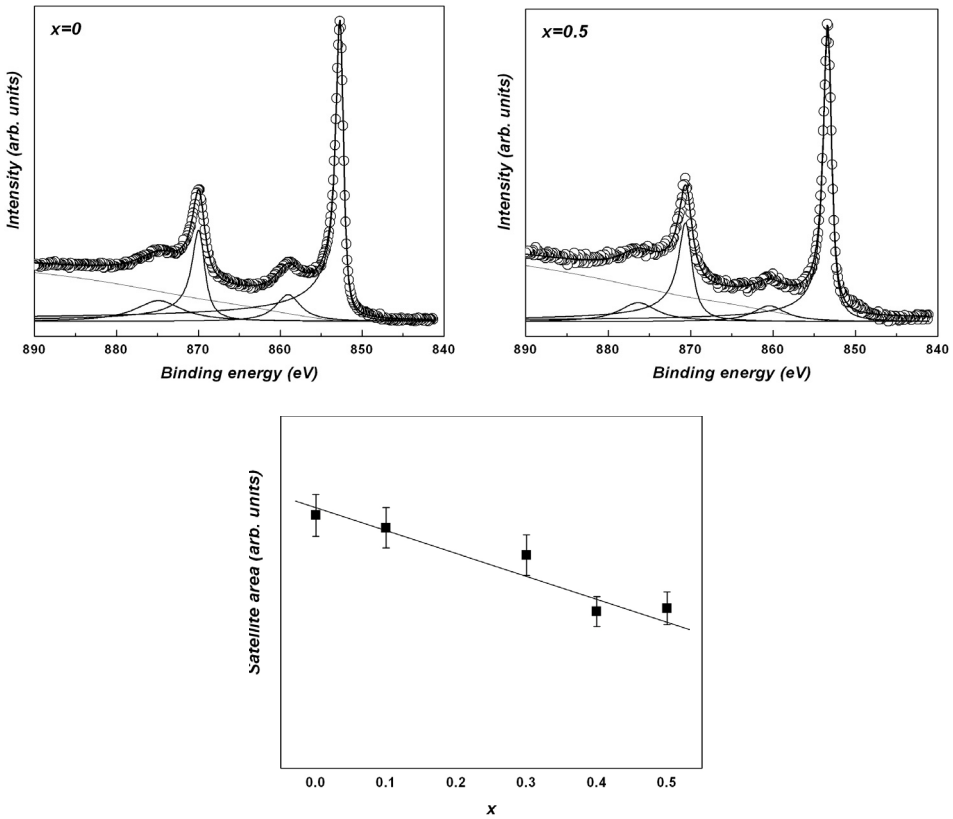

Fig .4. Ni 2p curve fitting results of $Ni_{0.7-x}Al_xMn_{0.3}$ alloys and the Al concentration dependence of Ni $2p_{3/2}$ satellite area

The observation of satellites implies the presence of d character in the unoccupied bands. The satellite structure intensity decreases as the Al content increases, confirming the gradual filling of the Ni 3d band. The presence of the satellite structures suggests that Ni atoms could carry a magnetic moment, but only the magnetic measurements at low temperatures can prove if the Anderson condition for the existence of the local moment at the Ni site is fulfilled.

There is an overlapping between Mn2p XPS line and Ni $L_2M_{23}M_{45}$ Auger line (Fig. 5). The observed spin orbit splitting, which can be identified in the distance between the two centers of energy of the $2p_{3/2}$ and $2p_{1/2}$ state, is $\Delta_{so}\approx 11.5$ eV.

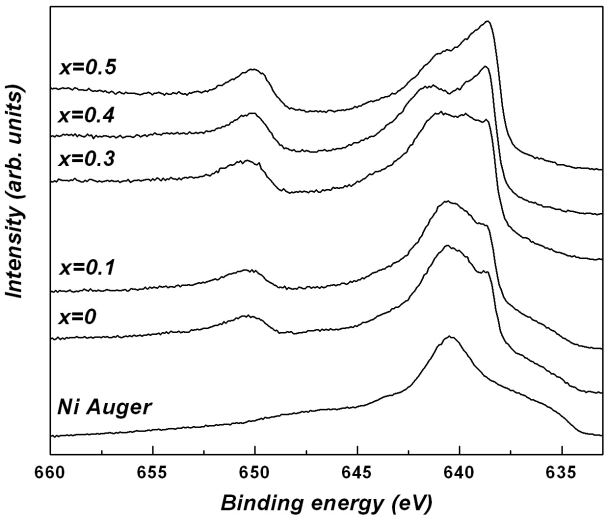

Fig. 5. Mn 2p XPS spectra of $Ni_{0.7-x}Al_xMn_{0.3}$ alloys and Ni Auger line

By using the fully relativistic photoemission calculations for Mn-based Heusler alloys, Plogmann *et* al. found a splitting of the $2p_{3/2}$ states into four sublevels, with an energy separation of 1.0-1.5 eV for all the alloys [11, 12]. After Ni Auger line extraction and background removal, using a Shirley-type background shape [13], we have also fitted the Mn $2p_{3/2}$ core-level spectra for some of the investigated alloys with four components and a satellite line situated at binding energy around 644.5 eV. The curve fitting results for $Ni_{0.7}Mn_{0.3}$ alloy is given in Fig. 6, with the mean energy separation $\Delta_{ex}\approx 1.2$ eV. Similar results were obtained in other alloys based on Mn [14, 15].This gives direct evidence of the existence of local moments confined on Mn sites.

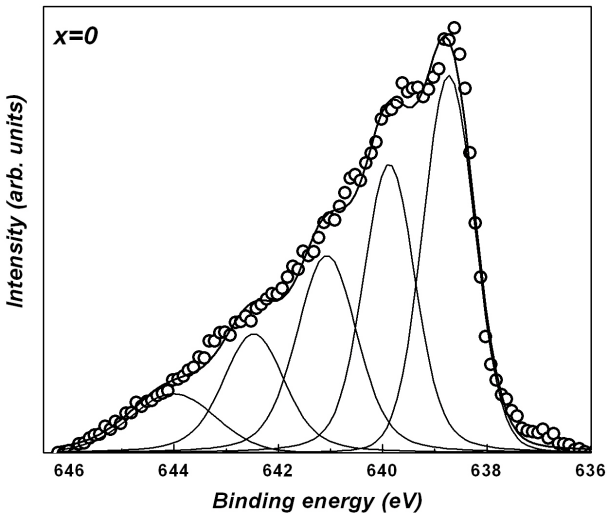

Fig. 6. Mn $2p_{3/2}$ curve fitting results of $Ni_{0.7}Mn_{0.3}$ alloy

Conclusions

The substitution of Al for Ni in $Ni_{0.7}Mn_{0.3}$ leads to significant changes in the crystallographic structure with remarkable effects on the electronic structure of $Ni_{0.7-x}Al_xMn_{0.3}$ alloys. XPS spectra pointed out the existence of local magnetic moments on Mn sites in $Ni_{0.7-x}Al_xMn_{0.3}$ alloys. Ni 2p core-level spectra evidenced the existence of unoccupied 3d states, which is one of the conditions for the apparition of local magnetic moments at Ni sites. The hybridization between the 3d Ni and 3sp Al states leads to a partial filling of the Ni 3d band, as indicated by the XPS core level and valence band spectra.

REFERENCES

1. V. Yu. Irkhin et al, J. Phys.: Cond. Matter **5** (1993) 8763
2. J. Friedel, Nuovo Cimento, Suppl. **2** (1958) 287
3. P. W. Anderson, Phys. Rev. **124** (1961) 41
4. M. A. Howson, Contemporary Physics **35** (1994) 347
5. T. Moriya, J. Magn. Magn. Mat. **10** (1983) 31
6. J. Yeh, I. Lindau, At. Data Nucl. Tables **32** (1958) 1
7. Y. Kurtulus and R. Dronskowki, J. Sol. State Chem., **176** (2003) 390

8. R. Y. Umetsu, K. Fukamichi, A. Sakuma, J. Magn. Magn. Mat. **239** (2002) 530
9. S. Plogmann, T. Schlatholter, J. Braun, M. Neumann, Yu. Yarmoshenko, M. V. Yabloskikh, E. I. Shreder, E. Z. Kurmaev, Phys. Rev. B (1999) 60
10. P. Steiner, H. Höchst, S. Hüfner, J. Phys. F, **7** (1977) L105
11. S. Plogmann et al, Phys. Rev. B **60** (1999) 6428
12. Yu. M. Yarmoshenko et al, Eur. Phys. J. B **2** (1998) 1
13. D.A. Shirley, Phys. Rev B **5** (1972) 4709
14. V. Rednic, M. Coldea, S. K. Mendiratta, M. Valente, V. Pop, M. Neumann and L. Rednic, J. Mag. Mag. Mat, DOI: 10.1016/j.jmmm.2009.06.020
15. R. Pacurariu, V. Rednic, M. Coldea, D. Benea, V. Pop, O. Isnard, and M. Neumann, Phys. stat. sol. (b), 246 (2009) 50-55

STUDIA UNIVERSITATIS BABES-BOLYAI, PHYSICA, LIV, 1, 2009

NEUTRON AND GAMMA DOSE RATE MEASUREMENTS IN THE VICINITY OF THE MEDICAL LINEAR ACCELERATORS

E. HORJ[1], L. DARABAN[1], I. CHEREJI[2]

ABSTRACT. We demonstrate that in the accelerator γ therapy there is an undesirable neutron contamination due to the nuclear reactions (γ,n) type at energies of the gamma radiation higher than 10 MeV, increasing the total biological dose.

This paper presents and discusses the results of the dose rate measurements in the case of gamma irradiation and that of neutron produced in different position chosen near the treatment room for both medical accelerators "Saturne 41" and "Primus".

Using a Neutron Detector FHT 757, designed to successive measure the neutron and gamma radiation the measurements were made during the patients irradiation, in the intention to obtain values as close to reality.

Keywords: γ therapy, dose rate, biological dose

1. Introduction

Medical linear accelerators produce a beam of high energy electrons used to treat superficial tumors or to hit a metallic target for producing X-rays, which are used to treat deeper tumors.

At the electrons energies sufficiently high so that the upper boundary of the X-ray spectrum is more than 10 MeV, the photoneutrons can be released from any nucleus and the target may also cause the generation of neutrons [1].

At the electrons energies sufficiently high so that the upper boundary of the X-ray spectrum is more than 10 MeV, the photoneutrons can be released from any nucleus and the target may also cause the generation of neutrons [1].

The unwanted process of generating neutrons takes place in two stages: the first stage involves the partial conversion of the electrons energy into electromagnetic energy or the generation of the so-called braking radiation (Bremsstrahlung), and the second stage involves generating the neutrons by photonuclear reactions [1].

The neutrons produced are classified into two groups: evaporation neutrons, which have a Maxwell distribution of their energies and direct neutrons, which are produced by direct interaction between a photon and a neutron from the nucleus of the atom-target. Approximately 15% of all neutrons produced in (γ,n) reactions are direct neutrons and their energy is greater than that of the evaporation neutrons [2].

[1] Babes Bolyai University, Faculty of Physics, Kogălniceanu 1, RO – 400084 Cluj-Napoca, Romania
[2] Oncology Institute "Prof. Dr. I. Chiricuta", Republicii 34-36, RO – 400015 Cluj-Napoca, Romania

The evaporation neutrons form the vast majority of the neutrons and their spectrum is described by the formula [2]:

$$\frac{dN}{dE_n} = \frac{E_n}{T^2}\exp\left(-\frac{E_n}{T}\right) \qquad (1)$$

where E_n is the neutron energy measured in MeV and T is the nuclear temperature corresponding to the nucleus-target, measured in MeV. For the tungsten target, the temperature corresponding to the production of neutrons is 0.5 MeV [2].

Taking account of the X-rays energy and considering the source of neutrons to be isotropic, the formula (1) becomes:

$$\frac{dN}{dE_n} = \frac{0.8929E_n}{(0.5)^2}\exp\left(\frac{-E_n}{0.5}\right) + \frac{0.1071\ln[\frac{E_{max}}{E_n+7.34}]}{\int_0^{E_{max}-7.34} ln[\frac{E_{max}}{E_n+7.34}]dE_n} \qquad (2)$$

where E_{max} is the known X-rays energy and E_n is the neutron's energy.

The fast neutrons which are produced in (γ,n) reactions are thermalized by scattering on the atoms of the material while passing through the concrete wall.

The process of slowing generates epithermal and thermal neutron fluxes. In the concrete wall of the therapy room, neutron capture reactions also take place, producing highly penetrating gamma quanta [3, 4].

In this study, the neutron detector was placed near the therapy room, at a distance of about 25 cm, for both accelerators, in different points of interest indicated in Fig. 1 and 2.

2. Materials and methods

2.1. A brief description of the medical accelerators "Saturne 41" and "Primus"

Our medical linear accelerator "Saturne 41" produces electron beams with energies of 6, 7, 9, 10.5, 12, 13.5 and 16 MeV. The X-rays have energies of 6 MV and 15 MV bias. The absorbed dose rate at the isocentre is approximately 200 cGy/min. The neutron equivalent dose at the distance of 1,41 m from the target, expressed per unit of dose, due to the X-rays at the isocentre, has a value of 0.32 mSv *n*/Gy *X* , given by [5]. The second our medical linear accelerator is "Primus" type.

The absorbed dose rate at the isocentre is approximately 300 cGy/min. The neutron equivalent dose at the distance of 1,41 m from the target, expressed per unit of dose, due to the X-rays at the isocentre, has a value of 0.17 mSv *n*/Gy *X* given by [5]. The X-rays produced have energies of 6 and 15 MV bias equivalent.

2.2. The neutron detector

We used the Neutron Detector FHT 752, which consists of a proportional counter tube, filled with BF_3 (1 bar), a PE-moderator, high voltage supply, a

preamplifier and a pulse shaper. The neutron and gamma radiation are measured successive. The dose equivalent rate (Sv/h) measuring range, for neutrons, is 1 Sv/h-0.4 Sv/h and the energy range : 0.025 eV- 20 MeV, according to ICRP 60. For the gamma detector, the measuring range for the dose equivalent rate is 10 nSv/h – 1Sv/h and the energy range goes from 36 KeV to 1.3 MeV.

3. Results and discussion

For the medical accelerator "Saturne 41", the measurements were made in 8 different points noted P_i, shown in Fig.1. Each measurement lasted an hour. The results are presented in Table 1.

Table 1.

The dose values for neutron and gamma radiation obtained by "Saturne 41".

	P_1	P_2	P_3	P_4	P_5	P_6	P_7	P_8
The γ dose (nSv)	145	133	133	485	983	207	206	202
The neutron dose (nSv)	105	8.96	90.7	8.4	3970	454	418	213
The γ and n dose (nSv)	250	142	224	494	4950	661	625	415
The average dose rate for neutrons (nSv/h)	105	8.83	89.5	6.3	4000	448	415	215
The maximum dose rate for neutrons (nSv/h)	380	31.3	370	25.2	32700	3690	3080	2370

For the medical accelerator "Primus", the measurements were made in 7 different points noted P_i', shown in Fig.2. Each measurement lasted an hour and the results are presented in Table 2.

Table 2.

The dose values for neutrons and gamma radiation obtained by "Primus".

	P_3'	P_4'		P_5'	P_6'	P_7'	P_8'	P_{10}'
the γ dose (nSv)	121	206	109	121	109	109	133	182
the n dose (nSv)	4.48	6.72	5.04	26.3	6.16	3.36	3.92	52.1
the γ and n dose (nSv)	125	213	114	147.3	115	112	137	222

	P_3'	P_4'		P_5'	P_6'	P_7'	P_8'	P_{10}'
the average dose rate for neutrons (nSv/h)	4.32	6.60	4.96	26	5.98	2.66	3.37	45.8
the maximum dose rate for neutrons (nSv/h)	20.7	26.7	25.5	324	25.5	21.6	17	250

In Table 2, for P_4' point, placed in the waiting room, the results are written in two columns. The first column contains the measurements made when, during an hour, seven patients were irradiated: six of them, at the energy of 15 MeV and one, at the energy of 6 MeV. The second column contains the measurements made when, during an hour, six patients were irradiated: five of them, at the energy of 6 MeV and one, at the energy of 15 MeV. The neutron dose increases in the first case, when the most of the patients were irradiated at the energy of 15 MeV. The total neutron and gamma radiation dose is 1.86 times higher in the first case than the total dose from the second. The gamma radiation dose is 1.88 times in the first case than that from to the second, which reflects the proportionality between the productivity of the barking radiation and the incident electrons kinetic energy.

The P_5 point is placed at 25 cm in front of the sliding door of the "Saturne 41" accelerator. Comparing the values obtained here with those obtained in P_5', which is placed at 25 cm in front of the sliding door of the "Primus" accelerator, we found that the total neutron and gamma radiation dose was 33.6 times, respectively, the average dose rate was 153.84 times higher. The sliding door of the "Saturne 41" accelerator doesn't contain a shield for neutrons, which explains the high value obtained here for the average dose rate of neutrons (4000 nSv/h).

The sliding door of the "Primus" accelerator is made of a lead layer with a thickness of 5 cm and a polyethylene layer with a thickness of 10 cm. The average neutron dose rate obtained in point P_5' has a value of 26 nSv/h, due to the polyethylene neutron shield.

The differences arising between the values in the points (P6' and P7', P2 and P4) which are symmetrically placed to the isocenters of the two accelerators, it is due to the number of patients treated during the measurements, the beam direction and the irradiation time which varies from one measurement to another.

The P_3 point is placed in the "Saturne 41" accelerator control room. The total neutron and gamma radiation dose found here is higher than the one measured in point P_3', situated in the "Primus" accelerator control room. This can be explained by the specific neutron production of the accelerators and by the different absorption between the measurement points and the isocenteres of each accelerator.

4. Conclusions

The values found in the P_4 point, placed in the waiting room, require the construction of a decorative wall in the near future. It must be taken into account the fact that the patients and sometimes the persons who accompany them spend some time in the waiting room, so the risk of involuntary irradiation should be avoided.

The doses found in these important points (in the waiting room, in front of the sliding door, in the control room) require the replacement of the "Saturne 41" sliding door with one that screens the neutrons.

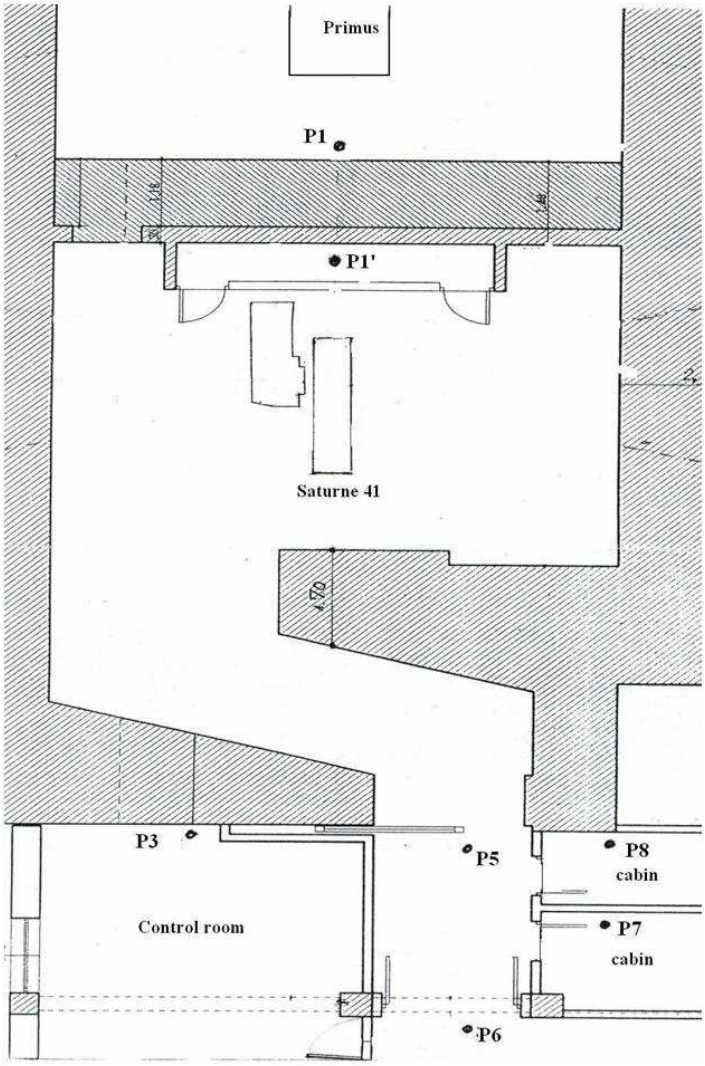

Figure 1. "Saturne 41" accelerator scheme. The measurement points are indicated on the figure.

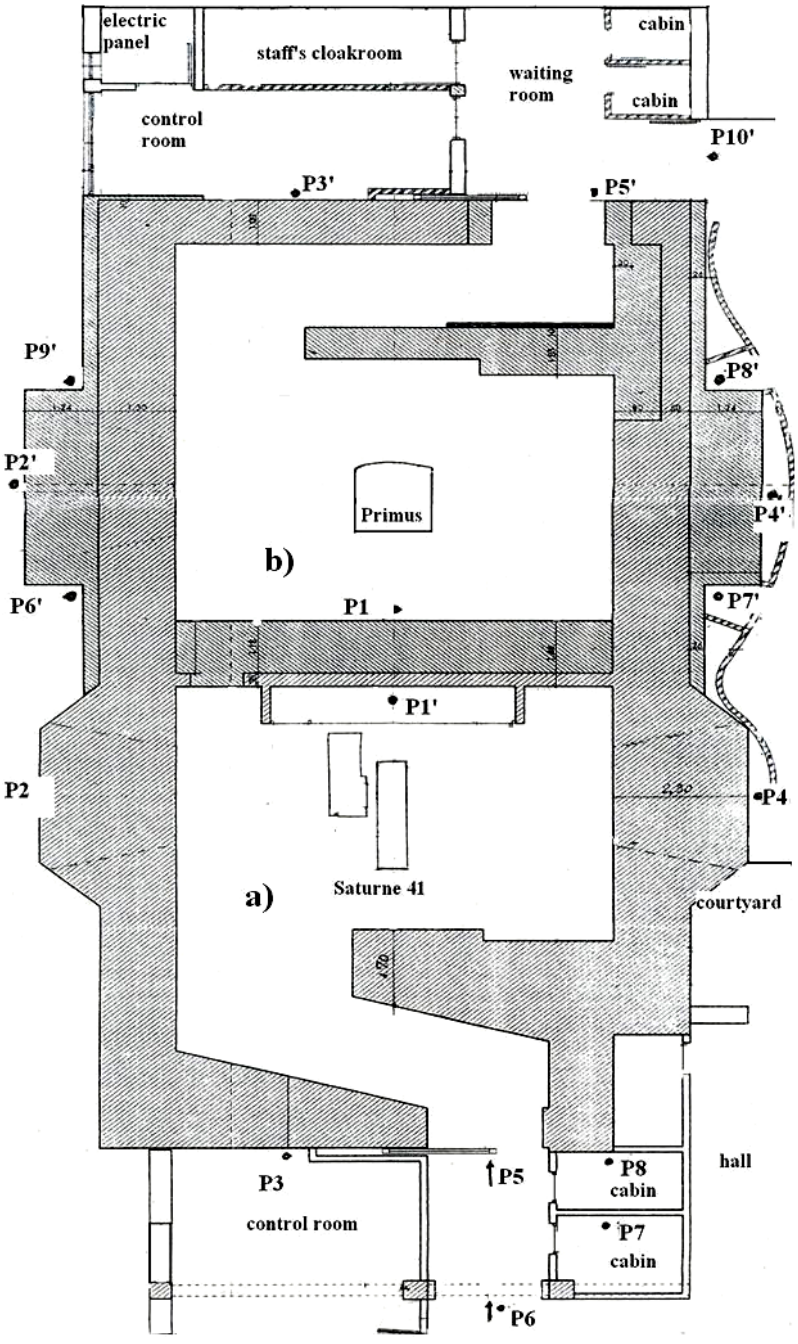

Figure 2. "Saturne 41" and "Primus" accelerators scheme:
(a) Saturne 41 and (b) Primus.

REFERENCES

1. I.E. Teodorescu, *Neutron generators. Principles and uses*, Acad. RSR Publisher, Bucharest (1969).
2. A. Facure, R. C. Falcão, A. X. Silva, V. R. Crispim, J. C. Vitorelli, *A study of neutron spectra from medical linear accelerators,* Applied radiation and Isotopes, **62**, 69-72 (2005).
3. A. Facure, R. C. Falcão, A. X. Silva, V. R. Crispim, *Neutron dose rate evaluation for medical linear accelerators,* Radiation Protection Dosimetry **111**(1), 101-103 (2004).
4. J. C. Rivera, R. C. Falcão, C. E. deAlmeida, *The measurement of photoneutrons in the vicinity of clinical linear accelerators,* Radiation Protection Dosimetry **130**(4), 403-409(2008).
5. NCRP Report Nr. 51 (NCRP 1977)

STUDIA UNIVERSITATIS BABES-BOLYAI, PHYSICA, LIV, 1, 2009

CHARGE TRANSFER IN Fe /Ga As(001)INTERFACE

V. CRISAN*

ABSTRACT. The KKR band structure and the pseudopotential molecular dynamic calculations have revealed important interlayer (metal-semiconductor) as well as intralayer (between Fe atoms) charge transfer. Due to the different atomic environment of the Fe atoms at the interface they became nonequivalent. It is the intralayer charge transfer responsible of the antiferromagnetic ordering of Fe magnetic moments at the interface.

Keywords: Single crystals films, charge transfer, intralayer charge

Single crystals films grown epitaxially on semiconductor substrates offer on opportunity to realize on artificial low dimensional system with controllable magnetic properties, and for a range of device applications [1] while also permitting fundamental studies in magnetism, [2-7].

Fe on GaAs is of interest as a model system for the epitaxial growth of ferromagnetic metals(FM) on semiconductors. It has been shown [3], [7-11] that bcc Fe grows epitaxially on (001) surface done in part to the fact that the lattice constant of bcc Fe (a=2.866A) is almost exactly half that of Ga As (a=5.654A). Fe/Ga As is also of current interest due to its potential as FM spin injection pads [12, 13]. However a strong reduction of the magnetization has been found [8]. The reduction of the Fe moment was attributed to the magnetically “dead” layers near the interface, which would be detrimental to the spin dependent transmission and tunneling between the FM metal and the semiconductor substrate. Thus the interface structure and magnetism is a key issue for current research.

The present study aims to characterise the magnetic properties of FM - semiconductor atoms, by using KKR band structure method in a scalar relativistic way in LDA by using the exchange-correlation parametrisation of Moruzzi, Janak and Williams. The molecular dynamic calculations were done by pseudopotential method as was implemented in the Viena code, VASP. The calculation were done on a supercell formed by 5 layers of GaAs and 3 layers of Fe as is seen in Figure 1.

The lattice parameters were decreased from the experimental on a to smaller values in order to see the As position effect on the Fe atoms. It is know that As and Fe form stable chemical compounds, with small Fe magnetic moments.

* Faculty of Physics,Babes-Bolyai University,Cluj-Napoca

No serch compounds were found at the Fe/GaAs interface. As the lattice parameter decreases, there is a charge transfer from metal to semiconductor. For some lattice parameter the change transfer is also from one Fe atom to the other Fe atom located in the same layer.

During this interlayer transfer the Fe spin is flipping which lead to an antiferromagnetic moments in the layer situated closest to the semiconductor.

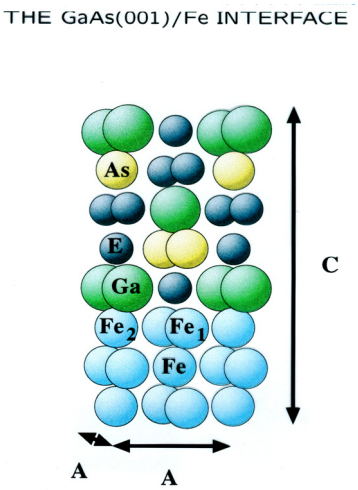

Figure 1. The interface unit cell used in molecular dynamics calculations.$Fe_1$and Fe_2 denote the nonequivalent Fe atoms in the first layer of interface while E empty spheresused to improuve the convergence in linear band structure methods.The semiconductor is Ga terminated. The top 5 lyers form semiconductor partand the last 3 layers the metal one.

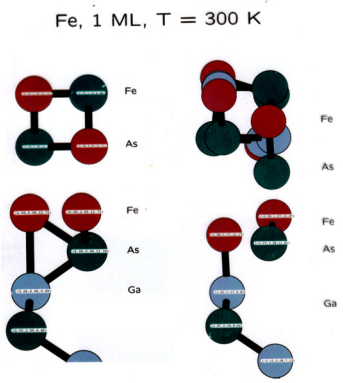

Figure 2. A snap-shot of the atomic positions of atoms from unit cell with one monolayer of Fe at T = 300 K.The left column is the side and top view of the T = 0 K while the right one is at T = 300. The solid lines denote the presumed chemical bonding.It is seen the As atom which changes the position,while the other atoms continue to occupy the same positions.

The modification of the lattice parameter have compensated the fact that the calculations were done for T=0 K (as usual in band structure calculations). At T≠0 K the positions of the interatomic distances are changed. During this dynamics of the atoms the system can rech the situations described by a lattice parameter modifications.

In figure 2 we show a snap-shot of the atomic position in the unit cell as obtained by molecular dynamic calculation, by using the same supercell but with different number of layers in the Fe slab.The pair correltion function shows as is seen in figure 2. that the As atom spend more time in the neighbor of Fe atom which depend on the temperature.The physical picture is that the interface is formed by a fluctuating As-Fe bonding atoms. The charge transfer is produced as usual from metal to semiconductor as well as in the Fe layer closest to the semiconductor.

Conclusions.The interlayer charge transfer reduce the chare in Fe slab and the exchange interaction is changing the sign and the antiferromagnetic ordering appears. The intralayer charge transfer is in fact an charge redistribution in the Fe slab producing the modification of the magnitude of the magnetic moments.

REFERENCES

1. G.A. Prinz, J.J. Krebs, Appl. Phys. Lett. 39, 397 (1981), J.J. Krebs, B.T. Jonker, G.A. Prinz, J. Appl. Phys. 61, 2596 (1987)
2. G.A. Prinz, Science, 250, 1092 (1990)
3. V. Crisan, P. Entel, G. Rollmann, J. Mag. Magn. Mat., 240, 417 (2002)
4. G.A. Prinz, B.T. Jonker, J.J. Krebs, Appl. Phys. Lett.48, 1756 (1986)
5. A. Chambers, F. Xn, H.W. Chen, I.M. Vitovirov, S.B. Anderon, J.H. Weaver, Phys. Rev B34, 6605 (1986)
6. K.T. Riggs, E.D. Dahlberg, G.A. Prinz, Phys. Rev. B41, 7088, (1990)
7. J.M. Florczak, E.D. Dahlberg, Phys. Rev. B44, 9338 (1991)
8. G.A. Prinz, G.T. Rado, J.J. Krebs, J Appl. Phys. 53, 2087 (1982)
9. C. Dolrao, J. Hicken, E. Gu, J. Gesters, D.E.P.Gray, E. Eley, J.A. CAhmand, C. Bland, Phys. Rev. B51, 15964 (1995)
10. A. Filipe, A. Schnhl, P. Galatier, Appl. Phys. Lett. 70, 129 (1997)
11. E.M. Kneedler, B.T. Jonker, P.M. Tibdo, R.J. Wagner, B.V. Shanabrook, L.J. Witman, Phys. Rev. B56, 8163 (1997)
12. Datta, B. Das, Appl. Phys. Lett. 56,665 (1990)
13. G.A. Prinz, Phys. Today, (4), 58 (1995).

STUDIA UNIVERSITATIS BABES-BOLYAI, PHYSICA, LIV, 1, 2009

MOLECULAR MASS EFFECT ON RHEOLOGICAL BEHAVIOR OF SOME AQUEOUS POLY (ETHILENE OXIDE) GELS

C. V. POP[1], L. UDRESCU[1], E. DINTE[2], M. TODICA[1]

ABSTRACT. The concentration and temperature dependence of the viscosity were observed for some aqueous poly (ethylene oxide) gels with different molecular mass. The transition from Newtonian to non-Newtonian behavior was observed at specific temperatures and polymeric concentration characteristic for each molecular mass of the polymer. The experimental data were analyzed with the power model and revealed the shear thinning or shear thickening behavior of the viscosity in function of the polymeric concentration.

Keywords: poly (ethylene oxide), viscosity, power law

Introduction

The poly (ethylene oxide) is one of the polymers widely used as support for the pharmaceutical products with dermatological applications. This polymer is known for its good mechanical properties, flexibility, biological neutrality and for the capacity to produce gels in aqueous solution. The gels can include pharmaceutical substances, that can be delivered under controlled condition in the desired area of the skin [1-5]. For clinical applications some mechanical properties, the adhesion the flexibility and the viscoelasticit are of great importance. Quantitative description of these properties is based on the measure of some rheological parameters, between which the viscosity plays an important role [6, 7]. The viscosity is strongly influenced by the polymeric concentration, the temperature and the molecular mass of the polymer. These dependences were observed in our study for aqueous gels based on polymers with two different molecular masses.

Experimental

The polymers used for our works were the poly (ethylene oxide) PEO 750 with molecular mass of 75 000 g/mol and PEO 1105 with molecular mass of 105 000 g/mol. At low polymeric concentration, a semisolid gel is obtained by mixing the polymer with distilled water during 3-4 hours. The polymeric concentrations of the samples were 3% and 5% for the first polymer, and 2% and 3% for the second

[1] "Babes-Bolyai" University, Faculty of Physics, Cluj-Napoca, Romania, 400084 Cluj-Napoca, e mail: tami@phys.ubbcluj.ro
[2] University of Medicine and Pharmacy, Faculty of Pharmacy, Cluj-Napoca, Romania

one. Homogeneous gels can be obtained only at small polymeric concentration. Above the concentration 11% no homogeneous gel is obtained and a separation of phases can be observed. We measured the viscosity of these samples at different rotation speed, between 0 and 200 rot/min, with a Brookfield DV II Pro viscometer. The determinations were made in the temperature range 26 - 55 ºC.

Results and discussion

The particularly response of the polymeric samples under external mechanical solicitations is determined by the existence of temporary or permanent junction between the polymeric chains. These connections are extended only to limited domains of the sample in molten state or in the solutions, allowing a limited mobility of the macromolecules. When these connections are extended to large areas of the sample, a spatial disordered and elastic structure appears, and a continuous passing between every two points of the sample is possible. This situation corresponds to the gel state. At weak amplitude and short time mechanical solicitations the system behaves like an elastic one, but at strong solicitations the network is destroyed and the system behaves like a viscous fluid [8, 9]. The polymeric concentration and the thermal agitation are two important factors with great influence on the viscosity. The thermal agitation reduces the stability of the temporary connections allowing a high local mobility of the chains. At macroscopic scale this effect is responsible for the variation of the viscosity with the temperature. High polymeric concentration facilitates the formation of the connections between the chains and the viscosity increases [10, 11]. The length of the polymeric chains facilitates the apparition of the gel state and play an important role on the viscosity. In addition we can observe a dependence of the viscosity in function of the time of application of mechanical solicitations. Under continuous stress the system can flow following Newtonian or non-Newtonian character in function of the contribution of the factors enumerated above.

The influence of the molecular mass on the dependence of the viscosity in function of the polymeric concentration, temperature, and shear rate was observed in our study. The main interest was the observation of the transition from Newtonian to non-Newtonian flow. We investigated first the samples with small molecular mass (POE 750). The smallest value of the viscosity was measured at 3% concentration. For this polymeric concentration of the gel the viscosity increases with the increase of the shear rate and decreases with the increase of the temperature for all the temperatures, (Fig. 1). At this concentration the gel state can be regarded as low structured network characterized by a specific relaxation time under external mechanical solicitations. At low shear rate, the time of solicitation is enough long to allow the disengagement from the entanglement of the polymeric chains located in different neighboring layers. The mechanical solicitation propagates at short distance, perturbing only few neighboring polymeric layers. The result is a low value of the viscosity. When the speed increases, the time of solicitation is short, and the chains located in neighboring layers have not enough time to disengage from the entanglements. The mechanical solicitation propagates at long distance, between many layers of flow, and the viscosity increases.

The variation of the viscosity with the shear rate indicates non-Newtonian flow. A different situation is observed for the concentration 5%. At 55ºC the viscosity is almost constant, indicating the Newtonian flow. For other temperatures, 37ºC and 26ºC the viscosity decreases with the increase of the shear rate, indicating the transition from Newtonian to non-Newtonian flow, (Fig. 2). At this concentration the gel is extended to large domains of the sample and it behaves like an viscoelastic network. At low shear

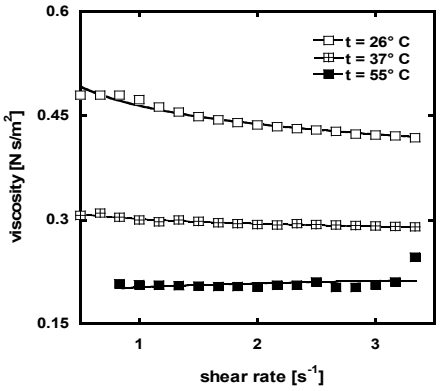

Fig.1. The viscosity vs. shear rate at different temperatures, for the sample PEO 750 with polymeric concentration 5 %.

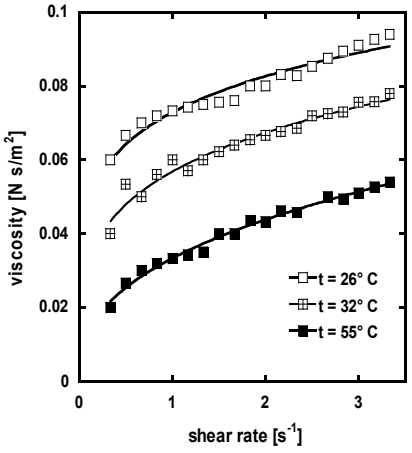

Fig. 2. The viscosity vs. shear rate, at different temperatures, for the sample PEO 750 with polymeric concentration 3 %.

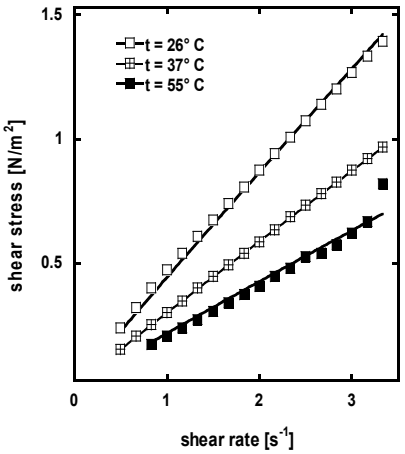

Fig. 3. The shear stress vs. shear rate, at different temperatures, for the sample PEO 750 with polymeric concentration 5 %.

rate, the time of solicitation is enough long to allow smooth disengagement from the entanglement of the polymeric chains located in different neighboring layers, allowing an elastic deformation of the local polymeric network, without fracture. The mechanical solicitations propagate at long distance, perturbing many neighboring polymeric layers. The result is a high value of the viscosity [12]. When the speed increases, the time of solicitation is shorten that the relaxation time of the chains from the entanglements, the chains located in neighboring layers have not enough time to disengage smoothly from the entanglements, and a great majority of them are broken. The gel domains are brutally separated. The mechanical solicitation propagates at short distance between the layers of flow and the viscosity decreases. The decrease of the viscosity with the temperature is determined by the amplification of the local mobility of the chains that facilitates the disengagement of the chains from the entanglements that leads to a reduction of the viscosity. In the classic theory of viscosity a constant value of the viscosity is associated with the Newtonian model, that predicts a linear dependence of the shear stress in function of shear rate [7, 12], (equation 1).

$$\sigma = \eta \cdot \dot{\gamma} \tag{1}$$

σ represents the shear stress, $(\dot{\gamma}) = \frac{\partial \gamma}{\partial t}$ represents the shear rate, and η is the viscosity. This situation is characteristic for the concentration 5% at 55ºC. The average value of the viscosity is η_{av}=0.20 N s/m^2

The Newtonian law cannot be applied when the viscosity is not constant. The simplest model, which is often used for the firs approximation, is the power law [12, 13], (equation 2).

$$\sigma = a \cdot (\dot{\gamma})^n \tag{2}$$

The meaning of the parameters is the same as in equation 1. *a* represents a proportionality parameter. The power exponent *n* contains the correction added to the Newtonian model, and it is correlated with the character of the fluid flow, shear-thinning (n<1), or shear-thickening (n>1) [13-15]. If we denote $n = 1 + x$ we can separate the Newtonian contribution in equation (2).

$$\sigma = a \cdot (\dot{\gamma})^{1+x} = a \cdot (\dot{\gamma})^x \cdot (\dot{\gamma}) \tag{3}$$

In equation (3) the first two factors play the roll of viscosity. On the basis of this observation the dependence of the viscosity in function of the shear rate can be expressed as follows:

$$\eta = a \cdot (\dot{\gamma})^x \tag{4}$$

The power exponent *x* characterizes the dependence of the viscosity in function of shear rate. For zero value of *x*, the viscosity became constant with *a* representing the average viscosity, as in the Newton's model, (equation. 1).

Table 1.

sample	*t* (^0C)	*a* (Ns/m^2)	*x*	x_{av}	*n*	*a** (Ns/m^2)
Peo 750 5%	26	0.46	-0.08	-0.023	0.97	0.44
	37	0.30	-0.03			0.30
	55	0.20	0.04			0.21
Peo 750 3%	26	0.07	0.18	0.27	1.27	0.06
	32	0.05	0.24			0.05
	55	0.03	0.39			0.03
Peo 1105 3%	32	0.97	-0.11		0.89	1.00
	37		0		1	0.77
	42	0.69	0.01		1.01	0.68
Peo 1105 2%	26	0.15	0.23	0.14	1.14	0.16
	37	0.10	0.18			0.10
	42	0.69	0.01			0.08

The parameters *n*, *x* and *a*, are calculated from the experimental data, on the basis of equations (2) and (4). Using equation (4) we can estimate the values of parameters *a* and *x*. The values of these parameters are listed in Table 1. Taking into account the small variation of *x* determined by the temperature at constant concentration, in the first order of approximation, we can neglect the variation with the temperature of the parameter *x*, considering only the dependence of concentration. For each concentration we considered the average value of *x*, i.e. x_{av}= 0.27 for concentration 3%, x_{av}=-0.023 for concentration 5% when we analyzed the effect of temperature. For each temperature we calculate the power exponent *n* from the relation $n = 1 + \mathrm{x}_{\mathrm{av}}$. These values were used to approximate the experimental data $\sigma(\dot{\gamma})$ with the equation:

$$\sigma = a^* \cdot (\dot{\gamma})^n \tag{5}$$

The fit of experimental data with this equation for concentration 5% is presented in figure 3. The values of parameter *a* resulting from this fit, denoted by a*, are compared with the values of *a* resulting from the fit with equation (4). The good agreement between these values confirms the validity of the power model and of the algorithm of analyze proposed for ours experimental data, (equation 2, 3 and 4).

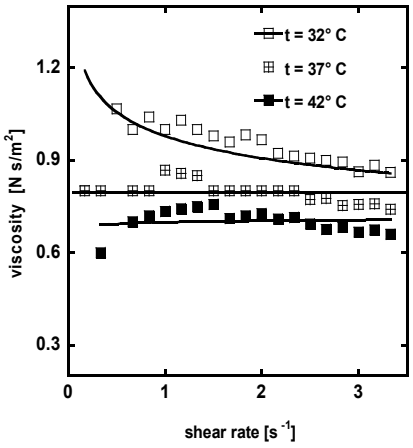

Fig. 4. The viscosity vs. shear rate, at different temperatures, for the sample PEO 1105 with polymeric concentration 3%.

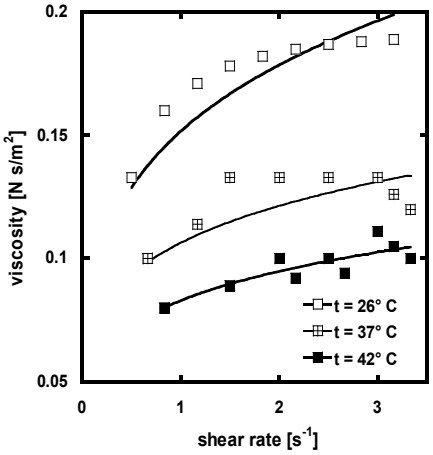

Fig. 5. The viscosity vs. shear rate, at PEO 1105 with polymeric concentration 2 %.

Similar results were obtained for the samples PEO 1105, but the transient effect from Newtonian to non-Newtonian flow was observed at 3% concentration instead 5% for the sample PEO 750, (Fig. 4 and 5). The parameters of the fit are listed in Table 1. The molecular mass of the sample PEO 1105 is greater than the mass of the sample PEO 750. For this reason a given value of the viscosity is observed for this sample at lower concentration than in the case of the sample PEO 750. The increase of the molecular mass in the case of sample PEO 1105 is equivalent to the increase of the concentration of the sample PEO 750.

The knowledge of power exponent n is of high importance to characterize the rheological behavior of the samples. For the sample PEO 750 this exponent decreases with the increase of the polymeric concentration, from n=1.27 at 3% to n=1 at 5% and 55ºC. The samples are characterized by non-Newtonian behavior, shear-thickening (n>1) [14, 15] in this domain of temperatures and concentrations. The flow became Newtonian at 5% and 55ºC and then, with the growing of the viscosity, it became again non-Newtonian, shear-thinning (n<1), n=0.97 at 5% and 37-26ºC. For the sample PEO 1105 we observed a translation of this behavior towards low polymeric concentrations. The exponent n decreases from n = 1.14 at 2% concentration and 26ºC to n=1.01 at 3% concentration and 42ºC. The samples are characterized by shear-thickening (n>1) in this domain of temperatures and concentrations [14, 15]. The transition appears at 3% concentration and 37ºC. n decreases until n=0.89 at 3% and 32ºC. Here the sample is characterized by shear-thinning behavior. Both the temperature and polymeric concentration affect the viscosity of the gel, but the influence of the concentration is dominant.

Conclusions

The decrease of the viscosity in function of temperature was observed for all ours samples, characterized by different molecular mass. The variation of the viscosity vs. of shear rate indicates different flows, shear-thickening, Newtonian and shear-thinning, depending on the temperature and polymeric concentration.

The transition from shear-thickening to shear-thinning is mainly determined by the polymeric concentration. The Newtonian flow is observed for both the samples but this behavior appears at low polymeric concentration for the high molecular mass compared with the sample with low molecular mass. In the non-Newtonian regime, the rheological behavior of the sample is described by the power model.

A simple algorithm for the analysis of experimental data, based on this model, is proposed. The values of parameters obtained from this analysis allow a good approximation of the experimental data with the equations (2) and (4).

REFERENCES

1. N. Lambov, N. Dimitrov, Tsankov S, Pharmazie, 52 790, (1977)
2. H. Savaş, O. Güven, Int. J. Pharm, 224 151, (2001)
3. L. Maggi, L. Segale, et al, Biomaterials, 23 1113, (2002)
4. Kim Ch Ju, J. Pharm. Sci. 84 303, (1995)
5. A. S. Hoffman, Adv. Drug Del. Rev. 43 3, (2002)
6. P. Borgquist, A. Korner et al, J. Controlled Release, 113 3 216, (2006)
7. M. Solomon, Viscozimetrie şi elemente de teorie a vâscozităţii, Ed. Tehnică, Bucureşti, 1958.
8. P. J. Flory, Statistical Mechanics of Chain Molecules, Interscience Publishers, New York, 1969.
9. M. Rubinstein and R. Colby, Polymer Physics, Oxford University Press, Oxford, 2002.
10. P. G. De Gennes, Scaling Concepts in Polymer Physics, Cornell University Press, Ithaca, 1979.
11. J. P. Cohen-Addad, NMR and Fractal Properties of Polymeric Liquids and Gels, Pergaman Press, London, 1992.
12. E. C. Bingham, Fluidity and Plasticity, McGraw-Hill, New-York, 1922.
13. Q. D. Nguyen, D. V. Boger, Annual Review of Fluid Mech., 24 47, (1992)
14. Park Sang-Wook, Choi Byoung-Silk and Lee Jae-Wook, Korea-Australia Rheology Journal, 17 4 199, (2005)
15. Sung Jun Hee, Sung Taek Lim, Chul Am Kim, Heejeong Chung and Hyoung Jin Choi, Korea-Australia Rheology Journal, 16 2 59, (2004)

STUDIA UNIVERSITATIS BABEŞ-BOLYAI, PHYSICA, LIV, 1, 2009

SOIL RADON MEASUREMENTS IN CLUJ-NAPOCA (ROMANIA)

DAN CONSTANTIN NIȚĂ[*], CONSTANTIN COSMA, PAPP BOTOND, MIRCEA MOLDOVAN

ABSTRACT. A wide interest subject in radioprotection is the issue of radon because it represents over 50% of natural radiation dose received by the population. Radon gas is an odorless, colorless, whose physical and chemical properties allow it to migrate to considerable distances. Besides other factors influencing soil radon concentration, the concentration and distribution of radon in soil parents have been found to be most dominant. Measurements of concentrations of radon (^{222}Rn) in Cluj-Napoca have highlighted regional variations, around the Someş River. The concentrations of radon found with the LUK3C detector varies between 1186 kBq/m^3 and 55.84 kBq/m^3. These variations have increasing or decreasing trends, once approaching the Someş, emphasizing indirect influence of the Someş River.

Keywords: ^{222}Rn, Radon, Soil - gas, Lucas cell.

Introduction

Radon has several radioactive isotopes, the most important being: the radon (^{222}Rn), the thoron (^{220}Rn) and the actinon (^{219}Rn). Radon (^{222}Rn) is part of the ^{238}U radioactive decay series, is the daughter of ^{226}Ra decay and has a half-life of 3.82 days. Thoron (^{220}Rn) is part of the ^{232}Th radioactive decay series, is a daughter of ^{224}Ra and has a half-life of 55.3 seconds. Actinon (^{219}Rn) is part of the ^{235}U radioactive decay series, is a daughter of ^{223}Ra and has a half-life of 3.96 seconds. Actinon due to the very short half-life, and low natural abundance of his parents, may be neglected in terms of radiological impact [1, 2].

The radiation produced by the decay of radon atoms and its daughters, that are also radioactive elements, creates a significant natural hazard and it poses a serious health risk [3, 4]. The amount of radon in the atmosphere depends primarily of the concentration of uranium and thorium soil and rocks [5, 6]. Meteorological parameters can also be considered a secondary factor that influence the concentration of radon in the atmosphere [7].

The measurements objectives was to discover the areas with high concentrations of radon within the investigated area of Cluj-Napoca and the influence of Someş River on these concentrations.

[*] Babeş-Bolyai University, Faculty of Environmental Science, 400294, Fantanele Street no. 30, Cluj-Napoca, Romania. *Corresponding author: E-mail address: negru_frozen@yahoo.com.*

Experimental method

The measurements were made at a depth of 60 cm, in 36 different locations in Cluj-Napoca (on both sides of the Someş River).

The concentration of radon was determined by the radon detector LUK3C, with Lucas scintillation cells [8].

For collecting the gas samples we extracted a volume of 150 ml, using a Janet syringe, from the extraction tube, which was introduced at a depth of 60 cm (Figure 1).

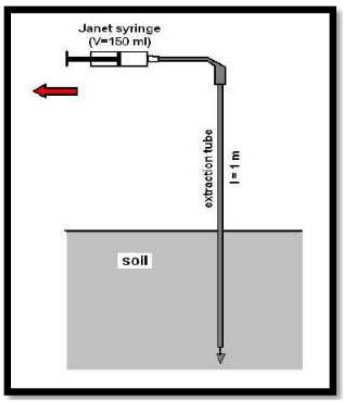

Figure 1 – Scheme of the method used for extracting the gas from the soil

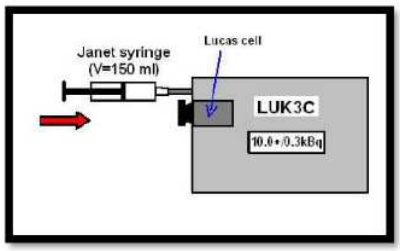

Figure 2 - Scheme of the extracted gas transfer in the detector

The extracted sample was transferred in the radon detector (Figure 2), with a preliminary mechanism of vacuum. The detector used to determinate the concentration of radon is based on scintillation detection.

The measurements were made over 3-4 days, in which variations of temperature, humidity and wind were minimal.

Results and discussion

The map of all the locations where samples were collected is shown in Figure 3, the color gradient vary depending on the determined concentration.

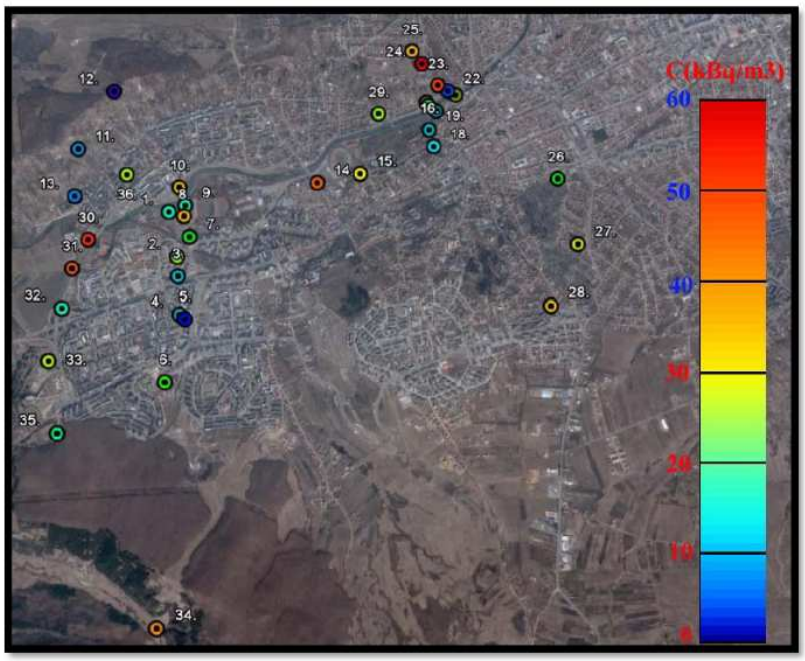

Figure 3 – The measurements location map of Cluj – Napoaca (modified Google map)

Based on the identification number displayed, we have divided the map into six zones, for a more detailed and clear view of the results.

Zone 1		
Identification no.	C ± ΔC (kBq/ m^3)	River distancing
10	32.89 ± 1.561	1
13	7.427 ± 0.55	2
36	17.83 ± 0.874	3
11	9.538 ± 0.62	4
12	1.186 ± 0.233	5

Table 1 – Measurements for zone 1 (where C-^{222}Rn concentration, ΔC- measurement error)

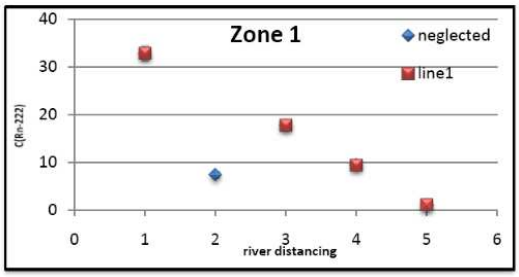

Figure 4 –The results for zone 2

Zone 2		
Identification no.	C ± ΔC (kBq/ m^3)	River distancing
30	54.15 ± 2.652	1
31	47.31 ± 2.132	2
32	16.29 ± 0.827	3
33	25.86 ± 1.252	4
35	17.83 ± 0.874	5
34	39.81 ± 1.957	6

Table 2 - Measurements for zone 2

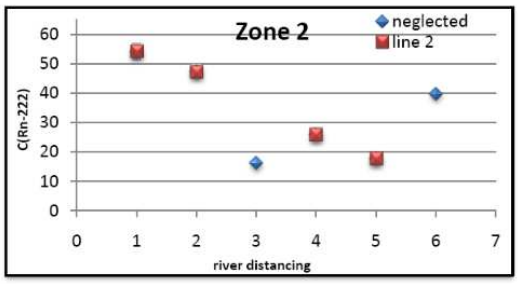

Figure 5- The results for zone 2

Zone 3		
Identification no.	C ± ΔC (kBq/ m^3)	River distancing
1	17.16 ± 0.836	1
9	16.45 ± 0.822	2
8	36.35 ± 1.803	3
7	20.41 ± 0.961	4
2	22.46 ± 1.086	5
3	12.74 ± 0.717	6
4	12.35 ± 0.721	7
5	2.102 ± 0.303	8
6	21.08 ± 1.045	9

Table 3 - Measurements for zone 3

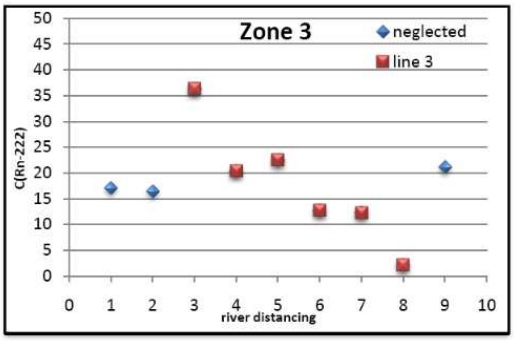

Figure 6 - The results for zone 3

Zone 4		
Identification no.	C ± ΔC (kBq/ m^3)	River distancing
14	43.05 ± 2.03	1
15	29.03 ± 1.353	2
28	28.38 ± 1.335	3

Table 4 - Measurements for zone 4

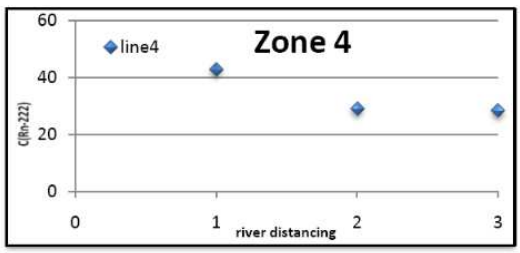

Figure 7 - The results for zone 4

Zone 5		
Identification no.	C ± ΔC (kBq/ m^3)	River distancing
17	14.44 ± 0.778	1
16	12.31 ± 0.727	2
18	12.98 ± 0.728	3
26	20.43 ± 0.959	4
27	28.38 ± 1.335	5
28	31.39 ± 1.541	6

Table 5 - Measurements for zone 5

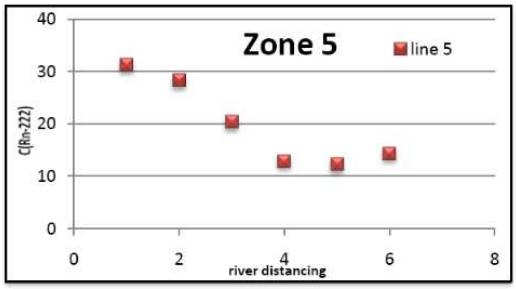

Figure 8 - The results for zone 5

Zone 6		
Identification no.	C ± ΔC (kBq/ m^3)	River distancing
19	19.48 ± 0.936	1
21	28.06 ± 1.321	2
22	4.226 ± 0.429	3
20	33.59 ± 1.584	4
29	23.77 ± 1.107	5
23	49.66 ± 2.178	6
24	55.84 ± 2.633	7
25	34.33 ± 1.613	8

Table 6 - Measurements for zone 6

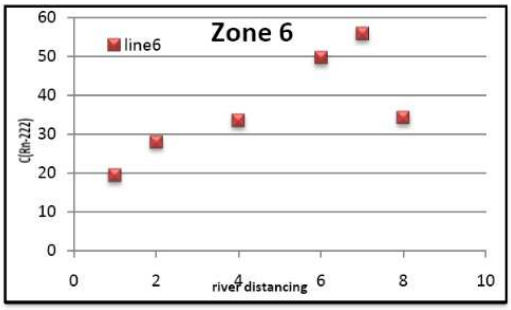

Figure 9 - The results for zone 5

The results of the following locations measurements are neglected:

- 13 because the soil is clayey, giving a low permeability;
- 32 because it was the beginning of a bridge, influencing the result;
- 34 because it was too far from Someş, and cannot see the influence of the river;
- 1 and 9 because in these areas arrangements, paving and construction work have been conducted, that involved disturbance of soil;
- 6 because soil permeability was low;
- 22 because it was too close to a block of flats, a factor that influence the concentration of radon;
- 29 because it was too far from Cetățuia hill, cannot be part of a distancing line from Someş.

In the 1-4 zones, once approaching the Someş, the concentrations of radon are rising. This is due to the indirect influence of the river. The large concentrations around Someş are due to the silts and sediments, rich in radium and uranium carried by it. The Someş River, as a spring water that streams and crosses rich areas in minerals with high levels of radon parents, is feeding the area close to it with silts and sediments which have high levels of radon parents concentrations.

For the zones 5 and 6 the radon concentrations are increase once distancing the Someş River. In the water area clayey soil predominates, and then, with increasing altitude, red clays begins to predominate, and at higher altitudes, corresponding with the most distanced locations from Someş, the sandstones predominates.

The measurement from the location 6 was carried out on the opposite side of the Cetățuia hill where the other measurements were performed. The predominant sandstones in the composition of the soil zone, are responsible for the concentration of radon found in this location.

Conclusions

The measurements of radon concentrations in the town of Cluj-Napoca highlights local variations of these concentrations with the distance from Someş.

In the first areas investigated the radon concentrations in soil decrease once increasing the distance form Someş. The large concentrations around Someş are due to the silts and sediments rich in ascending radon. These were brought from areas crossed by the river, areas that are rich in minerals that have high levels of radon parents.

The last areas studied the radon concentration are rising with the increaseing the distance from the Someş River. This increase is due to soil composition. In the water area clayey soil predominates, and then, with increasing the altitude, red clays begin to predominate, and at higher altitudes sandstones predominates.

We can conclude that the main factor determining the radon concentration in soil is soil composition, which involves the distribution and concentration of soil radon parents.

BIBLIOGRAFY

1. Constantin Cosma, Jurcuț, 1996, *Radonul şi mediul înconjurător*, Ed. Dacia, Cluj-Napoca.
2. Grigore Damian, 2005, *Surse de radiații nucleare*, Ed. Casa cărții de știință, Cluj-Napoca, 1 – 87, 289 – 325.
3. International Atomic Energy Agency, 2003, *Radiation Protection against Radon in Workplaces other than Mines*, Safety Reports Series no.33, Viena, Austria.
4. Nero, 1989, *Earth, air, radon and home*, Physics Today, 42, 32-39.
5. Nazaroff W.W. and Nero A.V., *Soil as a source of indoor radon: generation, migration and entry: Radon and its decay products in indoor air*, A Wiley-Interscience publication, 57-112, (1988).

6. Sogaard-Hansen, J. Damkjær, 1987, *Determining 222 - Rn diffusion lengths in soils and sediments*, Health Physics, Vol. 53, no. 5, 455 – 459.
7. Ryoko Fujiyoshi, Keita Sakamoto, Tsukushi Imanishi, Takashi Sumiyoshi, Sadashi Sawamura, Janja Vaupotic, Ivan Kobal, 2006, *Meteorological parameters contributing to variability in 222Rn activity concentrations in soil gas at a site in Sapporo, Japan*, Science of the Total environment 370 (2006), 224–234.
8. Radon Detector, LUK3C, 1997, Instruction manual.